Master's thesis

NTNU
Norwegian University of Science and Technology
Faculty of Engineering
Department of Structural Engineering

Eva Anita Sivertsen
Henriette Sofie Høgstedt Strehl

Flutter Analysis of Twin-Deck Configurations for a Suspension Bridge Crossing the Sulafjord

Wind Tunnel Testing and Numerical Predictions

Master's thesis in ICT, Civil and Environmental Engineering
Supervisor: Ole Øiseth

June 2021

NTNU
Norwegian University of
Science and Technology

Eva Anita Sivertsen
Henriette Sofie Høgstedt Strehl

Flutter Analysis of Twin-Deck Configurations for a Suspension Bridge Crossing the Sulafjord

Wind Tunnel Testing and Numerical Predictions

Master's thesis in ICT, Civil and Environmental Engineering
Supervisor: Ole Øiseth
June 2021

Norwegian University of Science and Technology
Faculty of Engineering
Department of Structural Engineering

NTNU
Norwegian University of
Science and Technology

Department of Structural Engineering
Faculty of Engineering
NTNU – Norwegian University of Science and Technology

ACCESSIBILITY

OPEN

MASTER THESIS 2021

SUBJECT AREA: Structural Dynamics	DATE: 10.06.2021	NO. OF PAGES: 26+80+44=150

TITLE:

Flutter analysis of twin-deck configurations for a suspension bridge crossing the Sulafjord

Flutter analyse for konfigurasjoner av dobbelt kassetverrsnitt for hengebro over Sulafjorden

BY:

Eva Anita Sivertsen
Henriette Sofie Høgstedt Strehl

SUMMARY:
Proposed in the "Ferry-free E39" project is the alternative of a twin-deck suspension bridge crossing the Sulafjord. The deep fjord surrounded by complex terrain requires a single span of 2800 m, which exceeds the longest suspension bridges today. Due to the rough coastal climate, wind-induced vibrations of the bridge deck are of major concern. At high wind velocities, violent bridge deck oscillations may lead to destructive behaviour in the absence of aerodynamic stability. To encounter the challenge, additional research is required to assess how the stability is affected by several bridge deck design variables. Twin-deck configurations of three geometric shapes and three different gaps are investigated to achieve sufficient aerodynamic stability for the suspension bridge crossing the Sulafjord. Flutter analysis is conducted for the nine configurations to estimate the stability limits. The modal parameters are obtained from global element models based on the feasibility study by Multiconsult. For the wind tunnel testing, section models are built and equipped with attachments. The static forces and self-excited forces are established from the wind tunnel tests, defining the static coefficients and aerodynamic derivatives, respectively. To predict the stability limits, the aerodynamic derivatives are approximated by 3rd order polynomials. Reliable estimates of the aerodynamic derivatives are crucial at the critical reduced frequency. Desirable is a stable bridge without encountering issues of vibrations due to vortex shedding. Thus, wind tunnel tests detecting the vortex-induced behaviour are performed. The governing instability phenomenon is assessed as multi-modal coupled flutter. The stability limits converge for the mode combination of the two first vertical symmetric modes and the first torsional symmetric mode. Despite small variations in the girder shapes, the stability limits for two of the geometric shapes proved to be superior. Evident is also a general tendency of increasing stability limit with larger gap. Deviations from the stability limit trends are substantiated by the inaccuracy of polynomial fits of the aerodynamic derivatives at the critical reduced frequency. For the three-mode flutter phenomenon, the stability limits obtained ranges between 86.0 ms^{-1} and 105.5 ms^{-1}. With a stability criterion of 75.9 ms^{-1}, all the configurations pass the instability control of the Norwegian bridge design code - N400.

RESPONSIBLE TEACHER: Professor Ole Øiseth

SUPERVISOR(S): Professor Ole Øiseth

CARRIED OUT AT: Department of Structural Engineering

Abstract

Proposed in the "Ferry-free E39" project is the alternative of a twin-deck suspension bridge crossing the Sulafjord. The deep fjord surrounded by complex terrain requires a single span of 2800 m, which exceeds the longest suspension bridges today. Due to the rough coastal climate, wind-induced vibrations of the bridge deck are of major concern. At high wind velocities, violent bridge deck oscillations may lead to destructive behaviour in the absence of aerodynamic stability. To encounter the challenge, additional research is required to assess how the stability is affected by several bridge deck design variables. Twin-deck configurations of three geometric shapes and three different gaps are investigated to achieve sufficient aerodynamic stability for the suspension bridge crossing the Sulafjord.

Flutter analysis is conducted for the nine configurations to estimate the stability limits. The modal parameters are obtained from global element models based on the feasibility study by Multiconsult (Multiconsult, 2015). For the wind tunnel testing, section models are built and equipped with attachments. The static forces and self-excited forces are established from the wind tunnel tests, defining the static coefficients and aerodynamic derivatives, respectively. To predict the stability limits, the aerodynamic derivatives are approximated by 3rd order polynomials. Reliable estimates of the aerodynamic derivatives are crucial at the critical reduced frequency. Desirable is a stable bridge without encountering issues of vibrations due to vortex shedding. Thus, wind tunnel tests detecting the vortex-induced behaviour are performed.

The governing instability phenomenon is assessed as multi-modal coupled flutter. The stability limits converge for the mode combination of the two first vertical symmetric modes and the first torsional symmetric mode. Despite small variations in the girder shapes, the stability limits for two of the geometric shapes proved to be superior. Evident is also a general tendency of increasing stability limit with larger gap. Deviations from the stability limit trends are substantiated by the inaccuracy of polynomial fits of the aerodynamic derivatives at the critical reduced frequency. For the three-mode flutter phenomenon, the stability limits obtained ranges between 86.0 ms^{-1} and 105.5 ms^{-1}. With a stability criterion of 75.9 ms^{-1}, all the configurations pass the instability control of the Norwegian bridge design code - N400 (Statens vegvesen, 2015).

Sammendrag

Prosjektet "Ferjefri E39" inkluderer et forslag om å krysse Sulafjorden med en hengebro med dobbelt-kassetverrsnitt. Den dype fjorden som omgis av et komplekst terreng er opphavet for behovet om et enkelt spenn på 2800 m. Broens spenn overgår dermed de lengste hengebroene som eksisterer i dag. På grunn av det værharde kystklimaet er vind-induserte vibrasjoner i brodekket en stor bekymring. Ved store vind hastigheter kan ukontrollerbare svingninger i brodekke føre til destruktive bevegelser ved fravær av aerodynamisk stabilitet. For å imøtekomme slike utfordringer er det behov for ytterligere forskning på hvilken innvirkning detaljer i design har på brudekkets stabilitet. Konfigurasjoner av doble kasse-tverrsnitt, med tre geometriske former og tre ulike avstander mellom kassene, er analysert med formål om å kunne oppnå tilstrekkelig aerodynamisk stabilitet for hengebroen over Sulafjorden.

Flutter analyse er anvendt for å estimere stabilitets grensene til de ni konfigurasjonene. De modale parameterne er hentet ut fra globale element modeller som er basert på mulighetsstudiet til Multiconsult (Multiconsult, 2015). Fra de statiske og selv-induserte kreftene i responsen fra ulike vind-tunnel tester hentes henholdsvis de statiske koeffisientene og aerodynamiske deriverte. For beregning av stabilitets grensene er de aerodynamiske deriverte tilnærmet med tredje grads polynomer. Avgjørende er gode estimater av de aerodynamiske deriverte for den kritiske reduserte frekvensen. I tillegg er eventuell ustabilitet forårsaket av svingninger fra virvelavløsninger kontrollert ved vind-tunnel tester som avdekker slik oppførsel.

Flutter analysen avslørte at multi-modal koblet flutter er det dominerende instabilitets fenomenet for alle konfigurasjonene. Konvergens av stabilitets grensene ble funnet for kombinasjon av de to første symmetriske vertikale modene og den første symmetriske torsjonsmoden. Selv med minimale geometriske forskjeller, skiller to av tverrsnittene seg ut med betydelig høyere stabilitets grenser. I tillegg finnes en åpenbar trend med økende stabilitets grenser for større avstander mellom brokassene. Avvik fra trendene for stabilitets grensene kan begrunnes med unøyaktighet vedrørende de polynomiske tilnærmingene av de aerodynamiske deriverte for den kritiske reduserte frekvensen. De oppnådde stabilitets grensene for de ni konfigurasjonene, basert på det nevnte tre-moders flutter fenomenet, varierte mellom 86.0 ms^{-1} og 105.5 ms^{-1}. Alle konfigurasjonene oppfyller dermed det beregnede stabilitets kravet fra Håndbok N400 på 75.9 ms^{-1} (Statens vegvesen, 2015).

Acknowledgements

Throughout the progression of our master's thesis in structural dynamics at NTNU we have received great support and assistance. We would like to express our sincere appreciation to our supervisor, Prof. Ole Øiseth. His guidance and valuable expertise has been essential, as well as his help with the processing of wind tunnel data which was important for the completion of the thesis.

We are grateful to Postdoc. Øyvind Wiig Petersen for his competence and help with the Abaqus modelling. We would also like to thank PhD candidate Oddbjørn Kildal, PhD candidate Dario Castellon and PhD candidate Niccolo Barni for consultation and interesting discussions.

Great assistance with the laboratory work was recieved from Gøran Loraas, Pål Erik Endrerud and Marius Østnor Døllner.

It has been inspiring to collaborate with a research group such devoted to the topic of our master's thesis.

Table Of Contents

List of Figures

List of Tables

Abbreviations

Acronyms

AD	Aerodynamic derivative
FE	Finite Element
G	Gap
H	Horizontal
NPRA	Norwegian Public Road Administration
NTNU	Norwegian University of Science and Technology
NTP	National Transportation Plan
S	Section
SE	Self-excited
T	Torsional
TMD	Tuned mass damper
V	Vertical
VIV	Vortex induced vibration

Symbols

α	Rotational angle of bridge deck relative to the wind flow
$\boldsymbol{\eta}$	Eigenvector, generalized coordinate vector
$\boldsymbol{\phi}$	Natural eigen-mode shape
$\tilde{\boldsymbol{K}}$,$\tilde{\boldsymbol{C}}$,$\tilde{\boldsymbol{M}}$	Modal stiffness, damping and mass matrices
$\boldsymbol{E}$	Equivalent coefficient matrix
$\boldsymbol{I}$	Identity matrix
$\boldsymbol{K}$,$\boldsymbol{M}$	Stiffness and mass matrices
$\boldsymbol{X}$	Motion histories matrix
$\ddot{r}_z$	Vertical acceleration

$\dot{r}_y$,$\dot{r}_z$,$\dot{r}_\theta$	Horizontal, vertical and torsional velocities
$\hat{E}$,$\hat{\boldsymbol{E}}$	Non-dimensional impedance, non-dimensional impedance matrix
κ_{ae},$\boldsymbol{\kappa_{ae}}$	Aerodynamic modal stiffness contributions, aerodynamic modal stiffness contributions matrix
λ	Eigenvalue
ν	Kinematic viscosity of air
ω	Angular frequency of motion (rads^{-1})
ω_j	Still air eigenfrequency associated with mode shape j
ω_r	Resonance frequency associated with critical wind velocity
ψ	Mode shape similarity factor
ρ	Air density
$\tilde{C}_{ae}$,$\tilde{\boldsymbol{C}}_{\boldsymbol{ae}}$	Aerodynamic modal damping, aerodynamic modal damping matrix
$\tilde{K}_{ae}$,$\tilde{\boldsymbol{K}}_{\boldsymbol{ae}}$	Aerodynamic modal stiffness, aerodynamic modal stiffness matrix
$\tilde{m}_\theta$	Modally equivalent and evenly distributed mass in θ direction
$\tilde{m}_z$	Modally equivalent and evenly distributed mass in z direction
$\tilde{Q}$,$\tilde{\boldsymbol{Q}}$	Modal wind load, modal wind load matrix
$\tilde{Q}_{ae}$,$\tilde{\boldsymbol{Q}}_{\boldsymbol{ae}}$	Modal self-excited load, modal self-excited load matrix
ζ,$\boldsymbol{\zeta}$	Structural damping ratio, structural damping ratio matrix
ζ_{ae},$\boldsymbol{\zeta}_{ae}$	Aerodynamic modal damping ratio contributions, aerodynamic modal damping ratio contributions matrix
$A_1^* - A_6^*$	Aerodynamic derivatives associated with the torsional motion
B	Width
C'_D, C'_L, C'_M	First derivative of the static coefficients
C_D, C_L, C_M	Static coefficients for drag, lift and pitching moment
D	Characteristic dimension
e_1	Local 1-coordinate to the center of mass
e_2	Local 2-coordinate to the center of mass
f_s	Vortex shedding frequency
f_v	Frequency of wake vortex formation
$H_1^* - H_6^*$	Aerodynamic derivatives associated with the cross-wind motion
i	Imaginary unit

I_{11}	Rotary inertia around the center of mass about the local 1-axis
I_{22}	Rotary inertia around the center of mass about the local 2-axis
j	Mode shape index
K	Reduced frequency
L	Total length of span
L_{exp}	Length of span exposed to wind flow
m	Mass per unit length
n	Sample number
n_s	Dominant shedding frequency
N_{mod}	Number of modes
$P_1^* - P_6^*$	Aerodynamic derivatives associated with the along-wind motion
q^{SE},$\boldsymbol{q^{SE}}$	Distributed self-excited force, distributed self-excited forces matrix (Nm^{-1})
q_L,q_D,q_M	Lift force, drag force and pitching moment
r_y,r_z,r_θ	Horizontal, vertical and torsional displacements
Re	Reynolds number
Sc	Scruton number
St	Strouhal number
t	Time
V	Mean wind velocity
V_r	Reduced velocity
V_s	Velocity causing vortex-induced vibrations
V_{cr}	Critical wind velocity, stability limit

Chapter 1

Introduction

With worldwide demand for longer span bridges follows great challenges in structural design. In Norway, the Norwegian Parliament aims to replace the current ferry connections along the E39 trailing the west coast. The Sulafjord is among the largest fjord-crossings in the "Ferry-free E39" project. Because of the deep fjord exceeding 400 m depth, the alternative of a single-span suspension bridge crossing the Sulafjord is suggested (Multiconsult, 2015). With a main span of 2800 m, the suspension bridge crossing the Sulafjord will surpass the longest suspension bridges today. The complex mountain terrain and the rough weather conditions towards the open ocean make the wind-induced response a crucial aspect of the bridge design (Cheynet et al., 2016; Fenerci et al., 2017; Lystad et al., 2018). Until the collapse of the Tacoma Narrows Bridge in 1940, there was limited understanding of the wind-structure interaction of long-span suspension bridges. The models currently used for wind-induced response are based on finite element formulations, which accounts for unsteady self-excited forces (Davenport, 1962; Scanlan and Tomko, 1971; Jain et al., 1996), non-linearities (Chen and Kareem, 2003; Diana et al., 2008), skew winds (Zhu and Xu, 2005) and non-stationary winds (Hu et al., 2013). In the last decades, multi-box girders have been introduced for long-span suspension bridges to alter the aerodynamic behaviour. Innovative designs were adopted for the Xihoumen Bridge twin-box girder and the Messina Straits crossing composed of three box girders (Gimsing and Georgakis, 2012).

The thesis aims to achieve a sufficient aerodynamic stability of the twin-deck suspension bridge crossing the Sulafjord. The flutter phenomenon is investigated, defining the instability at high wind velocities. To increase the aerodynamic stability, a twin-box girder configuration is proposed. An increase in the gap have been found to improve the aerodynamic stability of twin-decks (Sato et al., 2002; Fujino and Siringoringo, 2013; Yang et al., 2015). However, research is required to assess how several bridge design variables affect the onset of flutter. Thus, nine configurations of various girder shapes and gaps are explored. The aerodynamic stability limit is estimated by performing flutter analysis. Global element models are created to obtain the modal parameters. The static forces and self-excited forces are established from wind tunnel tests, defining the static coefficients and aerodynamic derivatives, respectively. Encountered by twin-box girders are vibrations due to vortex shedding (Kwok et al., 2012; Laima and Li, 2015; Álvarez et al., 2018). Therefore, the vortex-induced vibration performance is evaluated.

The chapter divisions present the structure of the thesis. Chapter 2 introduces the Sulafjord site and the stability criterion. The literature review in Chapter 3 presents the background theory with an understanding that the reader has knowledge of the basic structural dynamics. In Chapter 4, an overview of twin-box girders and control measures of existing long-span cable-supported bridges is presented. Chapter 5, 6 and 7 gathers the methodology of the thesis. In Chapter 5, the selection of the girder design is deliberated and the chosen configurations are presented. The global element models used to attain the modal parameters are introduced in Chapter 6. The wind tunnel tests are described in Chapter 7, including the building of the section models, the experimental setup and the testing procedure. The results are presented, analysed and discussed in Chapter 8. The conclusions and proposals for further work are presented in Chapter 9 and Chapter 10, respectively.

Chapter 2

Bridge Crossing of the Sulafjord

The bridge crossing of the Sulafjord is a part of the E39 Coastal Highway Route along the west coast of Norway. As seen in Figure 2.1(a), the E39 extends from Kristiansand to Trondheim, with a length of approximately 1100 km. Due to the coastal topography of Norway being dominated by fjords and islands, the E39 depends on several ferry crossings to stay connected. These ferry crossings, in addition to other factors, make the E39 route a very time-consuming distance. Since the area is one of the largest export regions in Norway and houses several large cities, it would be beneficial to make the travel distance more time-efficient. Therefore, The Norwegian Government decided that the National Transportation Plan (NTP) for 2018-2029 should include an improvement of the entire E39 Coastal Highway Route (Norwegian Public Roads Administration, 2020).

An essential part of the improvements is the project ”Ferry-free E39” which is administrated by the Norwegian Public Roads Administration (NPRA). It’s aim is to replace the ferry connections with permanent fjord crossings such as bridges or sub-sea tunnels. A feasibility study of the Sulafjord crossing was conducted by Multiconsult in 2015 (Multiconsult, 2015). The proposed location of the bridge is outlined with a black line in Figure 2.1(b). It would replace the current ferry crossing from Festøya to Leirvågen with a rearranged E39 requiring two new fjord crossings. The original path of the E39 is indicated by the red lines.

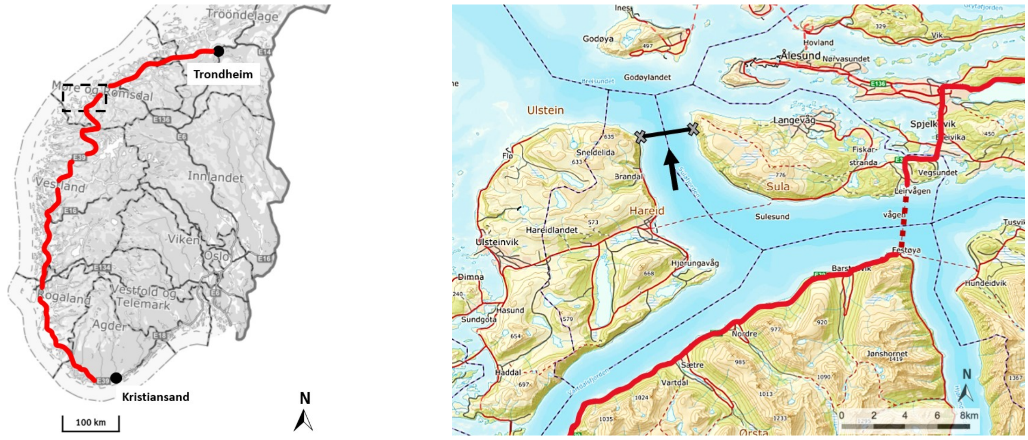

(a) The E39 Coastal Highway Route (b) Proposed location of the Sulafjord bridge crossing

Figure 2.1: Overview of E39 and the area surrounding Ålesund (Maps: ©Kartverket)

The fjord crossings can be wide as well as deep and are often exposed to tough coastal climate providing challenging conditions for permanent bridge crossings. At the proposed location the fjord has a width of approximately 3200 m and a depth exceeding 400 m. The bridge itself would be a suspension bridge with two towers and a main span of 2800 m (Multiconsult, 2015). This would be a significant increase in span length from the largest suspension bridge span today, which belongs to the Akashi-Kaikyo bridge in Japan with a main span of 1991 m (Brancaleoni, 2016). The 1915Çanakkale Bridge in Turkey is under construction, at the time of completion it will possess a span of 2023 m thereupon becoming the longest span in the world (Generate Directorate of Highways, 2020).

2.1 Stability Criterion

The stability requirement is derived for the location of the Sulafjord bridge crossing. To calculate the critical wind speed (V_{crit}), indicating the lower stability criteria for the Sulafjord, the following equation from the bridge design manual N400 is used (Statens vegvesen, 2015)

$$\frac{V_{crit}}{\gamma_{V_{crit}}} \geq V_m(z = z_m, T = 600\,s, RP = 500\,yrs) \tag{2.1}$$

and

$$\gamma_{V_{crit}} = 1.6$$

According to N400, the mean wind value (V_m) should be taken at a mean height of the terrain (z_m) and yield for a 600 second time-interval (T) with a return-period (RP) of 500 years.

The mean wind speed is obtained from the extreme value statistics for a return period of 500 years. The mean wind probability density function was adapted as a Weibull distribution based on hindcast data (Kjeller Vindteknikk, 2019) from the Sulafjord center location as reported in Castellon et al. (2021). A final value of the mean wind speed is found as

$$V_m(T = 600\,s, RP = 500\,yrs) = \underline{47.46}\;ms^{-1}$$

resulting in a stability criterion for the Sulafjord bridge crossing of

$$V_{crit} \geq 1.6 \cdot V_m = \underline{\underline{75.94}}\;ms^{-1} \tag{2.2}$$

Chapter 3

Literature Review

A brief explanatory chapter is included to secure a basic understanding of the topics introduced in the master's thesis. The presented theory is summarized and further reading, as well as the books and articles cited in the chapters, can be found in the reference list.

3.1 Modal Theory

Modal analysis uses the natural mode shapes of a structure to determine its free vibration response to different load types. An eigenvalue problem is established to derive the systems natural mode shapes of vibration (ϕ) and corresponding natural frequencies (ω). A modal frequency domain approach demands that a sufficiently accurate eigenvalue solution is available. The desired accuracy of the results is obtained by including the necessary number of modes (N_{mod}) in the calculations (Strømmen, 2010).

The bridge deck of a suspension bridge can be idealized as a flexible line-like structure with x as the horizontal position in the span-wise direction and y-axis in the transverse horizontal along-wind direction. The motion of the bridge deck can then be described by mode shape vectors (ϕ_j) with components in the vertical (z), horizontal (y) and torsional (θ) direction, all as functions of x. The natural eigenmode shape vector ($\boldsymbol{\phi}_j$) and the generalized coordinate (η_j) associated with mode number j of the multi-degree-of-freedom (MDOF) system of a bridge girder are expressed as

$$\boldsymbol{\phi}_j(x) = \begin{bmatrix} \phi_y & \phi_z & \phi_\theta \end{bmatrix}^T \tag{3.1}$$

For a linear system, the total displacements can be derived by superposition of the response from each mode ($r_j(x)$) over the total number of modes. A single-mode response is taken as the product between the generalized coordinates and the natural eigenmodes, defining the total response as

$$\boldsymbol{r}(x,t) = \sum_{j=1}^{N_{mod}} \boldsymbol{\phi}_j(x) \cdot \eta_j(t) = \boldsymbol{\phi}(x) \cdot \boldsymbol{\eta}(t) \tag{3.2}$$

The mode shape matrix and the vector of generalized coordinates corresponding to N_{mod} modes

$$\begin{aligned}\boldsymbol{\phi}(x) &= \begin{bmatrix}\boldsymbol{\phi}_1(x) & ... & \boldsymbol{\phi}_j(x) & ... & \boldsymbol{\phi}_{N_{mod}}(x)\end{bmatrix}\\ \boldsymbol{\eta}(t) &= \begin{bmatrix}\eta_1(t) & ... & \eta_j(t) & ... & \eta_{N_{mod}}(t)\end{bmatrix}^T\end{aligned}$$

By inserting Equation 3.2 in the systems equilibrium equations and performing integration over the length of the span, the equation of motion in the modal frequency domain is obtained.

$$\tilde{\boldsymbol{M}}_0\ddot{\boldsymbol{\eta}}(t) + \tilde{\boldsymbol{C}}_0\dot{\boldsymbol{\eta}}(t) + \tilde{\boldsymbol{K}}_0\boldsymbol{\eta}(t) = \tilde{\boldsymbol{Q}}(t) + \tilde{\boldsymbol{Q}}_{ae}(t, \eta, \dot{\eta}, \ddot{\eta}) \tag{3.3}$$

Here, modal mass, damping and stiffness matrices, given as $\tilde{\boldsymbol{M}}_0$, $\tilde{\boldsymbol{C}}_0$ and $\tilde{\boldsymbol{K}}_0$ respectively, all obtained in still air, indicated by the zero indexes. The matrices of the left-hand side in are defined as

$$\begin{aligned}\tilde{\boldsymbol{M}}_0 &= diag[\tilde{M}_j] & \tilde{M}_j &= \int_L (\boldsymbol{\phi}_j^T\, \boldsymbol{M}_0\, \boldsymbol{\phi}_j)\\ \tilde{\boldsymbol{C}}_0 &= diag[\tilde{C}_j] & \tilde{C}_j &= 2\,\tilde{M}_j\,\omega_j\,\zeta_j\\ \tilde{\boldsymbol{K}}_0 &= diag[\tilde{K}_j] & \tilde{K}_j &= \omega_j^2\,\tilde{M}_j\end{aligned}$$

The diagonal matrices of size 1xN_{mod} introduce a number of N_{mod} uncoupled modal equations. The damping ratio ζ decreases the displacement amplitude in the DOFs for each natural period of vibration $2\pi/\omega_n$.

Referring on the right-hand side of Equation 3.3, $\tilde{\boldsymbol{Q}}(t)$ is the total modal wind load while $\tilde{\boldsymbol{Q}}_{ae}(t, \eta, \dot{\eta}, \ddot{\eta})$ accounts for the motion induced loads of the structure. Both load vectors are derived by integration over the length of the bridge span subjected to wind flow (L_{exp}) as follows

$$\tilde{\boldsymbol{Q}}_j(t) = \int_{L_{exp}} \boldsymbol{\phi}_j^T \cdot \boldsymbol{q}\, dx = \int_{L_{exp}} \boldsymbol{\phi}_j^T \cdot \begin{bmatrix} q_y \\ q_z \\ q_\theta \end{bmatrix} \cdot dx \tag{3.4}$$

$$\tilde{\boldsymbol{Q}}_{ae_j}(t, \eta, \dot{\eta}, \ddot{\eta}) = \int_{L_{exp}} \boldsymbol{\phi} j^T \cdot \boldsymbol{q^{SE}}\, dx = \int_{L_{exp}} \boldsymbol{\phi}_j^T \cdot \begin{bmatrix} q_y^{SE} \\ q_z^{SE} \\ q_\theta^{SE} \end{bmatrix} \cdot dx \tag{3.5}$$

with the load vectors having three components of load per unit length representing drag, lift and moment (Strømmen, 2010).

3.2 Wind and Motion Induced Forces

Wind is a spatiotemporal phenomenon of dynamic and random nature (Fujino and Siringoringo, 2013). By considering a time period of typically 10 minutes, the wind speed can be assessed as a mean component (mean wind) and a fluctuating component (gust). The main flow is assumed to act perpendicular to the longitudinal bridge direction. For a long-span bridge, wind-induced vibrations are of major concern. As illustrated in Figure 3.1 the occurrence of wind and motion-induced forces depends on the mean wind velocity (Strømmen, 2010). The static response diverts from being proportional to the mean wind velocity squared when self-excited (SE) forces are encountered. The dynamic response will generally originate from vortex shedding forces, buffeting forces and SE forces with increasing mean wind velocity. At high mean wind velocities, the response may increase rapidly as it approaches unstable behaviour.

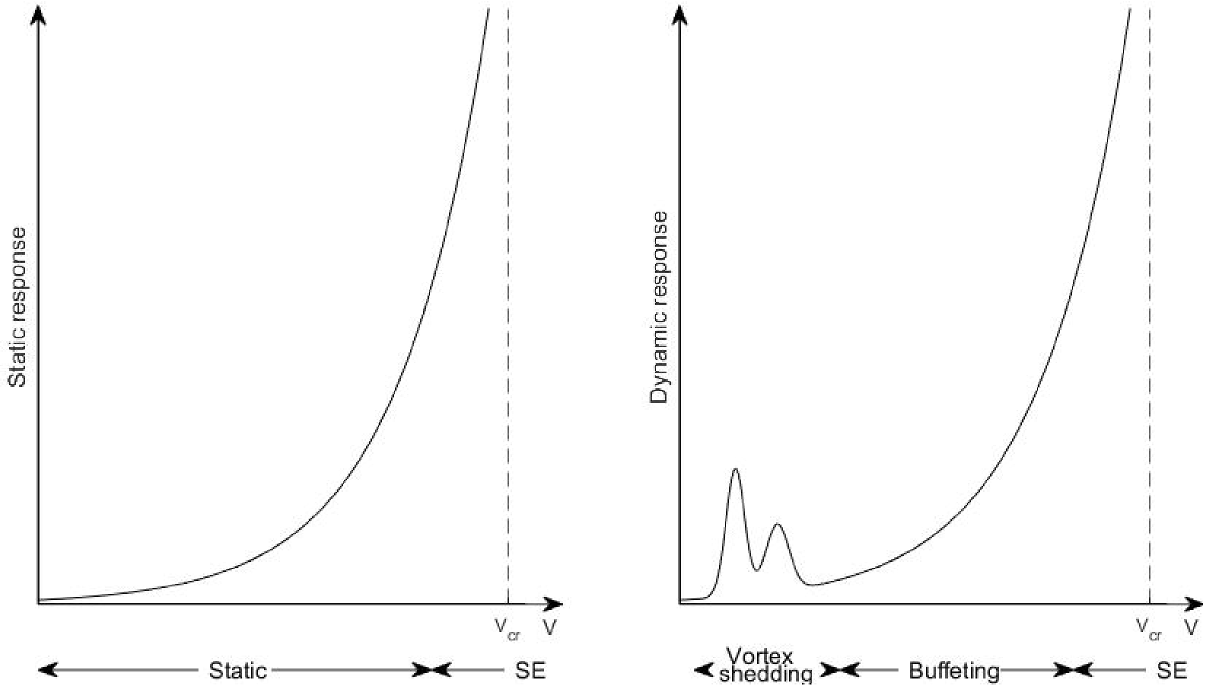

Figure 3.1: Typical response variation with mean wind velocity and causative forces

3.2.1 Static Forces

The mean wind induces static forces on a bridge deck in a deflected position through aerostatic pressures. By applying strip theory, only three force components in the flow axes require consideration: the lift force (q_L), the drag force (q_D) and the pitching moment (q_M). The static forces are utilized to determine the static coefficients (Tamura and Kareem, 2013).

3.2.2 Vortex Shedding Forces

The flexible structure of the bridge deck of a suspension bridge is prone to exhibit fluctuating motion due to the vortex shedding forces, also known as vortex-induced vibrations (VIVs). If the shedding frequency becomes equal to the eigen-frequencies of the first vertical or torsional vibration modes, resonance will occur. As the structure interacts with the wind flow, the flow gets separated and vortices shed behind the structure. The slender geometry of a bridge deck causes the vortices to shed alternately with a certain shedding frequency, f_s, inflicting vortex shedding forces on the bridge deck. The along wind vortex shedding forces are of less influence and can be neglected due to the dominance of the across wind forces and torsional vortex shedding forces (Strømmen, 2010).

3.2.3 Buffeting Forces

The velocity fluctuations in a wind flow together with any motion-induced contributions can cause a buffeting mechanism where vibrating motion is initiated in the bridge deck. Even though the buffeting forces occurs at higher wind speeds than the vortex shedding forces, the forces rarely appear exclusively alone (Strømmen, 2010). The vibrations are usually harmless to the bridge structure but can contribute to fatigue and serviceability issues. The buffeting mechanism depends on the turbulence of the oncoming wind flow, which will not be studied in this thesis but should be included in further analysis of the bridge decks.

3.2.4 Self-excited Forces

The movements of the bridge deck immersed in wind affects the surrounding flow. The deck displaces the air causing changes in the relative velocity. Vibrations and resulting self-excited forces are initiated by the interaction between the bridge deck and the flow. The motion-dependent forces are commonly expressed in terms of aerodynamic derivatives (Fujino and Siringoringo, 2013).

3.3 Motion Induced Instabilities

Unstable behaviour is induced when even the smallest increase in mean wind velocity triggers an infinite displacement response. A point is reached at which the structure is unable to damp the motions caused by the addition of aerodynamic energy. The phenomenon is illustrated in Figure 3.1, where the lowest mean wind velocity causing unstable behaviour (V_{cr}) represents the stability limit. It is distinguished between static and dynamic response. The static response occurs for zero frequency ($\omega = 0$), while the dynamic response is narrow-banded and centred on the resonance frequency (ω_r). Motion induced instabilities are commonly classified according to the type of displacement (Table 3.1). For suspension bridges in general, the dynamic instability phenomena are of greater interest than the static instability phenomenon due to the lower critical wind velocity (Gimsing and Georgakis, 2012).

Table 3.1: Classification of motion induced instabilities

Motion induced instability	Description
Static divergence	Static response in torsion
Galloping	Dynamic response in vertical direction
Torsional flutter	Dynamic response in torsion
Coupled flutter	Dynamic response in combined vertical and torsional motion

The stability limit is determined from the properties of the N_{mod} by N_{mod} impedance matrix

$$\hat{\boldsymbol{E}}_\eta(\omega, V) = \left\{ \boldsymbol{I} - \boldsymbol{\kappa_{ae}} - \left(\omega \cdot diag\left[\frac{1}{\omega_j}\right]\right)^2 + 2i\omega \cdot diag\left[\frac{1}{\omega_j}\right]\left(\boldsymbol{\zeta} - \boldsymbol{\zeta_{ae}}\right)\right\} \tag{3.6}$$

where

$$\kappa_{ae_j} = \frac{\tilde{K}_{ae_j}}{\omega_j^2 \tilde{M}_j} \quad and \quad \zeta_{ae_j} = \frac{\tilde{C}_{ae_j}}{2\omega_j \tilde{M}_j}$$

The impedance matrix is the inverse of the frequency response function. $\boldsymbol{\kappa_{ae}}$ and $\boldsymbol{\zeta_{ae}}$ is the aerodynamic modal stiffness contributions matrix and the aerodynamic damping ratio contributions matrix, which is defined as follows:

$$\boldsymbol{\kappa_{ae}} = \begin{bmatrix} \kappa_{ae_{zz}} & \kappa_{ae_{z\theta}} \\ \kappa_{ae_{\theta z}} & \kappa_{ae_{\theta\theta}} \end{bmatrix} = \begin{bmatrix} \frac{\rho B^2}{2\tilde{m}_z}\left(\frac{\omega_z(V)}{\omega_z}\right)^2 H_4^* \frac{\int_{L_{exp}} \phi_z^2 dx}{\int_L \phi_z^2 dx} & \frac{\rho B^3}{2\tilde{m}_z}\left(\frac{\omega_z(V)}{\omega_z}\right)^2 H_3^* \frac{\int_{L_{exp}} \phi_z \phi_\theta dx}{\int_L \phi_z^2 dx} \\ \frac{\rho B^3}{2\tilde{m}_\theta}\left(\frac{\omega_\theta(V)}{\omega_\theta}\right)^2 A_4^* \frac{\int_{L_{exp}} \phi_\theta \phi_z dx}{\int_L \phi_\theta^2 dx} & \frac{\rho B^4}{2\tilde{m}_\theta}\left(\frac{\omega_\theta(V)}{\omega_\theta}\right)^2 A_3^* \frac{\int_{L_{exp}} \phi_\theta^2 dx}{\int_L \phi_\theta^2 dx} \end{bmatrix} \tag{3.7}$$

$$\boldsymbol{\zeta_{ae}} = \begin{bmatrix} \zeta_{ae_{zz}} & \zeta_{ae_{z\theta}} \\ \zeta_{ae_{\theta z}} & \zeta_{ae_{\theta\theta}} \end{bmatrix} = \begin{bmatrix} \frac{\rho B^2}{4\tilde{m}_z}\left(\frac{\omega_z(V)}{\omega_z}\right)^2 H_1^* \frac{\int_{L_{exp}} \phi_z^2 dx}{\int_L \phi_z^2 dx} & \frac{\rho B^3}{4\tilde{m}_z}\left(\frac{\omega_z(V)}{\omega_z}\right)^2 H_2^* \frac{\int_{L_{exp}} \phi_z \phi_\theta dx}{\int_L \phi_z^2 dx} \\ \frac{\rho B^3}{4\tilde{m}_\theta}\left(\frac{\omega_\theta(V)}{\omega_\theta}\right)^2 A_1^* \frac{\int_{L_{exp}} \phi_\theta \phi_z dx}{\int_L \phi_\theta^2 dx} & \frac{\rho B^4}{4\tilde{m}_\theta}\left(\frac{\omega_\theta(V)}{\omega_\theta}\right)^2 A_2^* \frac{\int_{L_{exp}} \phi_\theta^2 dx}{\int_L \phi_\theta^2 dx} \end{bmatrix} \tag{3.8}$$

Equations 3.7 and 3.8 show how motion-induced instabilities depend on the eight aerodynamic derivatives (ADs) associated with instability. For infinite displacement response to occur, the absolute value of the determinant to the impedance matrix must equal zero (Equation 3.9). The solution to the eigenvalue problem consists of N_{mod} roots, each associated with an unstable behaviour.

$$\left| det\left(\hat{\boldsymbol{E}}_\eta(\omega, V)\right)\right| = 0 \tag{3.9}$$

3.3.1 Static Divergence

A deflected position of the bridge deck in still-air motion introduces aerostatic pressures and consequently the loss of torsional stiffness. For a certain wind velocity recognized as the torsional divergence velocity, the torsional stiffness will vanish completely (Gimsing and Georgakis, 2012). By incorporating a resonant frequency of zero, the impedance matrix reduces to zero when the aerodynamic rotational stiffness contribution equals 1 (Strømmen, 2010).

$$\hat{E}_\eta(\omega_r = 0, V_{cr}) = 1 - \kappa_{ae_{\theta\theta}} = 0 \tag{3.10}$$

3.3.2 Galloping

Galloping, also known as bending flutter, is the aeroelastic instability in which the bridge deck exhibits large-amplitude oscillations in the vertical direction. The wind-induced phenomenon is caused by the shift in pressure distributions around the cross-section due to initial motion changing the angle of attack of the wind flow relative to the deck (Fujino and Siringoringo, 2013). Seen as the oscillating motion of galloping does not involve rotation nor horizontal displacement of the bridge deck, its shape can be described using only the vertical component. The lowest frequency at which the mode shape occurs is the resonant frequency of the mode shape. Introducing the relation $\omega_r = \omega_z(V_{cr})$ in the impedance matrix and obtaining a reduced expression as

$$\hat{E}_\eta\left(\omega_r = \omega_z(V_{cr}), V_{cr}\right) = 1 - \kappa_{ae_{zz}} - \left(\tfrac{\omega_r}{\omega_z}\right)^2 + 2i\left(\zeta_z - \zeta_{ae_{zz}}\right)\left(\tfrac{\omega_r}{\omega_z}\right) \tag{3.11}$$

A resonance frequency representing the vertical stability limit may be derived as below when setting the real and imaginary part of 3.11 equal to zero

$$\omega_r = \omega_z\left(1 + \tfrac{\rho B^2}{2\tilde{m}_z} H_4^* \tfrac{\int_{Lexp}\phi_z^2 dx}{\int_L \phi_z^2 dx}\right)^{-1/2} \tag{3.12}$$

with corresponding damping properties of

$$\zeta_z = \zeta_{ae_{zz}} = \frac{\rho B^2}{4\tilde{m}_z}\frac{\omega_r}{\omega_z} H_1^* \frac{\int_{Lexp}\phi_z^2 dx}{\int_L \phi_z^2 dx} \tag{3.13}$$

H_4^* and H_1^* are the stiffness and damping related ADs associated with galloping, respectively.

3.3.3 Torsional flutter

Unlike galloping, torsional flutter is an unsteady phenomenon. As the bridge deck experiences twisting motion, it displaces the surrounding air. Changes in the relative velocity of the bridge deck introduce the effect of added mass (Tamura and Kareem, 2013). Therefore, the unsteady self-excited forces are represented by aerodynamic derivatives as a function of reduced velocity. Torsional flutter occurs when the total damping of the system in torsional motion equals zero. The impedance matrix is reduced by inserting the lowest natural frequency associated with the torsional mode (Strømmen, 2010).

$$\hat{E}_\eta\left(\omega_r = \omega_\theta(V_{cr}), V_{cr}\right) = 1 - \kappa_{ae_{\theta\theta}} - \left(\tfrac{\omega_r}{\omega_\theta}\right)^2 + 2i\left(\zeta_\theta - \zeta_{ae_{\theta\theta}}\right)\left(\tfrac{\omega_r}{\omega_\theta}\right) \tag{3.14}$$

By setting the real and imaginary part of Equation 3.14 equal to zero, the dynamic stability limit in torsion may be identified at a resonance frequency of

$$\omega_r = \omega_\theta\left(1 + \tfrac{\rho B^4}{2\tilde{m}_\theta} A_3^* \tfrac{\int_{Lexp}\phi_\theta^2 dx}{\int_L \phi_\theta^2 dx}\right)^{-1/2} \tag{3.15}$$

and with damping properties of

$$\zeta_\theta = \zeta_{ae_{\theta\theta}} = \frac{\rho B^4}{4\tilde{m}_\theta}\frac{\omega_r}{\omega_\theta}A_2^*\frac{\int_{Lexp}\phi_\theta^2 dx}{\int_L \phi_\theta^2 dx} \tag{3.16}$$

A_3^* and A_2^* are the stiffness and damping related ADs associated with torsional flutter, respectively.

3.3.4 Coupled flutter

Coupled flutter is the instability of SE motion where displacement responses in vertical and torsional direction couples into a joint resonant motion (Strømmen, 2010). Each displacement response corresponds to the first vertical or torsional eigenmode of the bridge deck in which one component dominates, either ϕ_z or ϕ_θ respectively. Required for the onset of coupling is the shape-wise similarity of the modes. The coupling of the motion can only occur if the off-diagonal terms of the $\hat{\boldsymbol{E}}_\eta$ matrix in Equation 3.6 have non-zero values. In terms of identifying the coupled flutter stability limit, the determinant of the impedance matrix needs to be zero.

$$\left| det(\hat{\boldsymbol{E}}_\eta(\omega_r, V_{cr}))\right| = 0 \tag{3.17}$$

The combined resonant motion of the two eigenmodes, defines

$$\omega_r = \omega_z(V_{cr}) = \omega_\theta(V_{cr}) \tag{3.18}$$

The analysis is most commonly conducted in the frequency domain due to the flutter derivatives being functions of reduced frequency (Fujino and Siringoringo, 2013). An iterative procedure is then required to solve Equation 3.17 as the identification of the AD's in the impedance matrix $\hat{\boldsymbol{E}}_\eta(\omega, V)$ demands known values of ω_r and V_{cr}.

3.4 Experimental Fluid Dynamics

Analytical solutions to the flutter problem of bridge decks are proven unsatisfactory, clarifying the need for experimental fluid dynamics. Scaling laws are used to determine the dynamic similarity between different experimental cases and predict bridge performance from model observations. The static forces and the SE forces are recorded from laboratory experiments to model the static coefficients and the aerodynamic derivatives, respectively.

3.4.1 Scaling laws

Scaling laws are applied to obtain similitude between the bridge and the section models tested in the wind tunnel. From dimensional analysis, it is found that while the governing equations and fundamental laws maintain, the downsizing leads to disruption in the equilibrium of forces that dominate. Scaling laws are utilized to describe the variation of physical quantities with the size of the system while the other quantities remain constant. Based on the Π-theorem of Buckingham a set of dimensionless parameters must be equal for the real structure and the section model (Buckingham, 1914). It is essential to employ dimensional parameters to predict structure performance from model observations. In the thesis, the dimensionless parameters considered are (Gimsing and Georgakis, 2012):

Reduced frequency: $K = \frac{B\omega}{V}$

Strouhal number: $S_t = \frac{f_s D}{V_s}$

Reduced velocity: $V_r = \frac{V}{B\omega}$

Scruton number: $S_c = \frac{m\zeta}{\rho D^2}$

Reynolds number: $Re = \frac{VD}{\nu}$

Where B is the width; ω is the angular frequency of motion; V is the mean wind velocity; ν is the kinematic viscosity of air (approx. $1.15 \times 10^{-5}\ m^2 s^{-1}$); f_s is the vortex shedding frequency; D is the characteristic dimension set to the girder depth; V_s is the velocity at which vortices are shed; m is the mass per unit length; ρ is the air density and ζ is the structural damping ratio which may be found from direct measurements from the logarithmic decrement of the envelope (Chopra, 2012).

The relative importance between the inertia forces and viscous forces of the fluid is expressed through the Reynolds number. The dynamic forces of traditional bluff bridge decks appear to be independent of the Reynolds number. However, the dynamic forces of the streamlined sections commonly used today show Reynolds number dependency. The Stonecutters Bridge girder reveals a 30% variation in drag force coefficient with wind speeds (Larose and D'Auteuil, 2006). Similarly to the effect of sharp edges of bluff girders, fixing the location of flow separation can reduce the Reynolds number dependency of streamlined sections (Lee et al., 2014).

The Strouhal number represents the non-dimensional vortex shedding frequency and is a critical parameter for VIVs. Considering twin-decks, the Strouhal number has been found to increase with increasing gap (Kwok et al., 2012; Laima and Li, 2015; Álvarez et al., 2018). Modifications causing an increase in the Strouhal number makes it more difficult to achieve the serviceability requirements of the bridge.

The main cables and hangers of suspension bridges are prone to vibration due to their low damping, high flexibility and small mass. The Scruton number is a non-dimensional mass-damping parameter used to evaluate the propensity of cables to vibrate due to dry inclined galloping and rain-wind-induced vortex shedding. According to Gimsing and Georgakis (2012), $S_c > 10$ is considered appropriate to avoid such vibrations for smooth cables subjected to typical wind velocities.

3.4.2 Static Coefficients

When performing static tests with rotation of the deck, the static coefficients can be derived as functions of the angle of inclination (α) of the bridge deck relative to the mean wind flow. The force and moment coefficients, C_D, C_L and C_M, establish a relation of the measured static forces to a chosen reference area (Strømmen, 2010). By analyzing magnitude and trend with respect to the angle α the different static coefficients give insights to pressure distributions around the bridge deck girders and can reveal Reynolds dependency. The relation to the static forces can be defined in the following manner

$$\begin{bmatrix} C_D(\alpha) \\ C_L(\alpha) \\ C_M(\alpha) \end{bmatrix} = \frac{1}{\frac{1}{2}\rho V^2 D} \cdot \begin{bmatrix} q_D \\ \frac{D}{B} q_L \\ \frac{D}{B^2} q_M \end{bmatrix} \tag{3.19}$$

where q_D, q_L and q_M are the measured static forces for drag, lift and moment per unit length. B and D are the chosen reference width and depth respectively while ρ denotes the air-density and V is the mean wind velocity.

Seen as the static load coefficients have a non-linear variation, it is preferable to simplify their curves. By adapting quasi-steady theory one can utilize the following linear approximation

$$\begin{bmatrix} C_D(\alpha) \\ C_L(\alpha) \\ C_M(\alpha) \end{bmatrix} = \begin{bmatrix} C_D(\bar{\alpha}) \\ C_L(\bar{\alpha}) \\ C_M(\bar{\alpha}) \end{bmatrix} + \alpha_f \cdot \begin{bmatrix} C'_D(\bar{\alpha}) \\ C'_L(\bar{\alpha}) \\ C'_M(\bar{\alpha}) \end{bmatrix} \tag{3.20}$$

here, a mean angle $\bar{\alpha}$ and the fluctuating part of α namely α_f are introduced together with the first derivative of the coefficients with respect to the angle of incidence. These derivatives, C'_D, C'_L and C'_D, describe the slopes of the static coefficients dependant on $\bar{\alpha}$. The quasi-steady assumptions can then give insights into the global trends and the tendency of the structure to exhibit different instabilities such as galloping and torsional flutter (Chen and Kareem, 2002).

3.4.3 Aerodynamic Derivatives

The study of aerodynamic instabilities originated from the aerospace industry. A theory was developed for the flutter problem of aircraft wings with a thin airfoil assumption by Theodorsen (1949) and further adopted for the wind-induced vibrations of bridges by Scanlan and Tomko (1971). ADs are used to define the SE forces and evaluate the propensity of the bridge to become unstable at high wind velocities. Assuming single harmonic motion and linear behaviour, the following unsteady SE forces on the bridge deck are obtained by Scanlan and Tomko (1971). In compact form the SE forces are expressed as:

$$\boldsymbol{q^{SE}} = \boldsymbol{C_{ae}}\dot{\boldsymbol{r}} + \cdot\boldsymbol{K_{ae}}\boldsymbol{r} \tag{3.21}$$

where

$$\boldsymbol{q^{SE}} = \begin{bmatrix} q_y^{SE} \\ q_z^{SE} \\ q_\theta^{SE} \end{bmatrix} \qquad \dot{\boldsymbol{r}} = \begin{bmatrix} \dot{r}_y \\ \dot{r}_z \\ \dot{r}_\theta \end{bmatrix} \qquad \boldsymbol{r} = \begin{bmatrix} r_y \\ r_z \\ r_\theta \end{bmatrix}$$

$$\boldsymbol{C}_{ae} = \frac{\rho V B K}{2} \begin{bmatrix} P_1^* & P_5^* & BP_2^* \\ H_5^* & H_1^* & BH_2^* \\ BA_5^* & BA_1^* & B^2A_2^* \end{bmatrix} \qquad \boldsymbol{K}_{ae} = \frac{\rho V^2 K^2}{2} \begin{bmatrix} P_4^* & P_6^* & BP_3^* \\ H_6^* & H_4^* & BH_3^* \\ BA_6^* & BA_4^* & B^2A_3^* \end{bmatrix}$$

P_k^*, H_k^* and A_k^* for $k = [1, 6]$ are the dimensionless coefficients termed ADs or flutter derivatives associated with drag, lift and pitching moment, respectively. The self-excited forces are functions of ADs, reduced frequency (K), mean wind velocity (V), air density (ρ), section width (B), displacements (r) and velocities ($\dot{r}$). By being associated with velocity- or displacement-proportional forces, the ADs are either damping or stiffness related.

The influence of ADs on the stability limit remains to be understood completely. Studies have verified that the influence of ADs can vary according to the classification of motion-induced instabilities (Fujino and Siringoringo, 2013; Gimsing and Georgakis, 2012; Chen, 2007; Strømmen, 2010; Trein and Shirato, 2011). Table 3.2 shows how ADs may relate to unstable behaviour.

Table 3.2: Influence of ADs on unstable behaviour

Motion induced instability	Condition for instability to occur
Static divergence	$A_3^* > 0$
Galloping	$H_1^* > 0$
Torsional flutter	$A_2^* > 0$
Coupled flutter	$H_1^* > 0$, $A_2^* > 0$, A_1^*x$H_3^* > 0$,$\lvert H_2^*\rvert > 0$, $\lvert H_3^*\rvert > 0$, $\lvert A_1^*\rvert > 0$, $\lvert A_3^*\rvert >> 0$, $\lvert A_4^*\rvert > 0$

Analytical expressions for ADs have been established considering simple cases. For other cases, experimental determination of ADs is required (Tamura and Kareem, 2013). ADs may be identified by wind tunnel tests of section models applying free or forced vibrations. The free vibration tests give more realistic in-wind behaviour, while the forced vibrations tests provide less scatter (Siedziako and Øiseth, 2017a). Through forced vibration tests, ADs can be identified in the frequency or time domain. The frequency-domain methods are simpler. However, spectral leakage effects due to frequency domain truncation may be present. Spectral leakage can reduce the accuracy of estimation significantly as it causes a redistribution of energy within the spectrum. The more complex algorithm of a time-domain approach may therefore be preferable (Siedziako et al., 2017). As suggested by Han et al. (2014), the time domain method where the model is fitted to the recorded time series of self-excited forces by least squares is applied. The self-excited forces can be obtained from forced vibration tests by subtracting the static forces, buffeting forces and inertia forces from the measured total forces (Siedziako et al., 2017). In compact form, the self-excited forces in Equations 3.21 are expressed as

$$\boldsymbol{q^{SE}} = \boldsymbol{XE} \tag{3.22}$$

where

$$\boldsymbol{q^{SE}} = \begin{bmatrix} q^{SE}_{y,1} & q^{SE}_{z,1} & q^{SE}_{\theta,1} \\ q^{SE}_{y,2} & q^{SE}_{z,2} & q^{SE}_{\theta,2} \\ \vdots & \vdots & \vdots \\ q^{SE}_{y,n} & q^{SE}_{z,n} & q^{SE}_{\theta,n} \end{bmatrix} \qquad \boldsymbol{X} = \begin{bmatrix} \dot{r}_{y,1} & \dot{r}_{z,1} & \dot{r}_{\theta,1} & r_{y,1} & r_{z,1} & r_{\theta,1} \\ \dot{r}_{y,2} & \dot{r}_{z,2} & \dot{r}_{\theta,2} & r_{y,2} & r_{z,2} & r_{\theta,2} \\ \vdots & \vdots & \vdots & \vdots & \vdots & \vdots \\ \dot{r}_{y,n} & \dot{r}_{z,n} & \dot{r}_{\theta,n} & r_{y,n} & r_{z,n} & r_{\theta,n} \end{bmatrix}$$

$$\boldsymbol{E} = \frac{1}{2}\rho V^2 B \begin{bmatrix} K_y P_1^*/V & K_y H_5^*/V & BK_y A_5^*/V \\ K_z P_5^*/V & K_z H_1^*/V & BK_z A_1^*/V \\ BK_\theta P_2^*/V & BK_\theta H_2^*/V & B^2 K_\theta A_2^*/V \\ K_y^2 P_4^*/B & K_y^2 H_6^*/B & K_y^2 A_6^* \\ K_z^2 P_6^*/B & K_z^2 H_4^*/B & K_z^2 A_4^* \\ K_\theta^2 P_3^* & K_\theta^2 H_3^* & BK_\theta^2 A_4^* \end{bmatrix}$$

for n sample numbers in the time series. $\boldsymbol{X}$ is the motion history matrix and $\boldsymbol{E}$ is the equivalent coefficient matrix containing the ADs. By minimizing the sum of squares the equivalent coefficient matrix is estimated as follows:

$$\boldsymbol{E} = (\boldsymbol{X^T X})^{-1} \boldsymbol{X^T q^{SE}} \tag{3.23}$$

3.5 Flutter Analysis

Before the computer age, the common methods for determining the stability limit was the bimodal approach and Selberg's formula (Chen et al., 2001). To ensure a wind-resistant design of long-span suspension bridges with low natural frequency, examination of coupled flutter at a higher reduced velocity range was required. Higher-order modes were found to contribute significantly, resulting in the development of multi-mode flutter analysis procedure (Jain et al., 1996). In the frequency domain, multi-mode analysis determines the stability limit by finding a solution to the complex eigenvalue problem. Equation 3.3 reduces to the complex eigenvalue problem by setting $\boldsymbol{\eta}(\mathrm{t}) = \boldsymbol{\eta}_0 \mathrm{e}^{\lambda \mathrm{t}}$ and neglecting the turbulence-induced buffeting force and the aerodynamic mass effect

$$\left(\lambda^2 \tilde{\boldsymbol{M}}_0 + \lambda \tilde{\boldsymbol{C}}_0 + \tilde{\boldsymbol{K}}_0\right) \boldsymbol{\eta}_0 e^{\lambda t} = \frac{1}{2}\rho V^2 \left(\tilde{\boldsymbol{K}}_{ae} + \frac{\lambda b}{V} \tilde{\boldsymbol{C}}_{ae}\right) \boldsymbol{\eta}_0 e^{\lambda t} \tag{3.24}$$

which results in complex eigenvalues of

$$\lambda_j = -\zeta_j \omega_j + i\omega_j \sqrt{1 - \zeta_j^2}; \qquad (j = 1, ..., N_{mod}) \tag{3.25}$$

To obtain a solution to the complex eigenvalue problem, iterations are required as the aerodynamic modal stiffness matrix ($\tilde{\boldsymbol{K}}_{ae}$) and aerodynamic modal damping matrix ($\tilde{\boldsymbol{C}}_{ae}$) depend on the mean wind velocity and frequency. The flutter onset is triggered by unstable behaviour due to negative damping. When the real part of Equation 3.25 equals zero in one of the in-wind modes, the damping ratio becomes zero which identifies the stability limit (V_{cr}) (Chen, 2007). The following pseudocode describes the multi-mode flutter analysis process.

```
INPUT Modal properties: $\boldsymbol{\phi}, \tilde{\boldsymbol{M}}_0, \omega_j$
      ADs: $P_1^* - P_6^*$, $H_1^* - H_6^*$, $A_1^* - A_6^*$
SET initial in-wind velocity: $V_k = V_0$
    initial wind velocity increment: $\Delta V$
WHILE in-wind velocity is less than critical wind velocity: $V_k < V_{cr}$
  FOR mode j in $N_{mod}$ modes
    ESTABLISH aerodynamic modal stiffness and damping matrices: $\tilde{\boldsymbol{K}}_{ae_j}$, $\tilde{\boldsymbol{C}}_{ae_j}$
    SOLVE complex eigenvalue problem (Equation 3.24)
  END
  IF real part of resulting eigenvalue matrix is less than zero: $Re(\boldsymbol{\lambda}) < 0$
    INCREASE in-wind velocity: $V_{k+1} = V_k + \Delta V$
  ELSE
    HALF wind velocity increment: $\Delta V = \frac{\Delta V}{2}$
    DECREASE in-wind velocity: $V_{k+1} = V_k - \Delta V$
    IF wind velocity increment is less than 0.1ms$^{-1}$: $\Delta V < 0.1$
      EQUATE critical wind velocity to in-wind velocity: $V_{cr} = V_k$
    END
  END
END
```

Chapter 4

Cable Supported Bridges

The collapse of the Tacoma Narrows Bridge in 1940 marks a turning point in the evolution of cable-supported bridges. Today, it is a common perception that the failure of the bridge was due to torsional flutter. The two main factors responsible for the collapse was nearly no torsional rigidity and the aerodynamic unstable design of the bridge deck (Fujino and Siringoringo, 2013). After the Tacoma Narrows Bridge collapse, the focus of the prominent designers of the period shifted from considering only static wind pressure to the phenomena of aerodynamic stability. This chapter introduces existing concepts and vibration control measures of cable-supported bridges.

4.1 Presentation of Multi-Box Girders

The multi-box girders of one cable-stayed bridge (Stonecutters Bridge) and four suspension bridges (Yi Sun-Sin Bridge, Xihoumen Bridge, 1915Çanakkale Bridge and Messina Bridge) are studied in this section. Table 4.1 presents the cable-supported bridges arranged by increasing main span. The outlines are mainly obtained from Brancaleoni (2016) and show the shape of the deck including the countermeasures of guide vanes and spoilers. Other attachments such as railings, wind screens and maintenance rails are omitted. Key information about the construction period, main span, gap to depth ratio and slenderness are collected in Table 4.1. A tendency is evident for the suspension bridges of increasing gap to depth ratio with increasing main span.

Based on the experience gained from instability problems of the traditional single-box girders, it was found that the span of the Xihoumen Bridge could not achieve the stability requirement of 78.7 ms^{-1} with one girder only (Gimsing and Georgakis, 2012). To counteract flutter, the Xihoumen Bridge adopted the twin-box girder and initiated a trend for the proceeding design of suspension bridges. A critical wind speed of 88 ms^{-1} was estimated for the twin-box configuration of the Xihoumen Bridge. However, for the Stonecutters Bridge, the gap between the box girders was implemented due to the space required for the pylon shaft to pass between. The twin-box girder design is not justified by aerodynamic stability as a single-box girder could have satisfied the critical flutter velocity (Gimsing and Georgakis, 2012). The wind-induced problem encountered by the Stonecutters Bridge was VIV. Guide vanes were mounted at the knuckle lines of the bottom girder plates to diminish vortex formation (Larsen et al., 2008).

Table 4.1: Multi-box girders

Stonecutters			
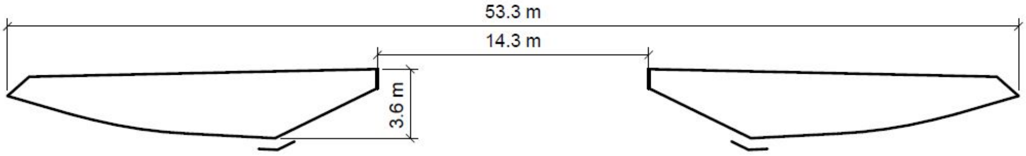			
Construction period:	2004-2009	Gap/depth:	3.97
Main span:	1018 m	Slenderness:	0.0035
Yi Sun-Sin			
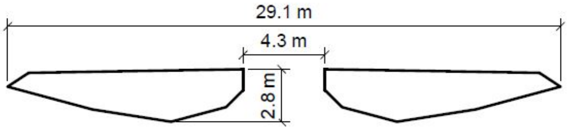			
Construction period:	2007-2012	Gap/depth:	1.54
Main span:	1545 m	Slenderness:	0.0018
Xihoumen			
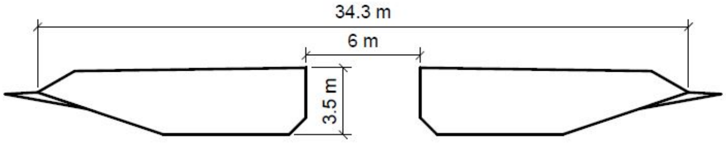			
Construction period:	2005-2007	Gap/depth:	1.71
Main span:	1650 m	Slenderness:	0.0021
1915Çanakkale			
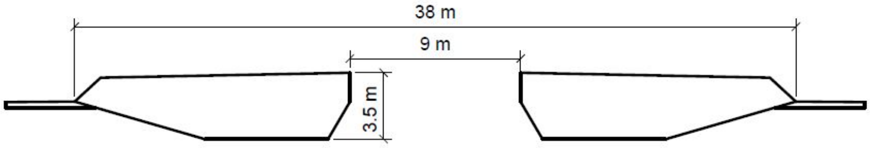			
Construction period:	2017-	Gap/depth:	2.57
Main span:	2023 m	Slenderness:	0.0017
Messina			
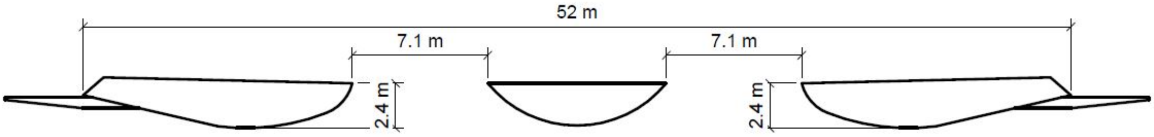			
Construction period:	-	Gap/depth:	2.96
Main span:	3300 m	Slenderness:	0.0007

The crossing of the Messina Straits is currently the longest span suspension bridge investigated. To address the issue of aerodynamic stability, the deck design is composed of three separated and streamlined box girders (Gimsing and Georgakis, 2012). The 1915Çanakkale Bridge is under construction about to become the largest suspension bridge in the world at the time of completion (Generate Directorate of Highways, 2020).

4.2 Countermeasures

Engineering solutions to reduce the undesirable vibration effect of long-span bridges have been adopted as countermeasures. Various vibration control measures are introduced to prevent the occurrence of different instability phenomena. However, absent are clear guidelines for engineers to select suitable countermeasures for long-span suspension bridges (Zhou et al., 2019). The relevant countermeasures of the thesis are presented and limited to the central slot concept and the installation of guide vanes and dampers.

4.2.1 Gap

The introduction of a gap reduces the pressure difference between the upper and lower girder surfaces and improves the flutter stability (Fujino and Siringoringo, 2013). The VIV performance of a twin-box girder is inferior to a single-box girder (Yang et al., 2016; Álvarez et al., 2018). At a critical gap to depth ratio, the flow surrounding the gap alters as seen in Figure 4.1. Small gaps prevent the formation of vortices behind the upstream girder and vortices are alternately shed behind the downstream girder. Whereas for moderate gaps, the flow detaches at the leeward side of the upstream girder and vortices emerge in the gap interfering with the downstream girder. For large gaps, a vortex street is created behind both girders without mutual interference. From wind tunnel testing, Laima and Li (2015) and Kwok et al. (2012) has identified a critical gap to depth ratio of approximately 2.14. However, the effectiveness of the flutter performance is strongly dependent on the girder design and the composition of attachments (Yang et al., 2015).

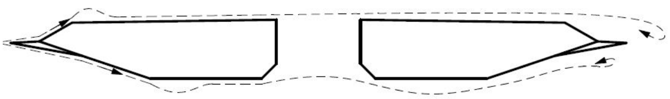

(a) Small gap

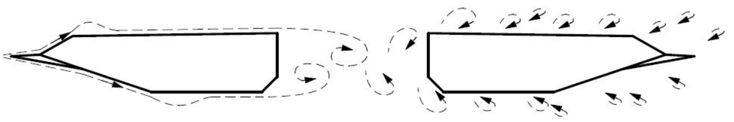

(b) Moderate gap

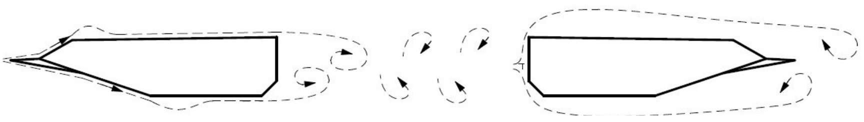

(c) Large gap

Figure 4.1: Expected flow regime of various gaps

4.2.2 Guide Vanes

Installing guide vanes beneath the girder of the Stonecutters Bridge is an efficient countermeasure for migrating the response due to vortex shedding (Larsen et al., 2008). By smoothing the air flow around the corners of the upstream girder section, the guide vanes prevent the formation of vortices at the flow separation point. Consequently, the vortex shedding street of the upstream girder no longer influences the downstream girder. Figure 4.2 illustrates the expected flow regime for a twin-box girder without and with guide vanes. Through a series of wind tunnel tests, Yang et al. (2016) explored the VIV performance of guide vanes of twin-box girders, revealing a dependency of effectiveness on the position and geometry of the guide vane along with the gap to width ratio of the deck.

After the completion of the Great Belt Bridge, vortex wind-induced problems were discovered. Aiming to suppress the VIV of the single-box girder, guide vanes were installed (Fujino and Siringoringo, 2013). The proceeding investigations by Frandsen (2004) found a reduction in critical flutter wind velocity of the suspension bridge due to the addition of guide vanes. However, an increase in critical flutter wind velocity was found with the installation guide vanes on twin-box girders (Zhou et al., 2019). The external guide vanes exhibiting superior flutter performance compared to the internal guide vanes.

(a) without guide vanes

(b) With guide vanes

Figure 4.2: Expected flow regime without and with guide vanes

4.2.3 Tuned Mass Dampers

The tuned mass damper (TMD) exploits the physics of an oscillator; a system that when displaced from its equilibrium position experiences a restoring force. The structural damping in the cables of suspension bridges is very low and dampers are often installed to mechanically control the vibrations (Gimsing and Georgakis, 2012). The Millennium Bridge is a prime example. The lateral suspension bridge serves as a pedestrian crossing of the River Thames in London. At the opening of the bridge into the new millennium, unpleasant swaying was experienced. The crossing crowd of walking people falling into step created a frequency that matched the natural frequency of the bridge. To counteract the bridge vibrations, dampers were installed. The frequency associated with the damper is tuned to the resonant frequency of the bridge. When the bridge is excited at the tuned frequency, the damper moves out of phase with the bridge. By absorbing the kinetic energy from the bridge, the TMD reduces the amplitude of vibration and increases the damping ratio.

Chapter 5

Girder Configurations and Design

The aim of this thesis is to derive at a twin-box section with sufficient aerodynamic stability for the super-long span. The first step is to determine an initial selection of cross-sections whose geometry is optimized based on prior knowledge of the bridge deck aerodynamics. According to Fujino and Siringoringo (2013) a low width to depth ratio diminishes the susceptibility of coupled and torsional flutter. Also mentioned, is the increased flutter stability by streamlining the decks and the adoption of fairings. Effectiveness of the gap is depends on the gap to width ratio of the configurations as well as the cross-sectional design (Laima and Li, 2015). Further reading provides insights to the possible effects of each chosen attribute.

By combining three designs with three different gap widths, a potential to distinguish between the behaviour of the design attributes from the gap width effects is enabled. The three different cross-sectional designs are given the names S1, S2 and S3 and can be seen in Figure 5.1.

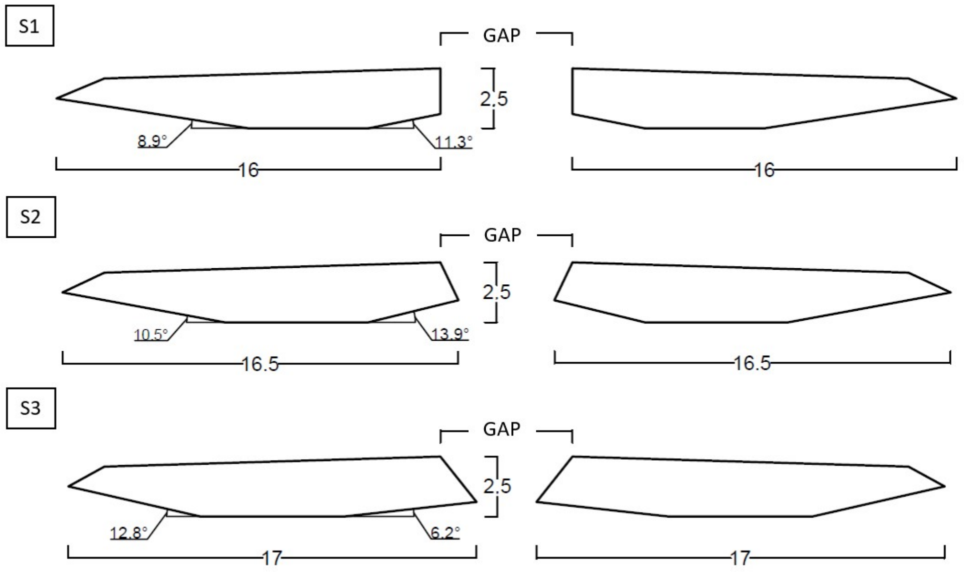

Figure 5.1: The three chosen cross-sectional designs of the twin-decks, with length units in [m] and 1:1 scale

The geometry of S2 is obtained by interpolation of the coordinates of S1 and S3 in Matlab. Through interpolation, a geometric relation is obtained between S1, S2 and S3 which is beneficial when observing the influence of the geometric variations. For all three girder cross-sections, the non-varying geometric properties are the girder depths and the roadway, with values of 2.5 m and 14 m respectively. The change in total widths of S1, S2 and S3 are caused by the varying angles of the inner and outer girder tip. Figures of the cross-sections with detailed dimensions are presented in Appendix B.

Multiconsult proposed an asymmetrical streamlined twin-box girder design for the suspension bridge crossing the Sulafjord in 2015 (Multiconsult, 2015). Wind tunnel tests showed good results for galloping and torsional instabilities but were on the other hand too vulnerable for both flutter and static divergence (Grongstad and Kildal, 2018). Neither the Multiconsult design nor a symmetrical less streamlined version of the design studied in Giske and Midtgarden (2018), met the critical flutter wind speed requirements of the bridge crossing of the Sulafjord.

A significant alteration in the girder designs of this thesis from the previously tested cross-sections is the narrow depth with respect to width. When addressing the flutter issue, less separation of the wind flow at the tip can mitigate the formation of vortexes along the girder surface. By the employment of fairings at the outer parts of the cross sections the flutter stability can be improved (Fujino and Siringoringo, 2013). The fairing angle is the horizontal angle of the inclined web. The cross-sections all have fairing angles below 15 degrees, which has proven to be beneficial for the aerodynamic stability (Wang et al., 2011).

The *gap* is defined as the horizontal distance between the inner uppermost points of the girders circumference. For this thesis, all three cross-sections will be tested with gaps of 5.5, 10.5 and 15.5 m, labelled G1, G2 and G3, respectively. By studying the existing long-span suspension bridges with twin-box girders, presented in Table 4.1, noticeable is a trend of an increasing gap to depth ratio with increasing main span for the suspension bridges. The gap to depth ratio for this thesis can be seen in Table 5.1 and are all above the critical ratio at approximately 2.14 (Laima and Li, 2015). Testing with different gap to depth ratios is favourable to observe both if the behaviour of the Strouhal number will be as expected as well as the effect the different gaps has on the flutter stability.

Gap	Gap width [m]	Gap to depth ratio
G1	5.5	2.2
G2	10.5	4.2
G3	15.5	6.2

Table 5.1: Chosen gaps and the corresponding gap to depth ratio.

Chapter 6

Global Element Models

Global element models of the suspension bridge crossing the Sulafjord are used to extract the modal parameters required to calculate the aerodynamic stability limits. The feasibility study of the Sulafjord crossing by Multiconsult is used as a reference for the bridge design (Multiconsult, 2015). Figure 6.1 shows the finite element (FE) model of the suspension bridge crossing the Sulafjord.

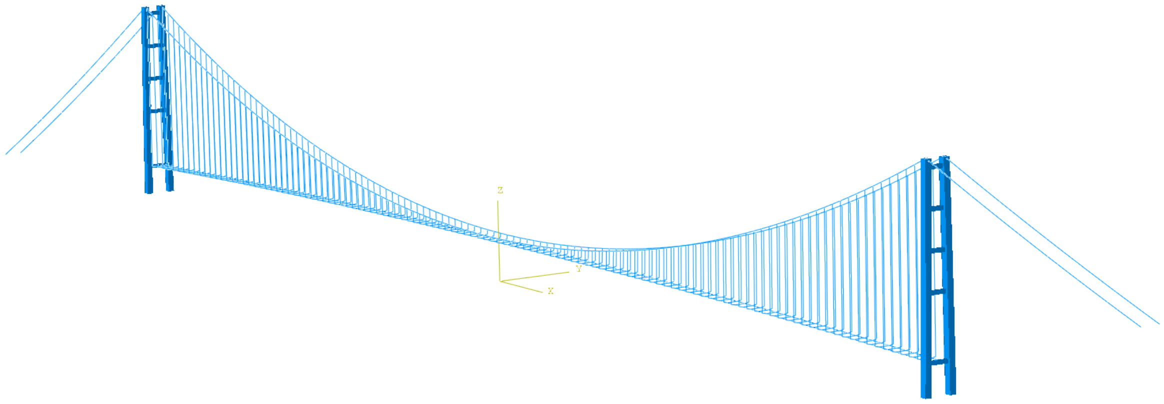

Figure 6.1: FE model of the Sulafjord Bridge

For each of the nine girder configurations, a FE model in Abaqus/CAE is created with assistance from Postdoc. Øyvind Wiig Petersen by writing the input file using Python commands (Dassault Systèmes Simulia Corp., 2014). The script *Sulafjorden_TD21_S1G1.py* used to model S1-G1 is provided in the electronic attachments (Appendix A). Abaqus scripting is the preferred approach for parametric modelling due to the efficiency of parameter modification and simplicity of implementing new commands. The script is a development of the work presented by Dombu and Gjelstad (2019), which models the Langenuen Bridge. The existing script remains unchanged except for the following modifications:

- A second girder is introduced to obtain a twin-box girder.
- The pylon type is changed from 'A'-shaped to 'H'-shaped pylons and multiple portal beams are added.

- A function that searches for nearby points is implemented to ease the creation of connection elements and ties with changing input variables.
- The geometric variables and section properties of the model parts are modified to fit the bridge design of the Sulafjord crossing.

6.1 Modelling Principles

The workflow in Abaqus is illustrated in Figure 6.2. The green boxes are input parameters, the grey boxes represent the process and the red box is the desired output. The script *AbaqusExportModal.py* is provided by Postdoc. Øyvind Wiig Petersen to extract the modal properties from the .odb-files containing the results from the Abaqus simulations. The modal parameters are further used in the computation of the aerodynamic stability limits.

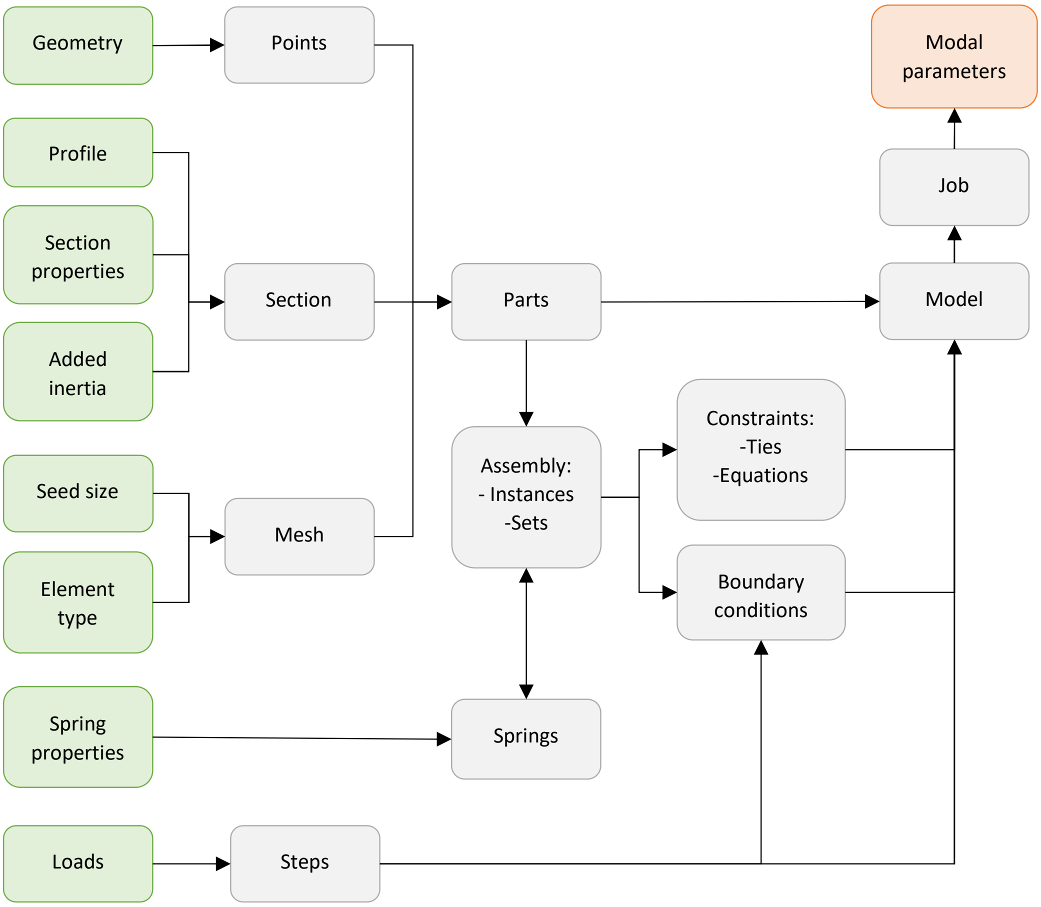

Figure 6.2: Flowchart illustrating the workflow in Abaqus

The Abaqus model is assembled similar to the construction stages of a suspension bridge. To provide an illustation, Figure 6.3 demonstrates the construction of the Hardanger Bridge, which replicate the static steps created in Abaqus. The pylons are withdrawn using retraction cables to obtain a natural vertical position of the pylons when loaded by the self-weight of the bridge. For simplicity, the force of the retraction cables at the tower tops are omitted, resulting in an inward lean of the towers at the final construction stage (Step 3). This is a valid assumption as inward leaning towers will have minor impact on the flutter analyses. An iteration procedure is executed in Abaqus to account for the displacement due to self-weight with a margin of less than 0.1 m. The adjusted input parameters are the main span sag of the cables and the vertical curvature of the girders.

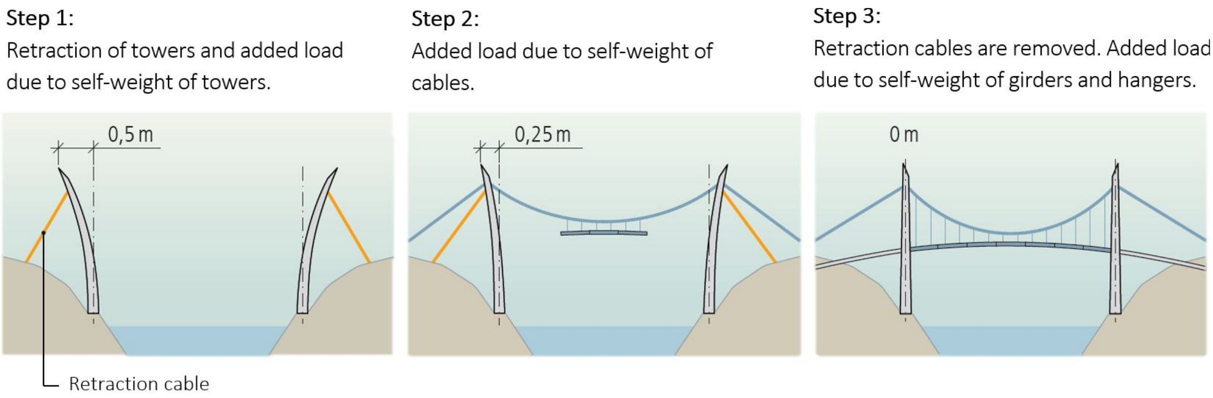

Figure 6.3: Construction of the Hardanger Bridge (Illustration: Statens vegvesen (2011))

6.2 Geometry

Figure 6.4 presents the definitions of the input parameters in Abaqus and the geometry at the final construction stage. The beams representing the girders are positioned in the mass centre of the girders. The parameter p defines the horizontal distance between the girders, which is unique for each configuration (Table 6.1).

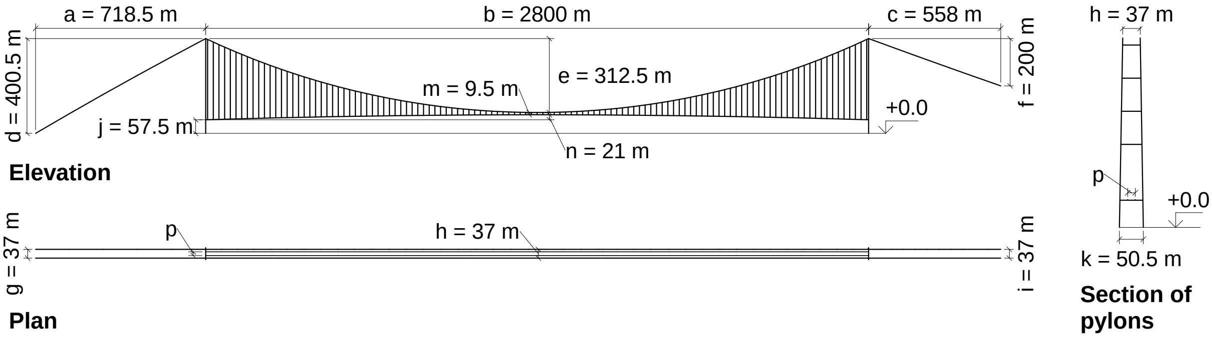

Figure 6.4: Input parameters

Table 6.1: Values of the parameter p

	p [m]		
Config.	G1	G2	G3
S1	15.032	20.032	25.032
S2	15.838	20.838	25.838
S3	16.310	21.310	26.310

6.3 Section Properties

The section properties of the cables, hangers, pylons and portal beams are tabulated in Table 6.2. Modal properties are not sensitive to pylon stiffness. Therefore, the pylons are assigned box profiles with simplified constant cross-section and thickness. Figure 6.5 illustrates the conservatively selected dimensions for the pylons and the portal beams.

Table 6.2: Section properties

Component	Material	E	ρ	A	$I_{11} = I_{22}$	J
		$[GPa]$	$[kgm^{-3}]$	$[m^2]$	$[m^4]$	$[m^4]$
Cables	Steel	200	7850.0	6.3110×10^{-1}	3.170×10^{-2}	6.340×10^{-2}
Hangers	Steel	155	7850.0	6.3330×10^{-3}	3.192×10^{-6}	6.384×10^{-6}
Pylons	Concrete	37	2500.0			
Portal beams	Concrete	37	2500.0			

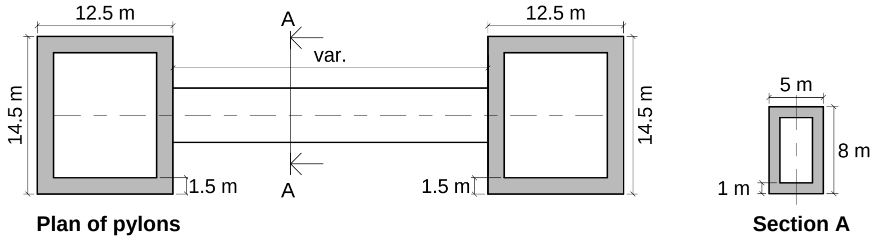

Figure 6.5: Profiles of pylons and portal beams

6.4 Added Girder Inertia

In Abaqus, the bridge deck girder is modelled using line-like elements without height and width dimensions. Hence, geometric shape variations are accounted for by introducing added girder inertia, linear mass and eccentricities for each girder cross-section. The modelled beam elements are placed in the shear centre of each cross-section thereby obtaining zero eccentricities for girders and diaphragms. Calculated values for configuration S1-G1 is presented in Table 6.3 and identical tables for all 9 configurations can be found in Appendix C.

Table 6.3: Added girder inertia for S1-G1

Component	Linear mass	e_1	e_2	I_{11}	I_{22}
	$[kg/m]$	$[m]$	$[m]$	$[kgm^2/m]$	$[kgm^2/m]$
Girder	6045.550	0	0	5542.885	143309.600
Diaphgrama	562.119	0	0	201.824	9034.565
Asphalt	2800.000	2.234	1.287	1.493	45733.333
Hanger heads	33.333	9.234	1.047	0.025	0.025
Cross-beams	191.125	-6.141	0	240.794	120.449

Neither stress analysis nor buckling of the cross-sectional plates is performed in this thesis as the focus is set on aerodynamic performance of twin-deck bridge girders with varying geometric shapes and gaps. Capacity calculations were performed for a twin-deck solution for the Sulafjord bridge crossing by Multiconsult (Multiconsult, 2015). To ensure reasonable values the plate and asphalt thickness, as well as stiffener geometry and dimensions are adopted from their feasibility study.

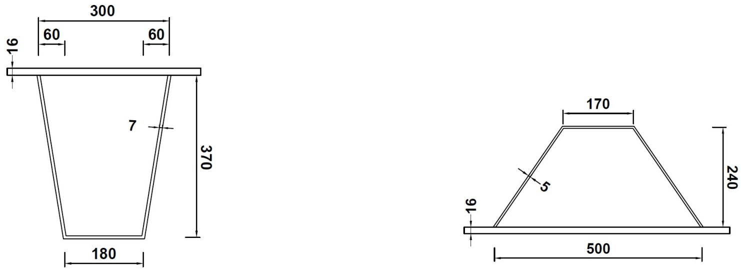

(a) Type 1: For top plate (b) Type 2: For remaining plates

Figure 6.6: Geometry and dimensions of stiffeners

The inertia forces I_{11} and I_{22}, around the local y-axis and z-axis of the girders respectively, are calculated using the computational program CrossX for thin-walled cross-sections. A simplified version of the cross-section with only the main outer plates and an effective wall thickness (t_{eff}) is used. The effective thickness is derived by dividing the total steel area of the cross-section, plates and stiffeners, by its circumference. The main aim by introducing stiffeners is therefore to derive reasonable values for cross-sectional linear weight and total steel area for the calculations.

The placement and number of the longitudinal stiffeners in Figure 6.7(b) is only based on, not identical to, a detail drawing from Multiconsult. Minimal variations in the circumferences of S1, S2 and S3 gave a similar amount of stiffeners and steel area, resulting in a mean value of $t_{eff} = 22.5mm$ for all cross-sections. The dimensions and layout of the cross beams are based on the concept study of Rambøll (2015), due to the lack of detailed drawings in Multiconsult (2015). The dimensions of the cross-beam stiffeners are equivalent to stiffener of Type 1.

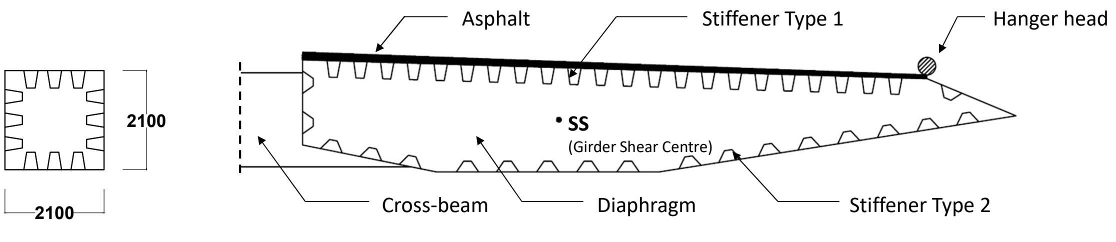

(a) Cross-beam (b) Right box girder with details and proposed stiffener layout

Figure 6.7: Cross-beam and right box girder of S1 with details

The only gap dependent parameters are the horizontal eccentricities and the length of the cross-beams. The shear centre of the cross-beam is vertically aligned with the girder shear centre, obtaining zero eccentricity. Cross-beams and hanger heads are added to the girder every 4 m, at the same span-wise position. Diaphragms of 10 mm thickness are spaced with 24 m intervals along each girder. The total linear mass of each deck configuration is tabulated in Appendix D.

Chapter 7

Wind Tunnel Tests

7.1 Section Models

Wind tunnel testing is a crucial part of determining the aerodynamic stability of a proposed cross-sectional design for a super long-span suspension bridge. A section model is a down-scaled replica of a section of the bridge deck girders. The width of the wind tunnel introduces a length limit to the section models. To ensure sufficiently slenderness for all gap widths, the section models are built in a 1:50 scale with a length of 2.64 m. This chapter addresses the different components and explains the building process.

7.1.1 Girders

The section models are made out of a PVC-based material called Divinycell, which is a light compact material that can imitate the low mass of a slender bridge girder and is easy to mill into different shapes. Due to the low strength and stiffness of Divinycell, an aluminium pipe is used as reinforcement in the longitudinal direction. The pipe also serves as a connection to the load cells in the wind tunnel. The girders are assembled as sandwich elements with Divinycell-blocks on each side of the aluminium pipe. Prior to mounting, three half-circle shaped paths are milled into each Divinycell-block. One path for the aluminium pipe, and two paths with the diameter of the wooden handle of the TMDs. One of the smaller paths is milled out to even out the weight loss of the TMD path. The model parts are glued together with "Casco Superfix Mounting Glue" spread out with spatulas and left to dry with applied pressure, see Figure 7.1(a).

For milling, a CNC-router of the model LTS-1530-4A provided by the Structural Engineering Department at NTNU as seen in Figure 7.1(b), is used. The router makes it possible to mill an entire section all at once, resulting in only 6 milling jobs, one for each girder. By following a three-axis system, the router uses coordinates obtained from a Matlab script for each girder section to orient itself during milling. Placing of the model and choice of local origo before milling is crucial to the accuracy of the finished results. A vacuum system restrains the finished sandwich elements of the girders during the milling. Due to the high precision of the router, the position of the models has to be completely parallel to the longitudinal axis of the CNC-router system before restraining them. Only one side is milled at a time, the milling procedure is repeated for the bottom face of the model.

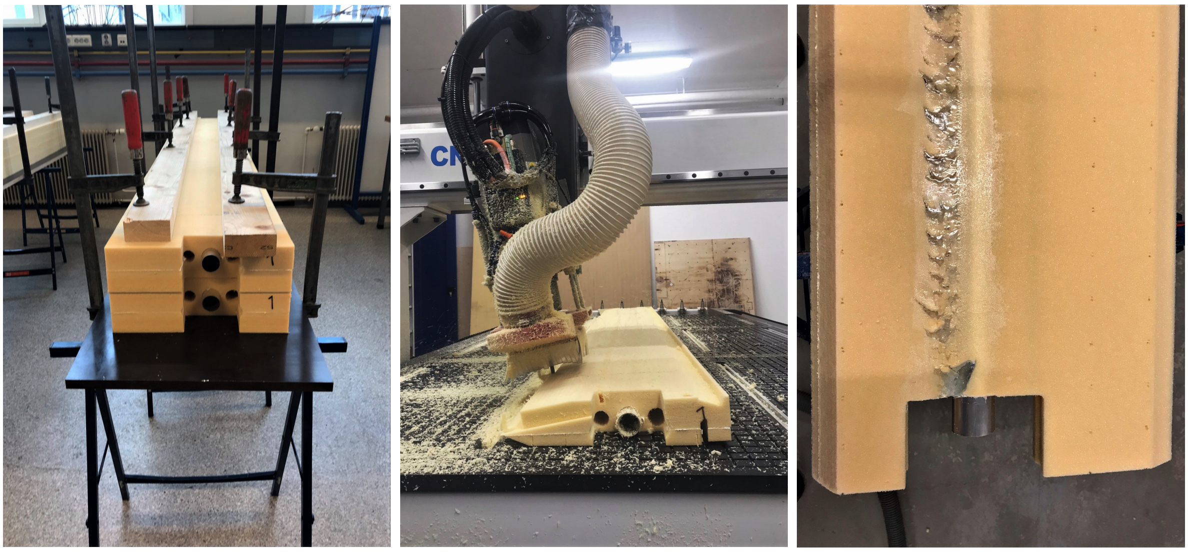

(a) Glued sandwich elements (b) Milling with CNC-router (c) Damaged S3 fixed with sealant

Figure 7.1: Pictures from building process

The steep inner angle of S3 caused the suction cap of the drill to rip the model. A transparent sealant of the type "Casco Clearseal" was applied to smooth out the severe damages, see Figure 7.1(c). The required amount of sealant resulted in a slight increase in the self-weight for the upwind girder of S3. Smaller cracks and misplaced holes are also sealed off with the sealant to guarantee a smooth surface as possible. In addition, although the milling is highly precise, all section models have been sanded with fine sandpaper for the removal of dust and smaller inaccuracies.

7.1.2 Built-in Tuned Mass Dampers

In the previous attempt on the stability limit for the bridge crossing the Sulafjord made by (Grongstad and Kildal, 2018), a self-made TMD proved to be favourable. To enhance the chances of improved stability of the girder, a built-in TMD is included in each section model. The design of the TMDs is proposed by Ole Øiseth as an upgraded version of the TMDs used in (Grongstad and Kildal, 2018). It is composed of a wooden handle and a wooden skewer with 20 coins at the tip, assembled as shown in Figure 7.2. The skewer and coins make up for a cantilever with a lumped mass of approximately 87 g. The wooden handle is glued and clamped inside the section models, while the coins are glued to the skewer which can be pulled to the desired length. As a result, the cantilevered mass can move freely when the section models start vibrating. A rough estimate showed a frequency of 8 Hz for a TMD with a cantilever length of 11 cm. The frequency of the section models are unknown prior to testing, so a slit for adjustment is cut out of the Divinycell material above the TMDs.

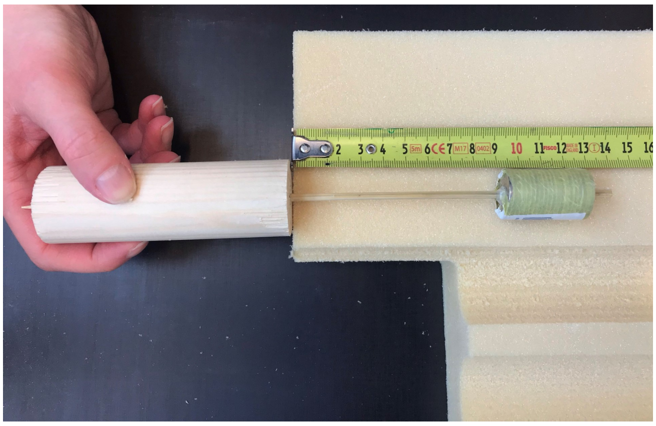

Figure 7.2: Self-constructed TMD illustrating a cantilever of 11 cm

7.1.3 Railings

Attachments are added to the bridge girder section models due to research by Siedziako and Øiseth (2017b) revealing a significant impact on the wind tunnel test results. Handrails and crash barriers can cause larger flow separation and decrease in the vortex shedding frequency, resulting in significant effects on the VIV (Laima et al., 2018). These attachments also serve as safety measures on a finished bridge and cannot be omitted.

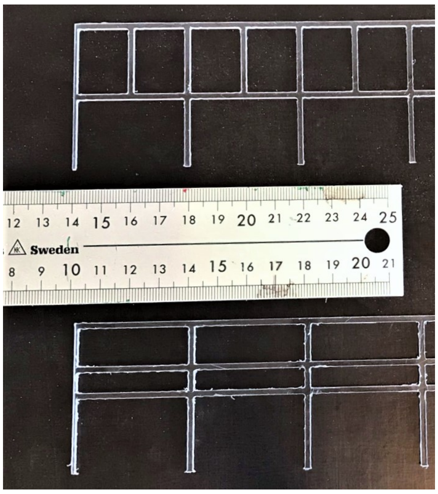

Figure 7.3: Picture of finished handrails (top) and crash barriers (bottom)

All section models are tested with railings, both handrails and crash barriers. One set of railings are used for all tests, hence the railings are transferred between the section models. The railings are milled out of a hard transparent plastic plate by the same CNC router as for the girders. Due to the vacuum system, the router cannot cut all the way through the plate and the railings have to be detached from the plate with a knife, consequently causing quite rough edges. To ensure that the railings do not interfere excessively with the wind flow during testing, the edges are scraped smooth with a knife. 3D printing could have shortened the production time of the railings significantly. Seen as the railings are to be transferred the material used for 3D printing is evaluated as too fragile and therefore excluded as an option.

7.1.4 Guide Vanes

To diminish VIV, guide vanes are attached to the bottom girder plates at the outer knuckle lines. The guide vanes are modelled with scaled-down dimensions of the guide vanes installed at the Great Belt Bridge (Larsen et al., 2000). Figure 7.4 shows the guide vanes created in Solidworks (Dassault Systèmes Simulia Corp., 2020). Protruding spikes are made to ease the attachment of the guide vanes to the bottom of the girder. The angle (α) obtains values of 171.12 °, 169.51 ° and 167.20 ° for S1, S2 and S3, respectively. The guide vanes are 3D-printed with the powder-based material PA2200 using the fused deposition modelling (FDM) device EOS P 395. Due to the limitations of the 3D printer, segments with a length of 291.5 mm are produced. PA2200 is a high-performance alternative to polylactic acid (PLA). However, because of the brittle material properties, minimum model thicknesses of 1 mm and 2 mm are selected for the plate and the installation spikes to avoid damage to the guide vanes.

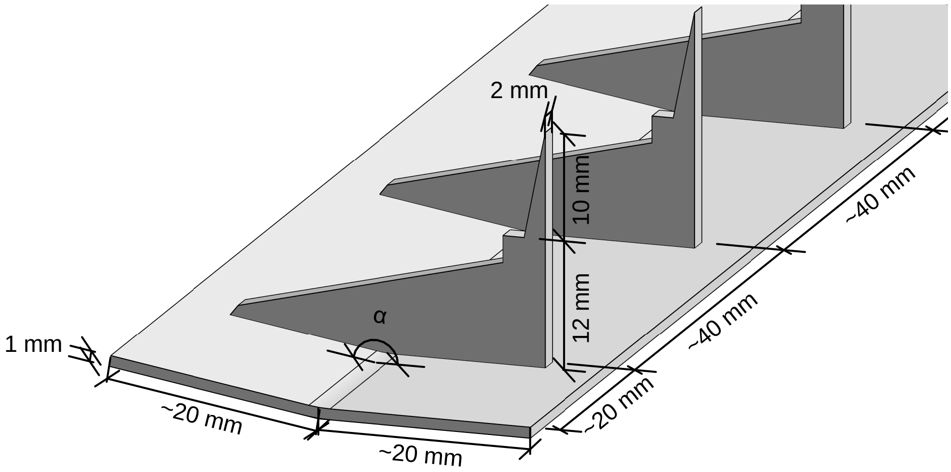

Figure 7.4: Model of guide vanes

7.2 Experimental Setup

The tests are conducted in the wind tunnel located in the Fluid Mechanics Laboratory at NTNU. The wind tunnel is a closed loop with a 2.7 m wide, 2.0 m high and 11 m long test arena. At the inlet, the wind profile is uniform and the flow is close to laminar (Siedziako et al., 2017). A pitot probe positioned halfway between the inlet and the rig computes the wind speed from air density variations with temperature. Figure 7.5 shows the experimental setup with the section models placed in the wind tunnel. Railings and guide vanes are attached to the girders. The actuators are mounted on the outer walls of the wind tunnel generating horizontal, vertical and rotational motion. At the ends of the section models, load cells are installed to measure the load. The gap is varied by moving the section models which are fastened to pre-drilled holes in the connection steel beam.

(a) Wind tunnel test arena

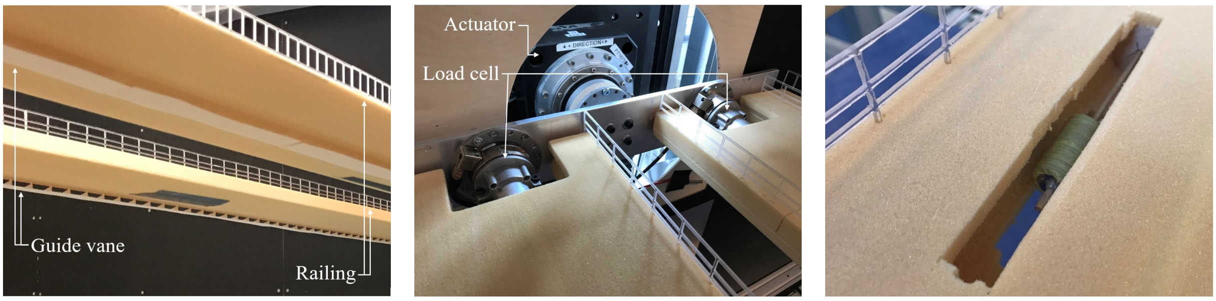

(b) Girder attachments (c) Forced vibration rig (d) Bult-in TMD

Figure 7.5: Section models installed in the wind tunnel

7.3 Testing Procedure

A series of wind tunnel tests are performed on the nine girder configurations. For the calculation of the critical wind speed, estimation of the mass and damping is required. The mass per unit length of the section models with attachments is recorded (Appendix D). The damping is determined from the decay of a free vibration time series initiated by a gentle stroke to the girder. The built-in TMDs in Figure 7.5(d) are manually tuned approximately to the natural frequency of the section model by sliding the rod altering the position of the coins relative to the wooden block. As TMDs are challenging to replicate in full-scale, it is desirable to achieve adequate damping and VIV performance without the influence of the TMD. Therefore, additional damping and VIV tests with a disabled TMD is conducted for S2-G3 by moving the coins to the cantilever support. In the wind tunnel, air density fluctuations of 1.18-1.19 kgm^{-3} are experienced. The air density of 1.2 kgm^{-3} is used as a conservative measure in the proceeding computations. With a sampling frequency of 200 Hz, the following wind tunnel tests are conducted.

7.3.1 VIV Tests

Vibrations due to vortex shedding are detected by performing a VIV test. While the section model is fixed in neutral position, the wind speed is gradually increased. With resonance, vibrations are observed when the natural frequency of the model coincides with the vortex shedding frequency. Vibrations due to vortex shedding disturbs the measured load. Therefore, the wind speeds causing VIVs are avoided in the proceeding quasi-static and forced vibration tests.

7.3.2 Quasi-Static Tests

To determine the static coefficients, quasi-static tests are performed. With a frequency of 0.008 Hz and an amplitude of 8 degrees, the section model is quasi-statically rotated such that the inertia forces can be neglected. In addition to a reference test in still-air, the procedure is repeated for wind speeds of 6, 8 and 10 ms^{-1} to reveal Reynolds number dependency of the static coefficients.

7.3.3 Forced Vibration Tests

Forced vibration tests are conducted to identify the eighteen ADs. The section models are forced into the single-harmonic motions listed, each providing the results associated with six ADs.

- Horizontal motion with amplitude of 20 mm
- Vertical motion with amplitude of 20 mm
- Torsional motion with amplitude of 1 degree

The frequencies 0.25, 0.5, 0.8, 1.1, 1.4, 1.7, 2.0 and 2.5 Hz are considered in the forced vibration tests. The reference still-air test is conducted to measure the inertia force and the in-wind tests with wind speeds of 6 and 8 ms^{-1} provide the data points in the ADs plots.

Chapter 8

Results, Analysis and Discussions

This chapter presents the processed data from the global element models and wind tunnel tests in addition to the predicted stability limits. The scripts *importAbaqusResults.m*, *VIV.m*, *staticCoeffAllTests.m*, *aerodynamicDerivativesAllTests.m* and *flutterAnalysis.m* are provided by Prof. Ole Øiseth to acquire the modal properties, results from the VIV tests, static coefficients, aerodynamic derivatives and predicted stability limits, respectively. The instability behaviour of the individual configurations are investigated and comparisons between the configurations are made. Lastly, the limitations of the results are presented.

8.1 Modal Properties

To estimate the stability limit, the modal properties are obtained from FE modal analysis. Appendix E provides the results for all FE-models processed using *modalProperties.m*. The first vertical mode is illustrated in Figure 8.1.

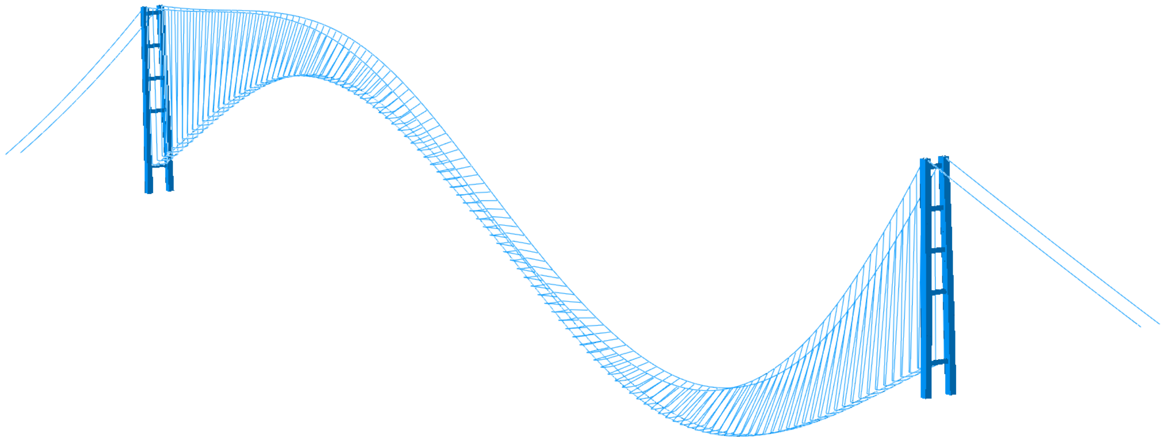

Figure 8.1: First vertical mode of FE-model

The modal properties for S1-G1 are presented in Table 8.1. The 50 first modes dominated by girder deflection is considered to evaluate the stability. The mode numbers, mode names, generalized masses and generalized stiffnesses are presented and arranged by increasing frequency. Alongside, the displacement plots for horizontal, vertical and torsional motion are displayed. The mode names are composed of the horizontal (H), vertical (V) and torsional (T) direction of motion followed by an accumulating index. Considering each direction of motion separately, the generalized stiffness increases with the frequency, while the generalized mass remains roughly constant.

Table 8.1: Modal properties for S1-G1

No.	Name	$\tilde{M}$	$\tilde{K}$	f	Displacement plot		
		[kg]	[Nm^{-1}]	[Hz]	Horizontal	Vertical	Torsional
1	H1	3.847×10^7	1.419×10^6	0.031	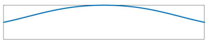	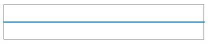	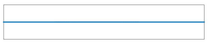
2	H2	3.054×10^7	5.014×10^6	0.064		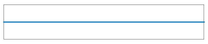	
3	V1	4.227×10^7	6.957×10^6	0.065			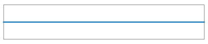
4	V2	2.189×10^7	5.212×10^6	0.078		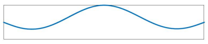	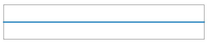
5	V3	3.298×10^7	1.626×10^7	0.112			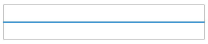
6	V4	3.794×10^7	1.951×10^7	0.114		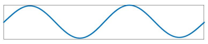	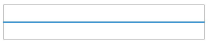
7	H3	2.583×10^7	1.419×10^7	0.118			
12	V5	3.496×10^7	2.954×10^7	0.146		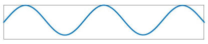	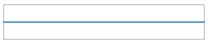
15	V6	4.123×10^7	4.915×10^7	0.174		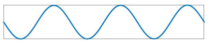	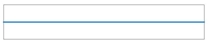
20	H4	3.897×10^7	6.462×10^7	0.205	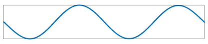		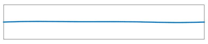
21	V7	3.782×10^7	6.278×10^7	0.205	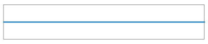	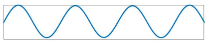	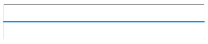
23	T1	2.760×10^7	5.678×10^7	0.228		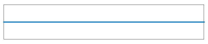	
24	V8	3.993×10^7	8.741×10^7	0.235		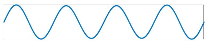	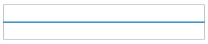
33	V9	3.585×10^7	1.023×10^8	0.269		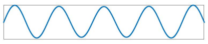	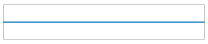
35	T2	2.388×10^7	7.705×10^7	0.286			
38	V10	3.502×10^7	1.264×10^8	0.302		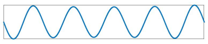	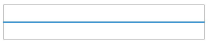
41	V11	3.348×10^7	1.508×10^8	0.338		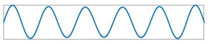	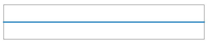
42	H5	2.740×10^7	1.243×10^8	0.339			
43	V12	3.342×10^7	1.852×10^8	0.375		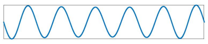	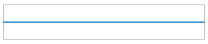
50	V13	3.223×10^7	2.179×10^8	0.414		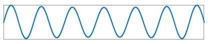	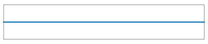

In Figures 8.2(a), 8.2(b) and 8.2(c) the natural frequencies are plotted against the gap for horizontal, vertical and torsional vibration modes, respectively. As the natural frequencies and mode shapes are similar for all sections, an average is taken of the section configurations. Where the darker shades of blue represent the higher-order modes. A 2nd order polynomial fit is implemented as a dashed line to observe modifications in natural frequency with changes in the gap. The listed changes in natural frequency are observed with alternations in the gap.

- For the horizontal modes, the natural frequency increases with the gap. With larger gaps, the generalized stiffness increases, which causes an increase in natural frequency. The increase in natural frequency due to the increased stiffness dominates the decrease in natural frequency due to the increased inertia. The increase in natural frequency is more prominent for the higher-order modes.

- For the vertical modes, a slight decrease in natural frequency with increasing gap is noticeable. With the increase in the gap, heavier cross-beams are obtained. Consequently, the inertia increases resulting in a small decrease in the natural frequency. The decrease in natural frequency is more clear for the higher-order modes.

- The torsional modes exhibit different trends. The first torsional mode is influenced by the increasing inertia causing a decrease in natural frequency for larger gaps. For the second torsional mode, the natural frequency increases for larger gaps. The stiffness-increasing effect dominates the mass-decreasing effect of the natural frequency.

Summarized, the sections have similar modal properties as expected due to the small amendments in the section shapes, while deviations in frequencies are observed for altering gaps.

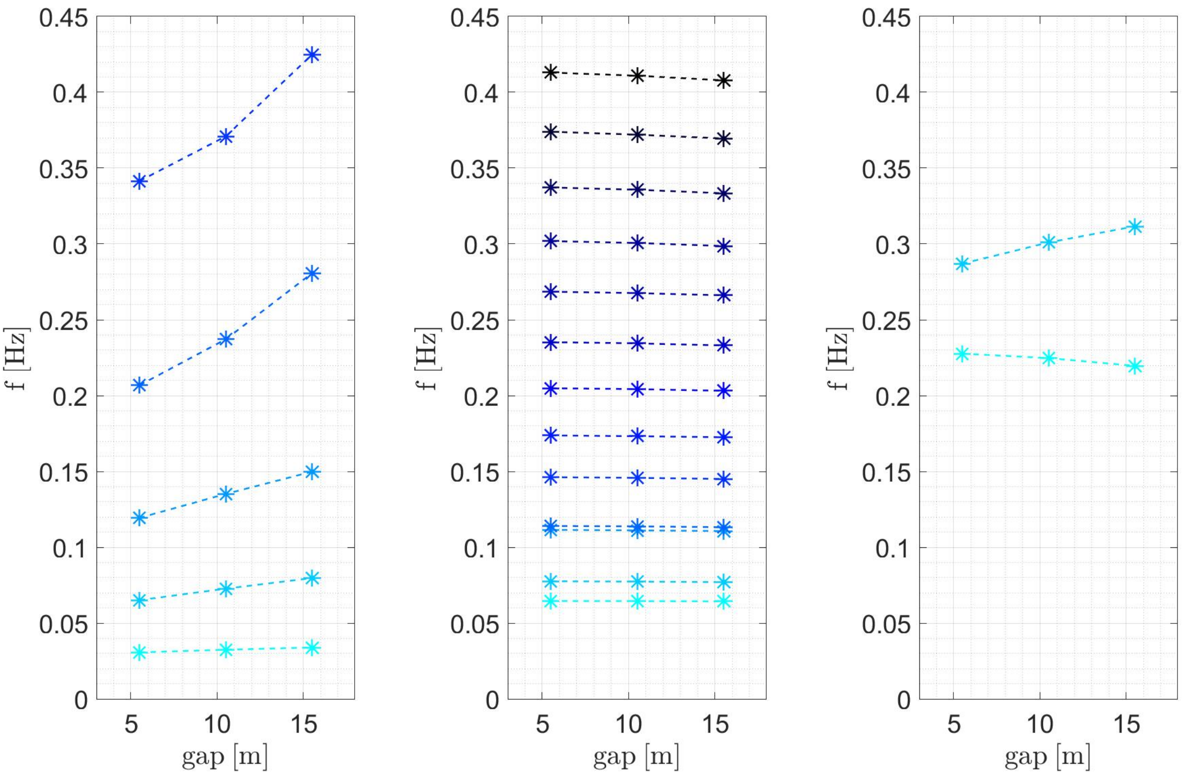

(a) Horizontal modes (b) Vertical modes (c) Torsional modes

Figure 8.2: Natural frequencies

8.2 Vortex-Induced Vibrations

In this section, the vortex-induced oscillating behaviour of the section models and full-scale bridge decks is considered. For the section models, the VIV tests and Strouhal numbers are investigated. While the damping and Scruton numbers are studied for both the section models and the full-scale bridge decks.

As TMDs are challenging to replicate in full-scale, it is desirable to achieve adequate VIV performance without the influence of the TMD. Figure 8.3(a) and 8.3(b) show the VIV test results for S2-G3 with active and disabled TMD, respectively. The VIV wind tunnel test results for all configurations are gathered in Appendix F. The sum of the recorded forces for the upstream girder and downstream girder are displayed for gradually increasing velocity. With resonance, vibrations are observed when the natural frequency of the section model coincides with the vortex shedding frequency. Identified for both the active and disabled TMD is a velocity causing VIV of $3.15\,\mathrm{ms^{-1}}$. The amplitudes of the forces are smaller for the section model with the active TMD compared to the section model with the disabled TMD. The plotted force-time series indicates that the built-in TMDs of the tested sections models affect the severity of the vortex-induced oscillations.

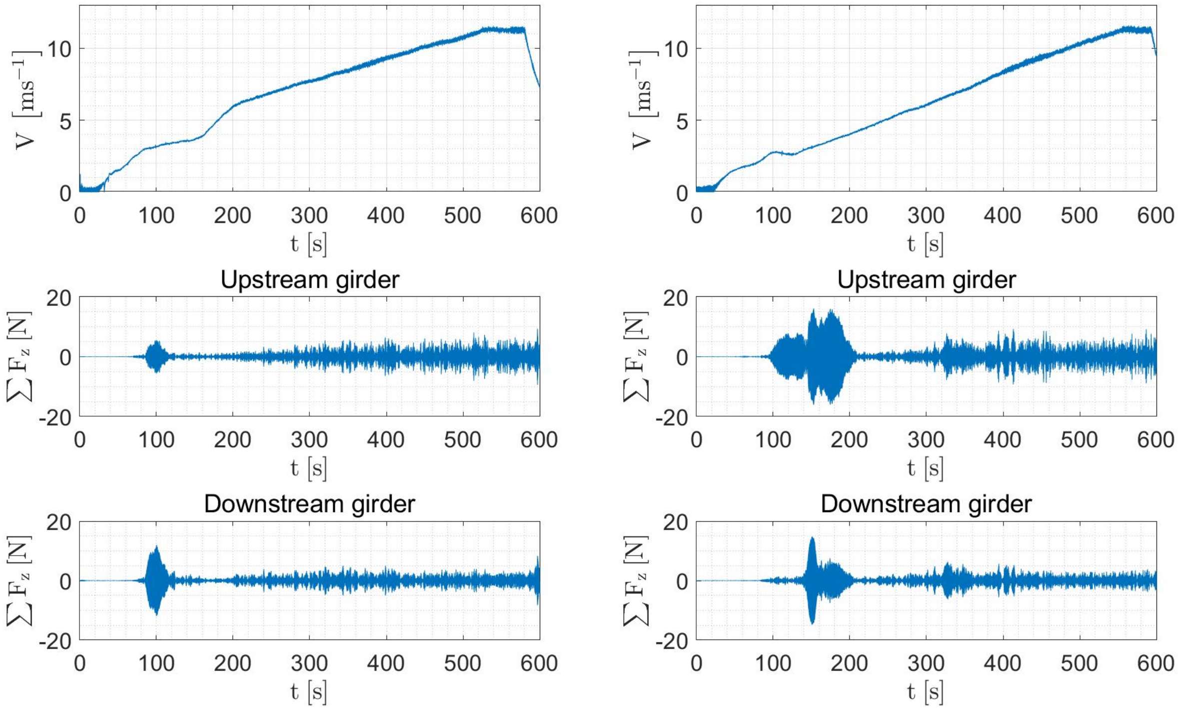

(a) Active TMD

(b) Disabled TMD

Figure 8.3: VIV test results for S2-G3

The Strouhal numbers calculated for the section models are investigated using the script *strouhalNumber.m*. Figure 8.4 displays the plot of the Strouhal numbers against the gap to depth ratios. The blue, red and green data points represent the configurations of S1, S2 and S3, respectively. All the configurations have a gap to depth ratios above the critical gap to depth ratio. Therefore, flow patterns as in moderate gap to depth ratios are expected. The flow detaches at the leeward side of the upstream girder and vortices emerge in the gap. A wake is formed behind the upstream girder, which interferes with the downstream girder. Higher values

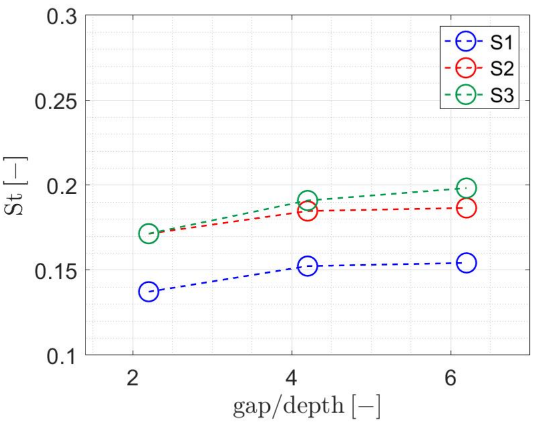

Figure 8.4: Strouhal number of section models

of the Strouhal number makes it more difficult to achieve the serviceability requirements of the bridge. Thus lower values of the Strouhal number are preferable, indicating that S1 has superior VIV performance compared to S2 and S3. The dashed line is a 2nd order polynomial fitted curve to each section model to emphasize the changes in the Strouhal number with altering gaps. Observed is the trend of increasing Strouhal number with increasing gap to depth ratio. The smaller gaps obtain superiour VIV performance, which is supported by Kwok et al. (2012).

From successive peaks in a damped free vibration time history, the damping ratio is determined using the script *damping.m*. Figures 8.5(a) and 8.5(b) show the vertical acceleration time series for S1 with the active and the disabled TMD, respectively. The decay of motion is captured by the envelope of the measurements defined by a logarithmic decrement. The calculated damping ratio for S2 with the active TMD is 0.5%, which differs from the damping ratio determined for S2 with the disabled TMD of 0.2%. The higher damping ratio of S2 with the active TMD suggests that the built-in TMD faster reduces the amplitude of the vibrations. The beating phenomenon is observed, where frequency components are closely located (Tamura and Kareem, 2013). The two girders of the twin-deck have close natural frequencies, which results in the girders alternately interfering constructively and destructively, amplifying and cancelling each other. A similar beating effect may occur when the girder frequency and the TMD are discordant due to imprecise tuning of the TMD. The acceleration time series and damping ratios are presented in Appendix G for each section configuration. The damping ratio is conservatively taken as 0.4% for all configurations. In the Norwegian bridge design code - N400, the damping ratio for suspension bridges is set to 0.2% (Statens vegvesen, 2015). The damping ratios are further used in the VIV performance assessments of the section models and the full-scale bridge decks.

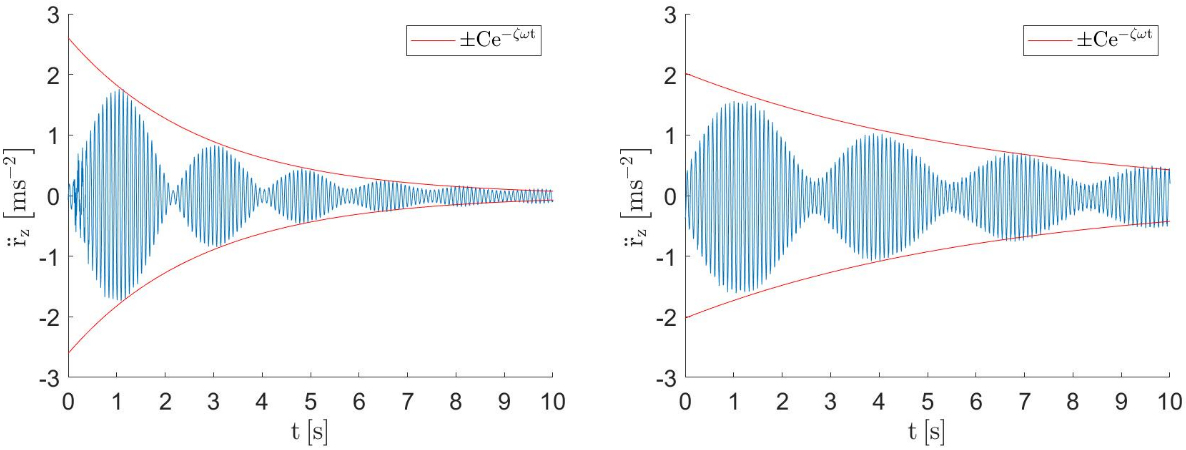

(a) Active TMD, $\zeta = 0.5\%$

(b) Disabled TMD, $\zeta = 0.2\%$

Figure 8.5: Decay of motion for S2

The Scruton numbers are computed in *scrutonNumber.m* to evaluate the propensity of the girders to vibrate due to vortex shedding. Figure 8.6(a) and 8.6(b) show the Scruton numbers plotted against the gap to depth ratio for the section models and the full-scale bridge decks, respectively. The blue, red and green data points respectively represent the configurations of S1, S2 and S3. A 2nd order polynomial fit is implemented as a dashed line between the data points of each girder shape. Observed is weak growth in the Scruton number with increasing gap for the full-scale bridge decks. Since the height is chosen as the characteristic dimension, the Scruton numbers of the section models are independent of alterations in the gap between the girders. The Scruton number appears to increase linearly with the mass. S2 is the lightest of the section models, while S1 is the lightest of the full-scale bridge decks. The proximity in weight may reason the swapped order of section models S1 and S2 in the estimation of the Scruton number. Present are the uncertainties related to the materials and assembly of the section models, including the repair of damages resulting in added mass. The Scruton number is a non-dimensional mass-damping parameter. To obtain section models comparable to real structures, a set of dimensionless parameter must be equal. The Scruton numbers calculated from the full-scale bridge decks are larger than the section models. As expected, larger vibrations due to vortex shedding are experienced in the wind tunnel compared to the bridge location.

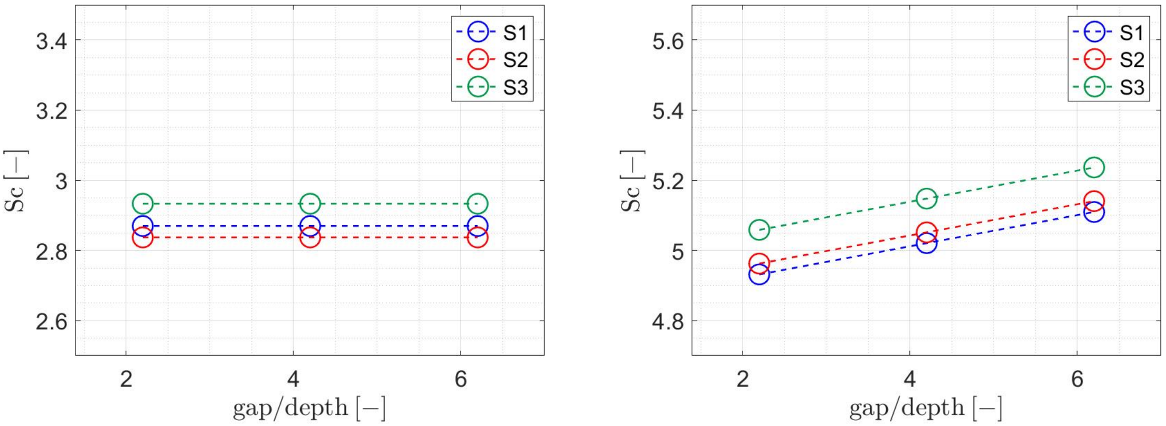

(a) Section models

(b) full-scale bridge decks

Figure 8.6: Scruton number

8.3 Static Coefficients

The static coefficients are obtained by quasi-static tests in the wind tunnel as described in Section 7.3.2 and processed using *staticCoeffAllTests.m*. The configurations are rotated with an amplitude of ±8 degrees and wind speeds of $V \approx 10$, 8 and 6 ms^{-1}. All figures in this section present the static coefficients as functions of α, denoting the bridge deck inclination angle with respect to the mean wind flow. The drag coefficients ($C_D(\alpha)$), lift coefficients ($C_L(\alpha)$) and moment coefficients ($C_M(\alpha)$) are plotted for each configuration, respectively.

Figures 8.8-8.10 plots the response of each section for the three different wind speeds. The multiple lines of the same colour are due to the plotting of the data from multiple rotations of the section models at each wind speed. The small deviations between the lines for the same wind speed highlight the sensitivity of the cross-sectional forces to the wind flow in a rotating motion. The exact wind speed at which the different tests were conducted can be seen in the legends of each plot. Configuration S2-G1 in Figure 8.9(a) is tested at $V = 9.1$ ms^{-1} as the configuration exhibited vortex-induced vibrations at $V \approx 10$ ms^{-1} which may affect the accuracy of the results.

An important property of the plots in Figures 8.8-8.10 is the lack of offset between the curves for different wind speeds. This implies that the static forces on the bridge deck do not depend on the wind speed. Hence, based on the obtained static coefficients the configurations can be said to have very low if any, Reynolds dependency.

All drag coefficients C_D have data appearing as a clean parabolic curve without deviations. The high values of C_D are to be discussed later in this section. The lift and moment coefficients, C_L and C_M, also show clear trends with typical linear development. The average values are smaller and more common than those of the drag coefficient C_D. Yielding for all gaps, C_L presents itself with negative values for $\alpha < 4$ degrees for configurations of S1 and S3, and $\alpha < 6$ for S2 implying that the mean vertical forces inflicted on the bridge deck by the wind flow works in a downward direction. An accelerated flow over the streamlined bottom surface entails larger pressures with negative values, causing negative average pressures for the whole bridge deck (Kwok et al., 2012). As an inclination angle of ±8 degrees is beyond what could be assumed as a realistic displacement for a bridge deck, the bridge decks will presumably exhibit merely negative values of the lift coefficients.

There are some appearing non-linearity at large negative inclination angles for the moment coefficients C_M. The noise from the vibration response of configuration S1-G1 is plotted together with the mean value lines in Figure 8.7 to illustrate the increased vibrations causing the slight non-linearity. At large negative values of α the wind flow is induced at the top surface of the bridge decks which may be causing a more turbulent flow around the sections consequently putting them in motion. Seen as the bridge decks does not exhibit noise of the same magnitude for positive values of α, the more streamlined design and guide-vanes on the bottom surface may seem to have a beneficial impact on the linearity of the static coefficients. By studying C_M in Figures 8.8-8.10, the non-linearities present in the plots seem to be minimal for S1, increased for S2 and most prominent for S3, magnified with increasing gaps for each section configuration. The observed pattern may be substantiated by the change in inner angles between the geometries for S1, S2 and S3 aggravating the turbulent flow.

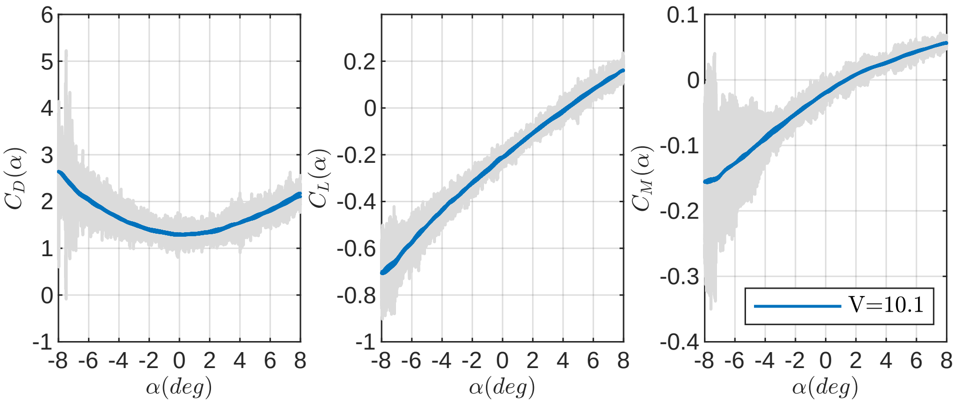

Figure 8.7: Static coefficients with plotted vibration response for S1-G1

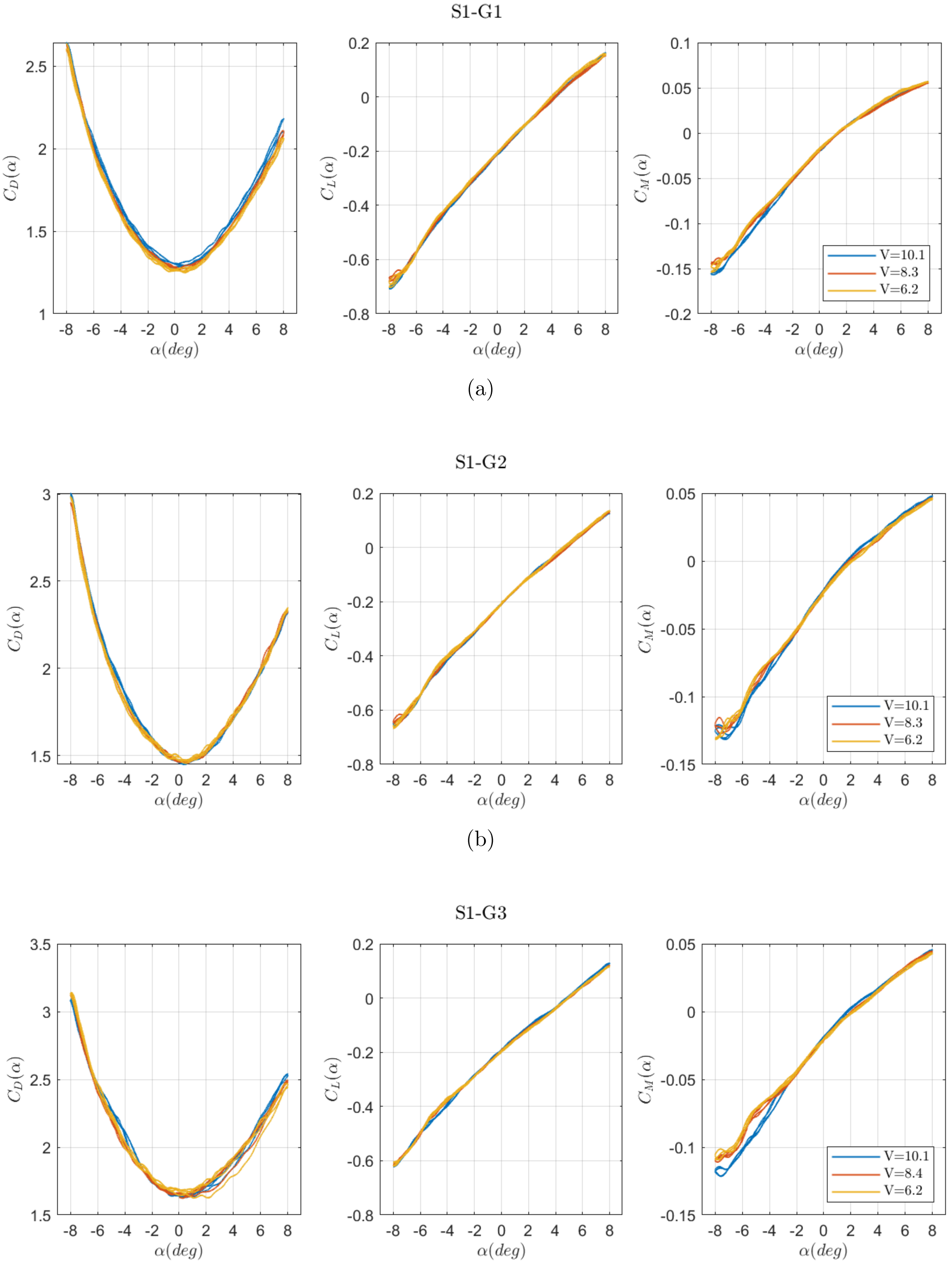

(a)

(b)

(c)

Figure 8.8: Static coefficients for configurations of section S1

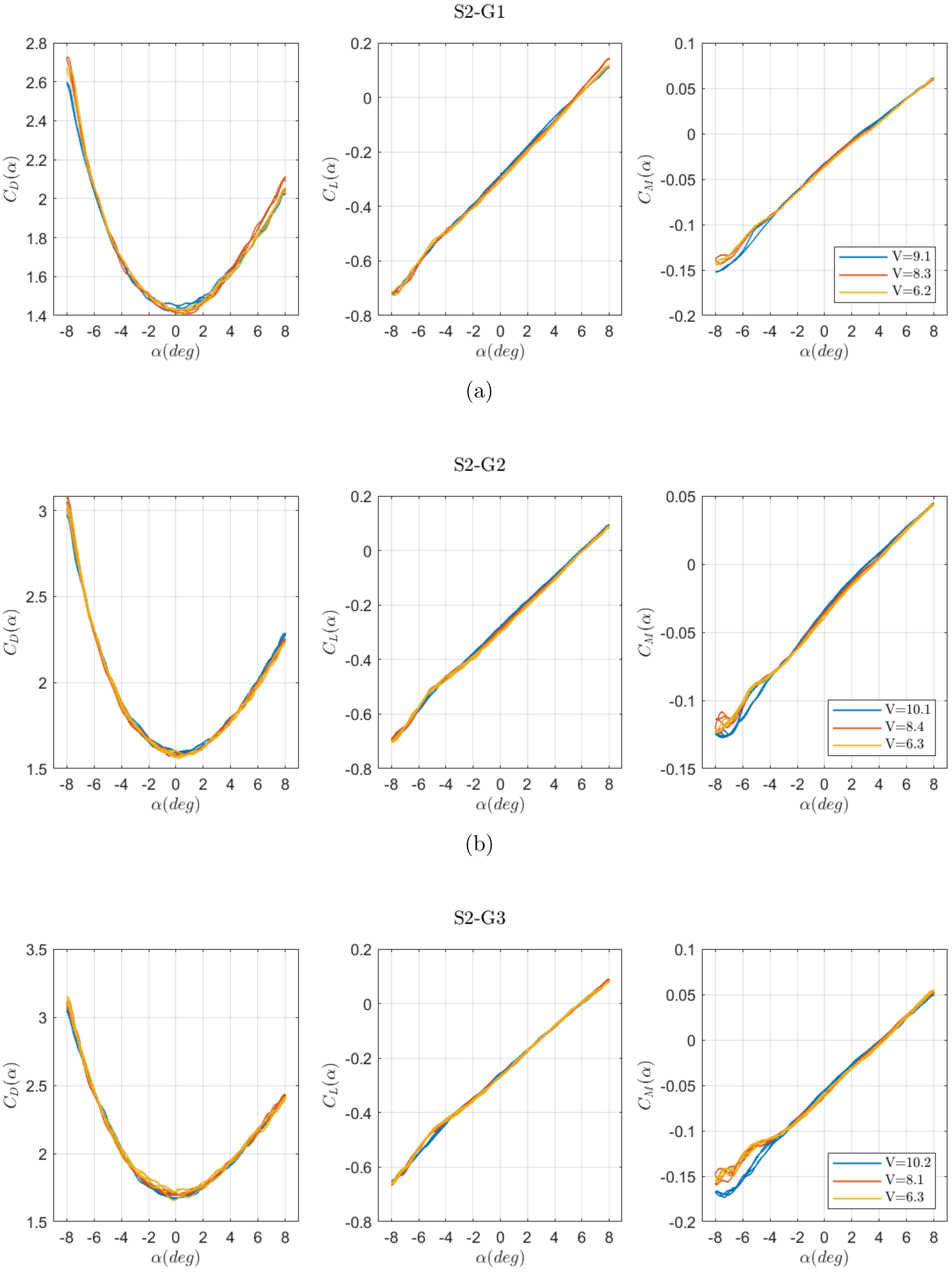

(a)

(b)

(c)

Figure 8.9: Static coefficients for configurations of section S2

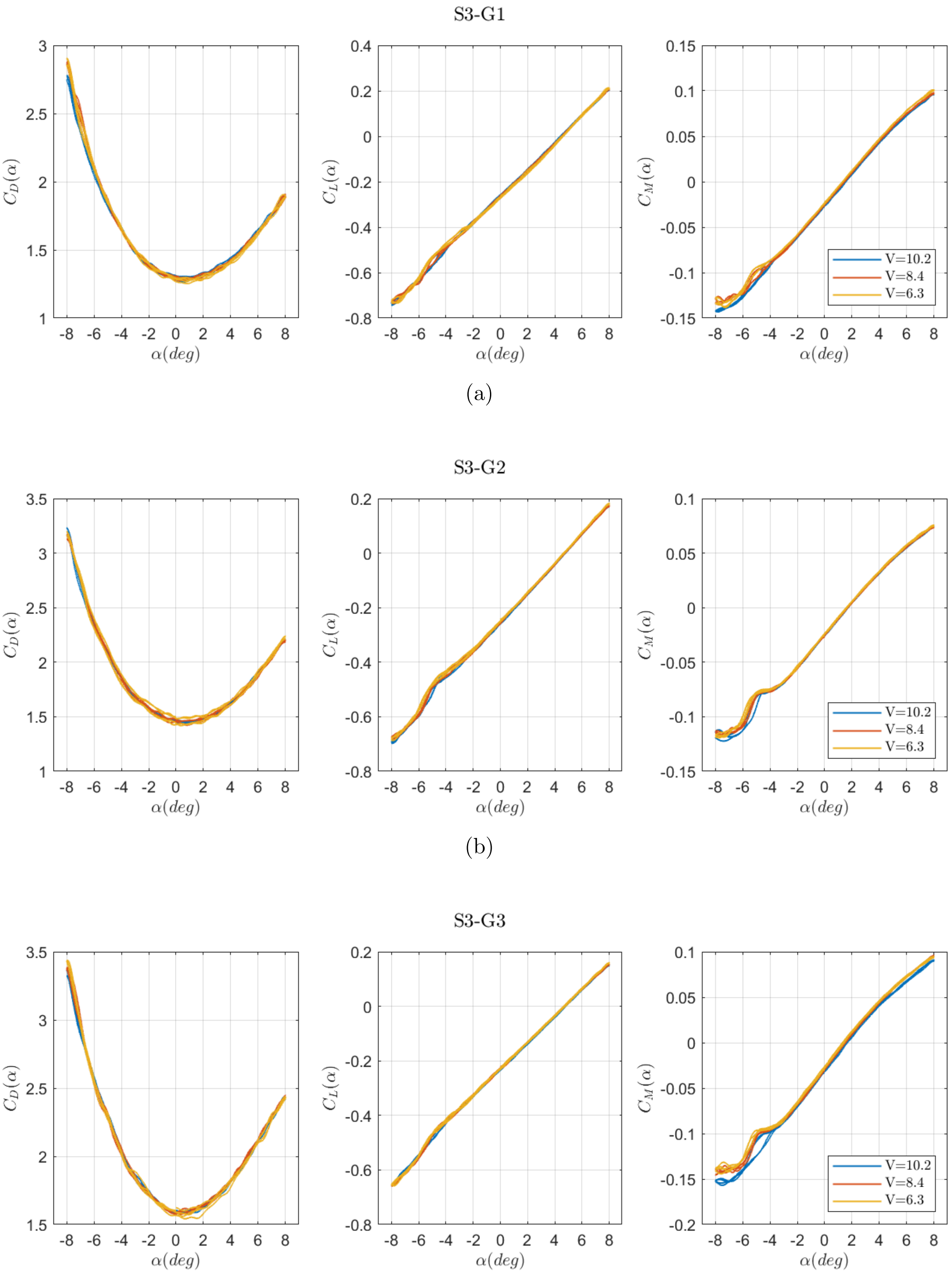

(a)

(b)

(c)

Figure 8.10: Static coefficients for configurations of section S3

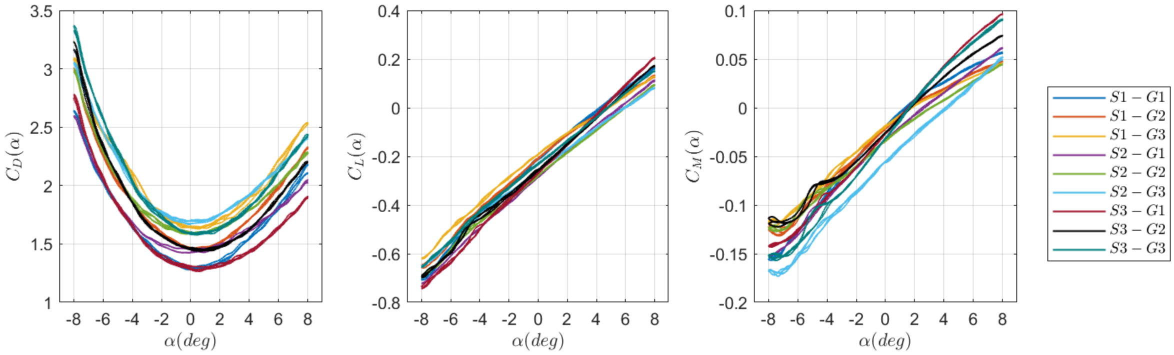

Figure 8.11: Static coefficients for all configurations at $V = 10\,ms^{-1}$

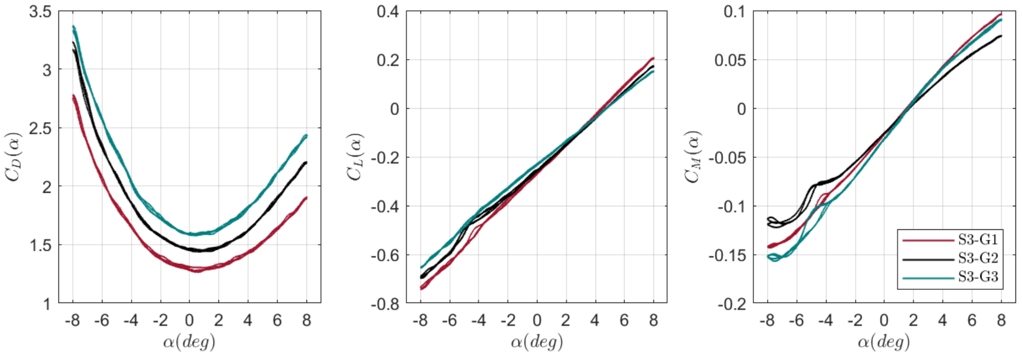

Figure 8.12: Static coefficients for configurations of S3 at $V = 10\,ms^{-1}$

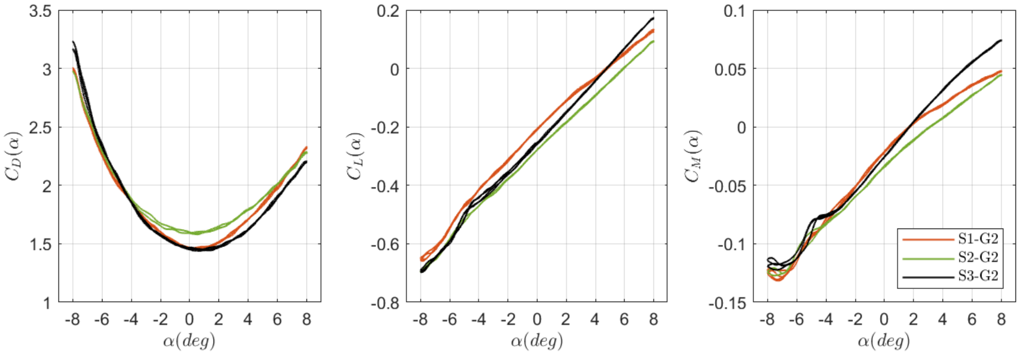

Figure 8.13: Static coefficients for configurations of gap G2 at $V = 10\,ms^{-1}$

For enhanced visualization of the diversity between the static coefficients, a plot containing static coefficients for all configurations at wind speed $V \approx 10$ ms^{-1} can be found in Figure 8.11. All configurations display the same shapes in the curves for each coefficient with only minor deviations. The drag coefficients appear to vary with a shift in values, while the lift and moment coefficients are separated with different inclinations of the linear trends. A low inclination is preferred for C_L and C_M as steeper curves can indicate that the forces acting on the bridge decks are of greater magnitude.

In general, it is desirable that the value of $C_M(\alpha)$ is zero at $\alpha = 0$ degrees to prevent that the cross-sections rotate when exposed to wind flow in a neutral position. An offset from zero in $C_M(\alpha)$ of approximately -0.025 can be observed for all configurations except S2-G3. A negative shift in $C_M(\alpha)$ is evident for S2-G3, consequently resulting in twice the magnitude in the offset of approximately -0.05. This may indicate that the configuration is slightly less resistant to rotations than the other configurations. Both offset values are still small indicating fairly good rotational stability.

As mentioned, the values of the drag force coefficients C_D are rather high with a range of 1.3-3.5. A possible explanation for the high values is that the used reference height and length of the cross-section should be equivalent to the area that is up against the wind flow. Consequently, for a twin-deck section, the additional area from the second girder adding additional drag forces to the configuration is not accounted for.

There is an interesting pattern to the average values of the drag coefficient C_D for varying gaps. By plotting section S3 individually in Figure 8.12, it becomes clear that the values of C_D increases with an increasing gap. Identical plots for S1 and S2 revealing a similar pattern can be found in Appendix H. The fact that the smallest gap gives lower values may be explained by less propensity of vortexes shedding in the gap. As the gap increases the wake behind the first girder may induce larger positive drag forces behind the upstream girder simultaneously increasing the value of the total drag coefficient.

The inclination of the linear trends in Figure 8.12 seems to decrease with increasing gaps. With a sufficiently large gap, the pressure difference between top and bottom surfaces may cause vortexes to enter the gap increasing the fluctuating pressures on the downwind girder and increasing the drag force (Kwok et al., 2012). The plots for S1 and S2 show great similarities with the patterns for each of the coefficients in Figure 8.12 with one evident deviation being the negative shift in values for C_D for configuration S2-G3. However, S2-G1 and S2-G2 are coherent with the previously mentioned pattern.

As the configurations do not have one varying parameter but are combinations of three cross-sections and three gaps, finding a geometrical pattern in relation to the response in static forces is more complicated. In means of revealing or dismiss such a relation, the three section types are plotted for gap G2 in Figure 8.13. The plots state the fact that a larger gap seems to give fewer variations in C_D, while having the opposite effect on C_D. The configurations of S2 seem to exhibit higher drag forces than S1 and S3. One of the geometrical differences between the sections is the inner angle of the girders. If this appears to be decisive, the angle of S2 may have caused increased turbulence in the flow in the large gap adding drag to the respective girders. The lift coefficient, C_L, seems to be less affected by varying gaps. Same plots for all three gaps, revealing a similar patterns for gaps G1 and G3 are presented in Appendix H.

Configuration S2-G3 deviates from the other eight configurations. It is less coherent with the observed patterns in addition to the negative shift in values for the moment coefficient C_M. This raises the question if the configuration does in fact have other aerodynamic properties than the others, or if the bad reading of response from the load cells during wind tunnel testing has resulted in inaccurate values.

Due to the negligible wind speed dependency of the static coefficients, plots for comparisons between the configurations have only been produced for $V \approx 10$ ms^{-1}. Yielding for Figures 8.11 and 8.12as well as the plots present in Appendix H.

8.4 Aerodynamic Derivatives

This section analyses the experimentally obtained aerodynamic derivatives (ADs) P^*_{1-6}, H^*_{1-6} and A^*_{1-6} for each of the nine configurations as well as a quantitative comparison between the configurations. The ADs for each of the configurations have been obtained by forced vibration tests in the wind tunnel as described in Section 7.3.3. The experimental was processed using the Matlab script *aerodynamicDerivativesAllTests.m*.

The ADs are related to the sections by the length of the section models (L) and the width (B) for each configuration. All figures plots the ADs as functions of reduced frequency (K) instead of reduced velocity (V_r). Plotting the ADs as functions of reduced frequency enhances the variations due to different geometric forms and gaps of the configurations. If the ADs are plotted as functions of V_r they obtain close-to-zero values at low reduced velocities, this is avoided when plotting them as functions of K (Øiseth et al., 2010). Common for all figures is that the ADs are organized identically to the stiffness and damping matrices related to the SE forces, $\hat{K}_{ae}$ and $\hat{C}_{ae}$, as seen in Section 3.4.3.

Figure 8.15 show scatter plots of the AD data points for configuration S1-G1 as functions of reduced frequency, plotted for each wind speed at which they were obtained. The colour definition is illustrated in Figure 8.14. Identical plotted ADs for the remaining configurations are presented in Appendix I. The scatter plots with separated wind speeds are favourable to evaluate if the trend differs for ADs obtained at different wind speeds, i.e. show Reynolds dependency.

There is an overall tendency of the ADs to have minimal offsets between the data points extracted at different wind speeds. Even though the trends in the damping related drag force coefficient P_2^* displays a clear offset in Figure 8.15, its values are of significantly less magnitude than the other coefficients resulting in the offset being negligible. The lack of offset suggests that the ADs are independent of wind speed implying that the sections may possess little to no Reynolds dependency. The minimal presence of offset between the trends also puts emphasis on the choice to present the rest of the results with combined data from both wind speeds without distinction.

The coefficient H_1^* in Figure 8.15 appear to have two separate trends for the different wind speeds for S1-G1. Similar divergent trends can be observed for H_1^* for S1-G2, S2-G1, S2-G3 and S3-G3, as well as for P_1^* for S1-G2, S1-G3, S2-G2, S3-G1 and S3-G3. This can also be observed in the background scatter of Figures 8.17 - 8.25 even if the experimental ADs are not distinguished for the two wind speed. When the coefficients develop two separate trends it may seem as the linear model used to estimate the damping related ADs do not fit the time-series for the mentioned ADs.

Figure 8.14: Legend for Figure 8.15

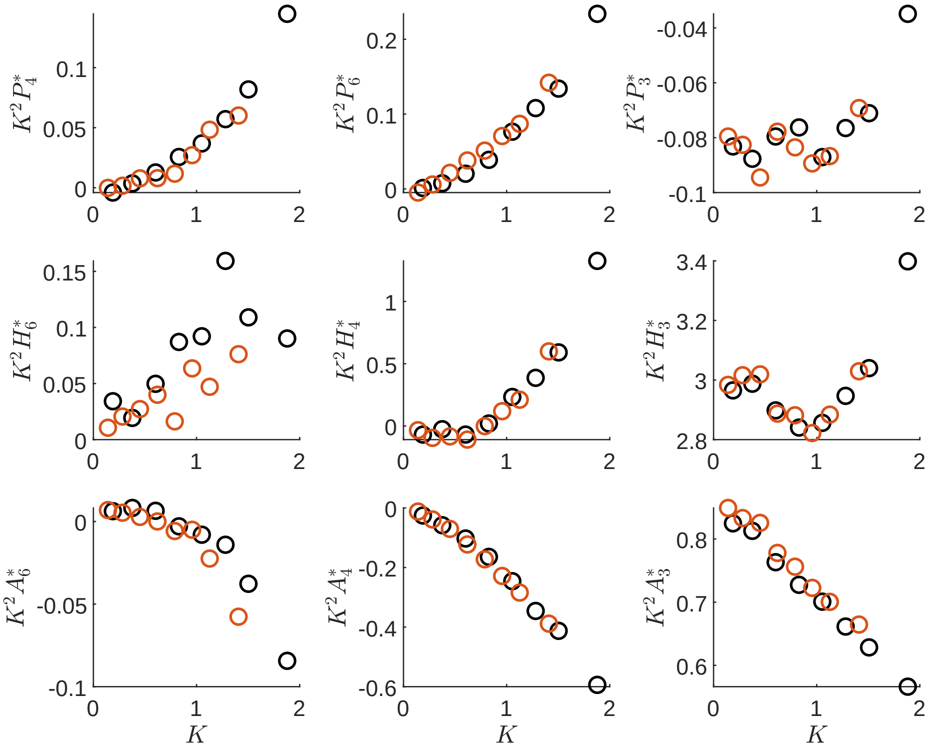

ADs related to $\hat{K}_{ae}$ for S1-G1

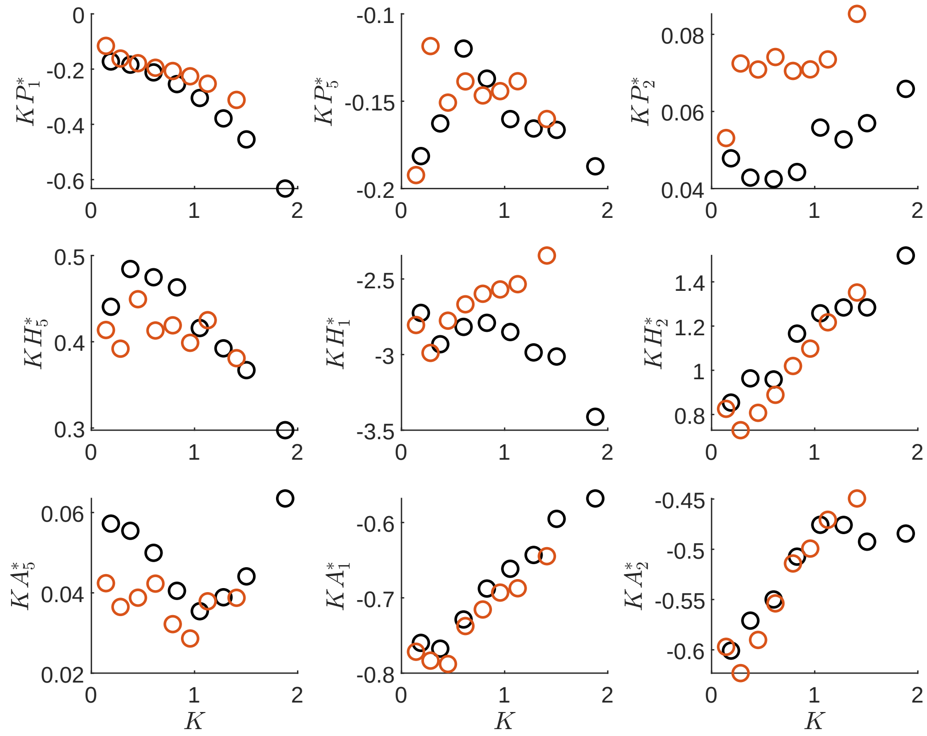

ADs related to $\hat{C}_{ae}$ for S1-G1

Figure 8.15: ADs plotted as functions of reduced frequency for S1-G1, obtained at wind speeds $V = 6\ ms^{-1}$ and $V = 8\ ms^{-1}$

Figures 8.17 - 8.25 contains stiffness and damping related ADs with a third-degree polynomial curve fitted to the data points. The grey circular points indicate the experimentally obtained data points for the ADs while the green line indicates the polynomial curve, both as functions of reduced frequency. Legend for the plots can be found in Figure 8.16.

The ADs are evaluated based on the presence of scatter with the polynomial fitted curves. The less critical ADs related to the self-excited drag force, P_{1-6}^*, has a more frequent occurrence of scatter. The overall magnitude of P_{1-6}^* for all configurations is low making them prone to dominance from inertia forces which can be a possible explanation for the scatter. The damping related coefficient P_2^* possesses evident scatter for all configurations making for the increased inaccuracy of the obtained polynomial fittings of this particular AD. P_1^* is also damping related and possesses positive values for configurations S2-G1 and S3-G1 for $K > 1$. This would indicate that these configurations could have a presence of negative drag damping which is unusual behaviour.

The ADs, H_{1-4}^* and A_{1-4}^*, may be important for the stability and show little to no scatter for the configurations assuring good accuracy for the polynomial fitted curves, with exception of H_1^*. The previously mentioned deviating trends for the coefficient H_1^* for some of the configurations consequently makes for a worse polynomial fit. This may introduce uncertainties in the calculation of the stability limit. H_1^* is related to self-excited forces in the vertical direction. The presence of higher-order self-excited forces could also be a reason for increased scatter.

Analysis of the ADs influence on motion-induced instabilities is conducted using Figure 8.26 containing the third-degree polynomial fitted curves for all configurations as functions of K. The motion-induced instabilities and the relation to the ADs, together with the equations relating the ADs to the self-excited drag, lift and moment forces, are presented in Section 3.3.

The damping related AD H_1^* influences the damping of the vertical vibrations of the configurations. In Figure 8.26 it can be seen that all values for H_1^* are negative implying that neither of the configurations have risk of galloping. S1-G1 and S1-G3 exhibit larger negative values for high reduced frequencies than the others, which may be beneficial.

A_2^* is also damping related but influences the vibrations in the torsional direction. Its values in Figure 8.26 show overall negative values implying that neither of the configurations are prone to torsional flutter. The negative values cause positive damping therefore A_2^* could improve the results in the stability limit calculations.

The stiffness related AD A_3^* influences the torsional vibrations and should be of negative value to eliminate the risk of static divergence. This is not the case in Figure 8.26 as A_3^* possesses positive values for all configurations which has a destabilizing effect on coupled flutter consequently decreasing the stability limit (Trein and Shirato, 2011). The prominent high values of all girder configurations of sections type S3 could consequently reduce the stability limit additionally.

The product between H_3^* and A_1^* only has a stabilizing effect when exhibiting negative values. Since only A_1^* is negative this particular requirement is fulfilled. Anyhow, the high absolute values of H_3^* is concerning as it is disadvantageous towards coupled flutter and could consequently decrease the stability limit of the configurations.

The polynomial fitted curves of the different configurations in Figure 8.26 are compared. For several of the different ADs the configuration S1-G3 is prominent with values of the highest magnitude. This yields for the stiffness related ADs P_6^*, P_3^*, H_4^* and H_3^*, in addition to the damping related ADs P_2^* and H_1^*. In general between the section configurations, S3 configurations are prominent for H_3^* and A_1^*. The ADs exhibit higher absolute values than S1 and S2. The configurations of S3 also possesses high values for A_3^* together with S1-G1 and S2-G1.

The configuration of S3-G1 seems to vary less than the others as the reduced frequency increases in Figure 8.26. It generally has low absolute values and more linear trends. If the values of the ADs approach constant values, this may imply that the AD is frequency independent. The same trends with a slight increase in variation can be found to yield for S2-G1 as well. Meanwhile, S3-G2 has a tendency to be in intermediate positions with respect to the other curves. It is rarely of the lowest nor the highest magnitude in values. This is only the case for P_1^* at higher reduced frequencies as the coefficient has an evident offset from the others at $K = 0$.

A figure containing ADs for all configurations plotted as functions of reduced frequency V_r is included in Appendix I. It displays the bad presentation of the ADs for low values of V_r. Due to V_r being dependent on the varying section model widths B, the AD data is obtained for different ranges of V_r.

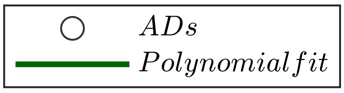

Figure 8.16: Legend for Figure 8.17-8.25

ADs related to $\hat{K}_{ae}$ for S1-G1

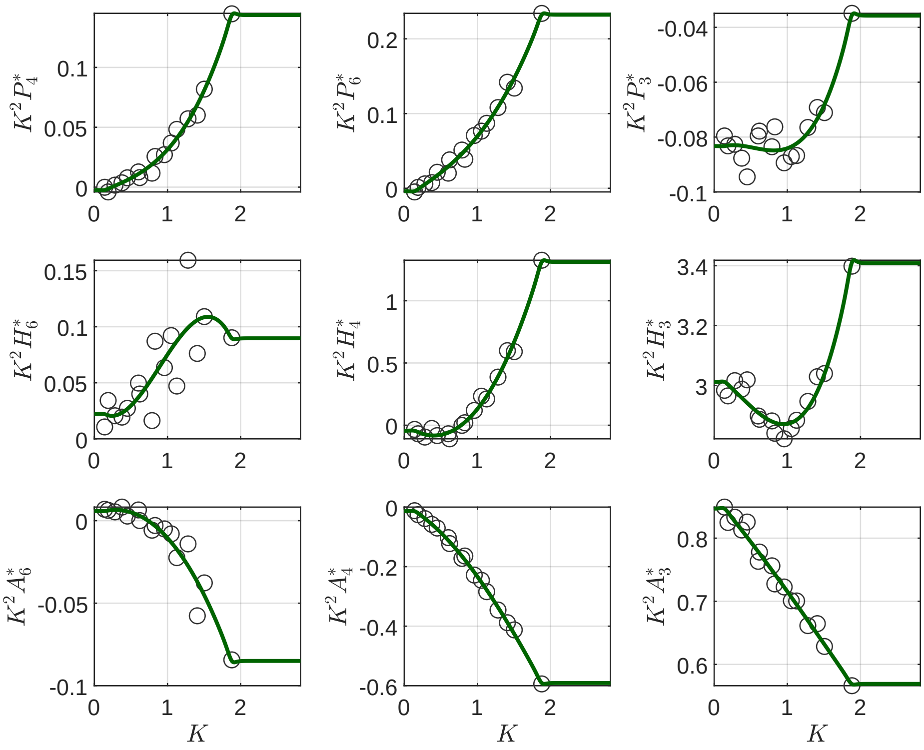

ADs related to $\hat{C}_{ae}$ for S1-G1

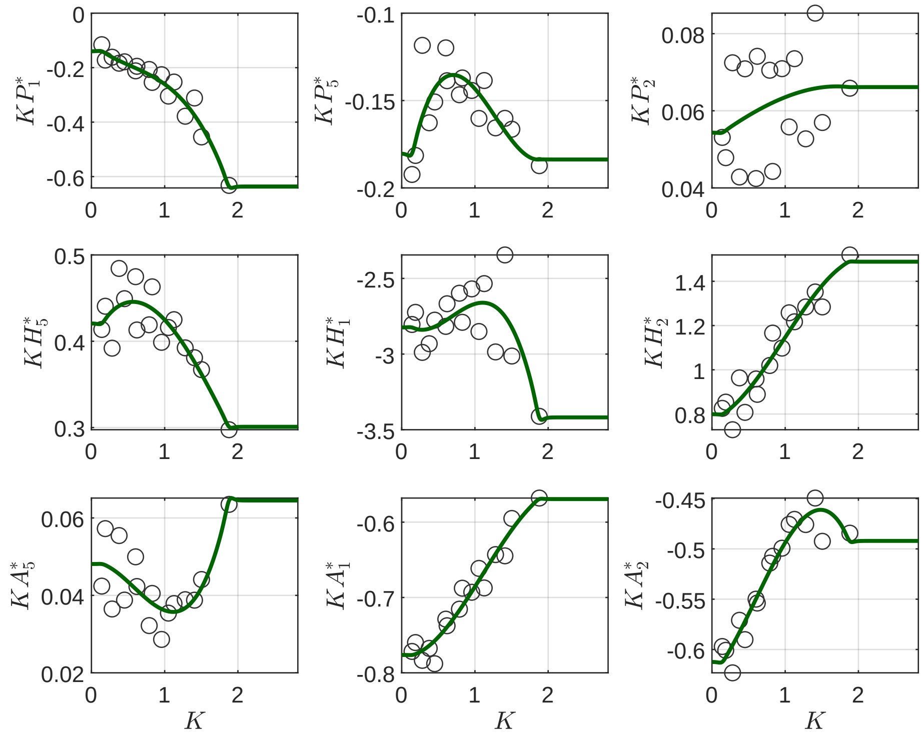

Figure 8.17: ADs for S1-G1

ADs related to $\hat{K}_{ae}$ for S1-G2

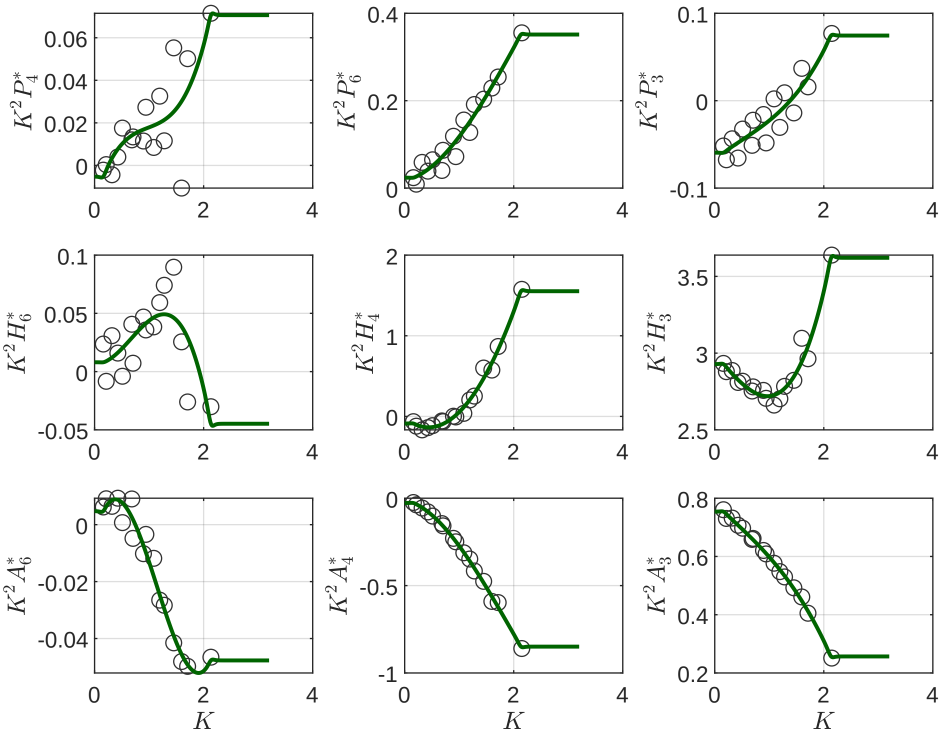

ADs related to $\hat{C}_{ae}$ for S1-G2

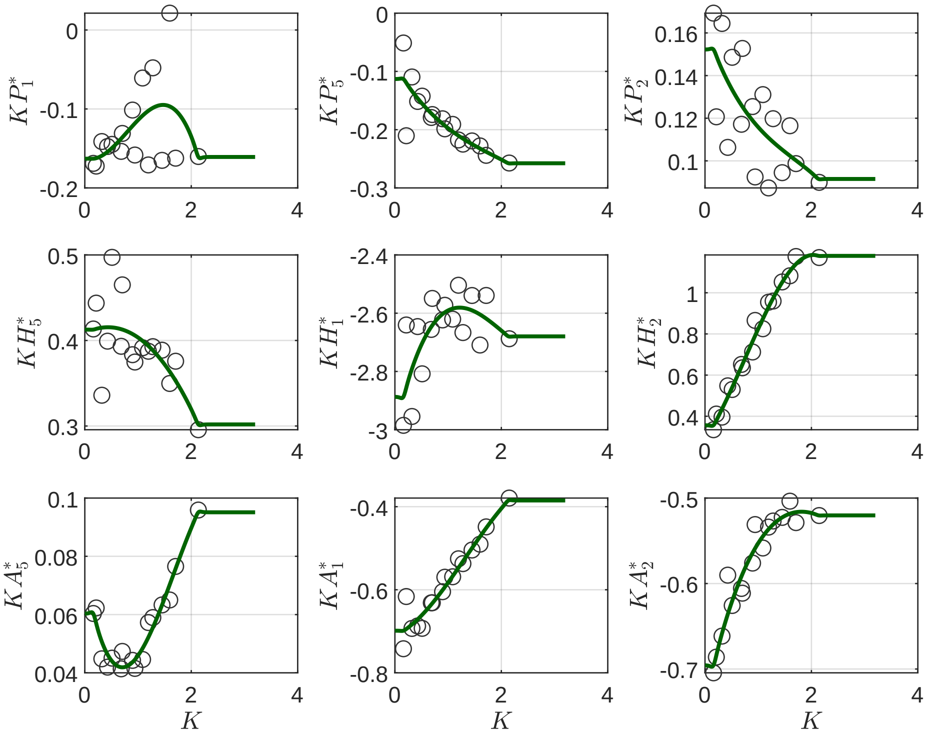

Figure 8.18: ADs for S1-G2

ADs related to $\hat{K}_{ae}$ for S1-G3

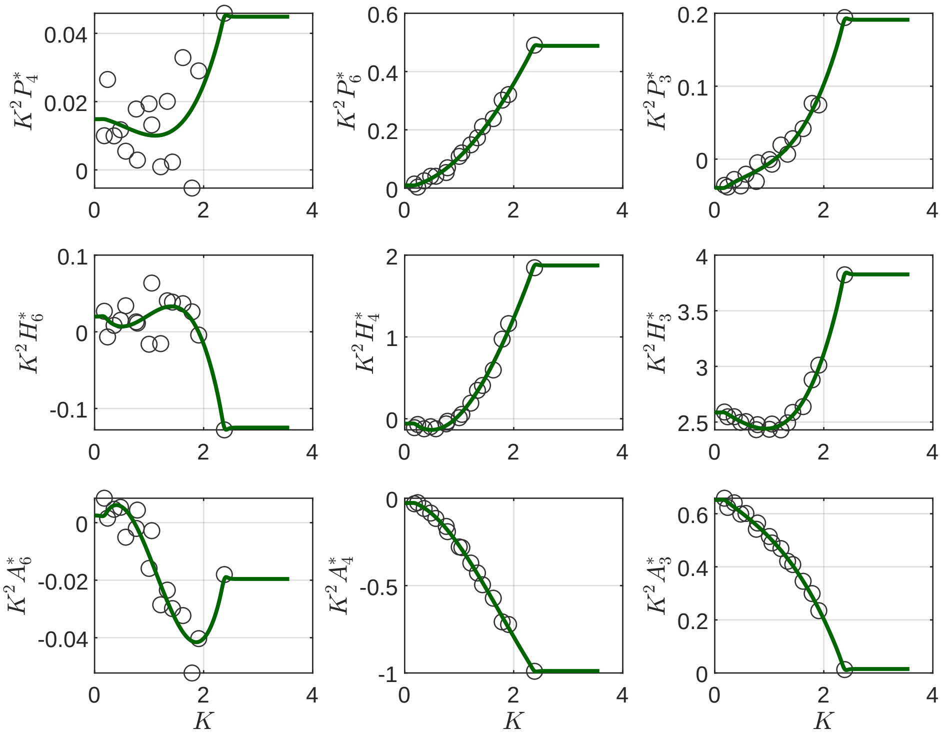

ADs related to $\hat{C}_{ae}$ for S1-G3

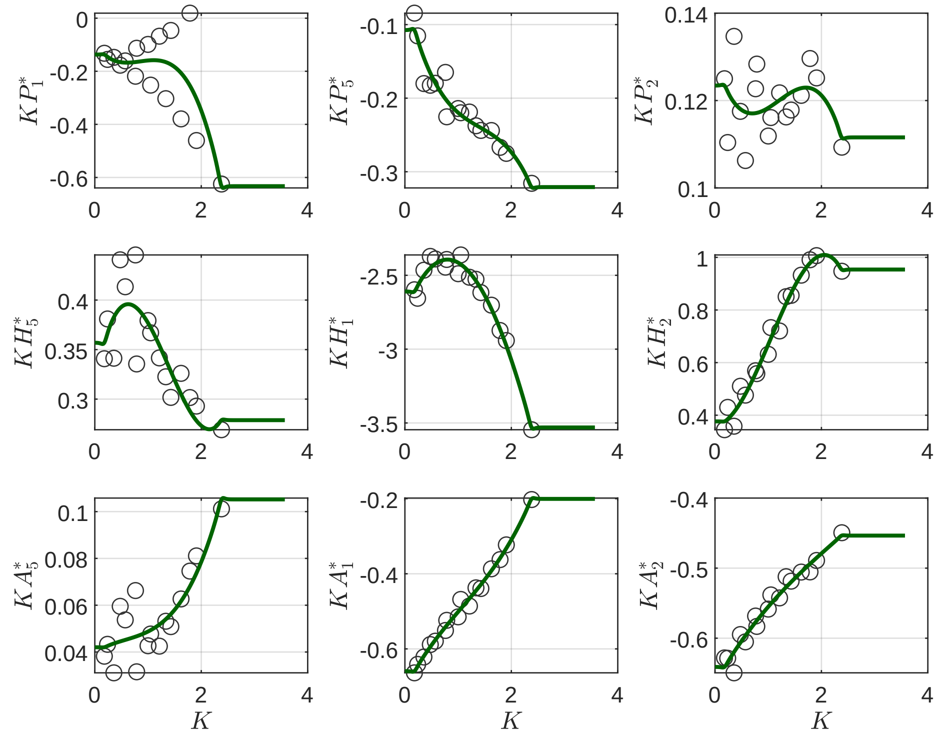

Figure 8.19: ADs for S1-G3

ADs related to $\hat{K}_{ae}$ for S2-G1

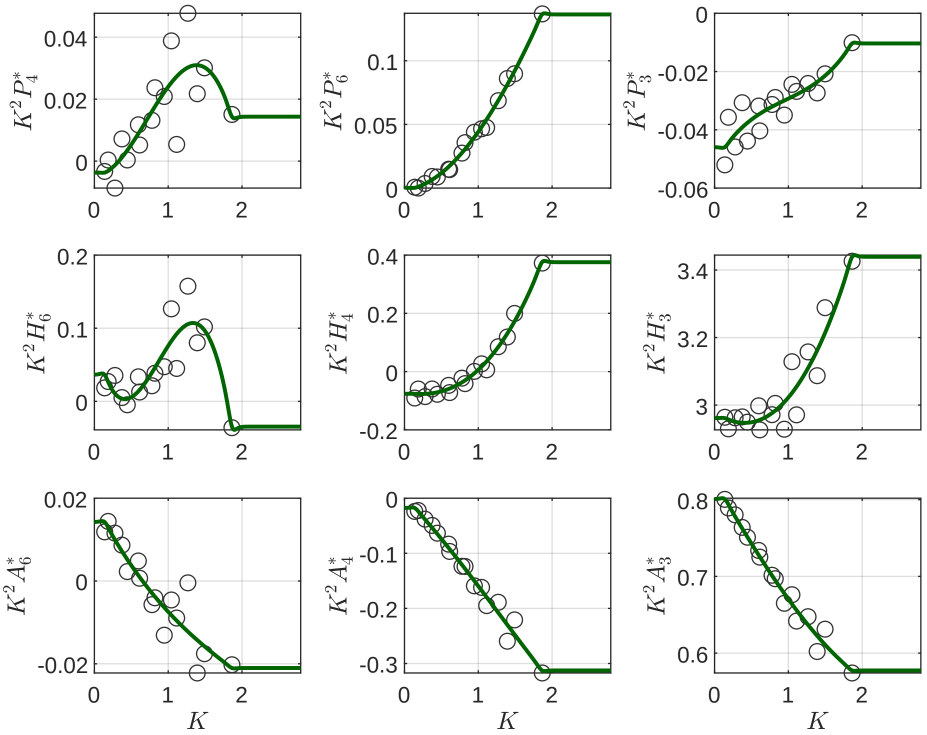

ADs related to $\hat{C}_{ae}$ for S2-G1

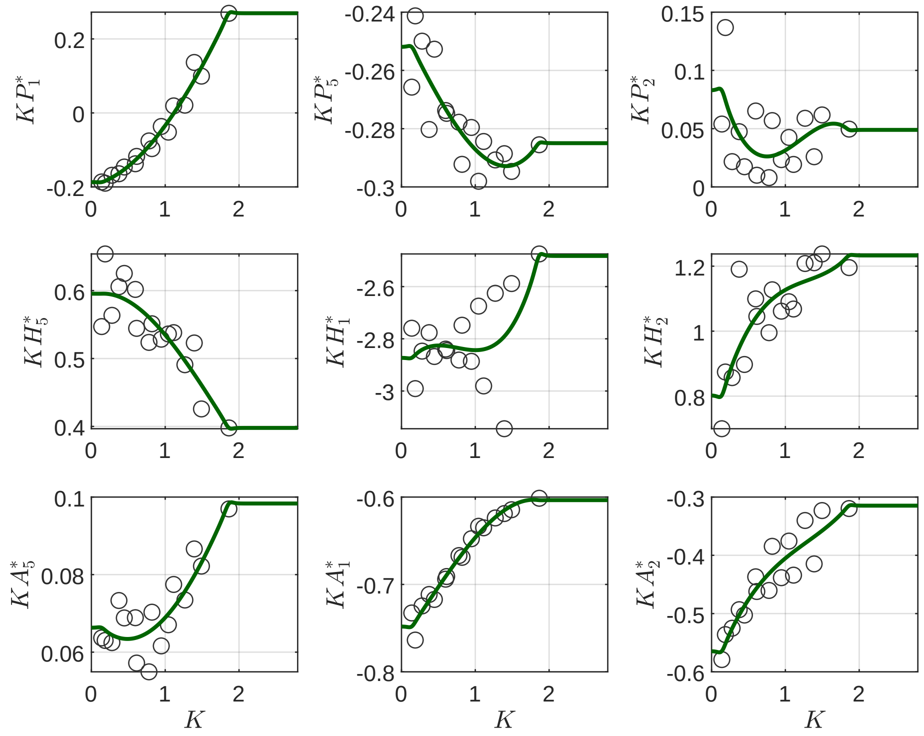

Figure 8.20: ADs for S2-G1

ADs related to $\hat{K}_{ae}$ for S2-G2

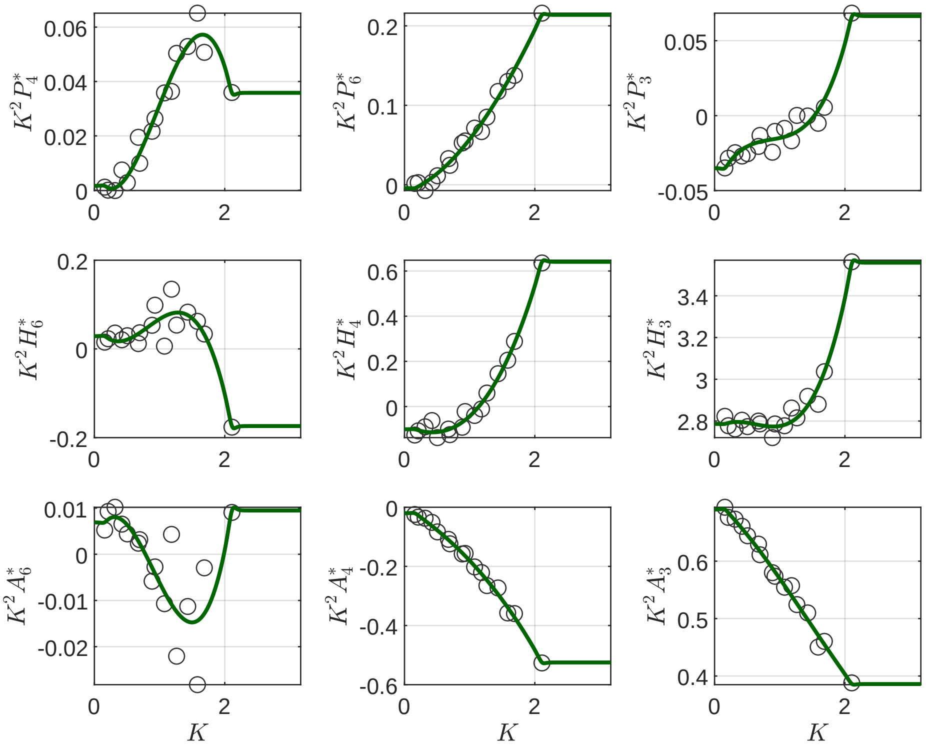

ADs related to $\hat{C}_{ae}$ for S2-G2

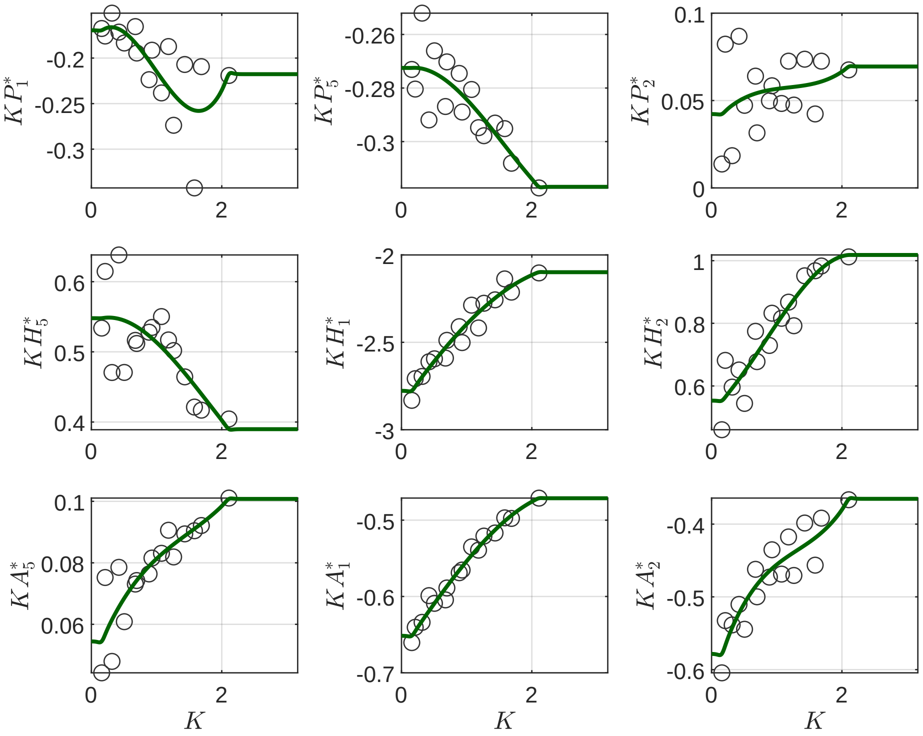

Figure 8.21: ADs for S2-G2

ADs related to $\hat{K}_{ae}$ for S2-G3

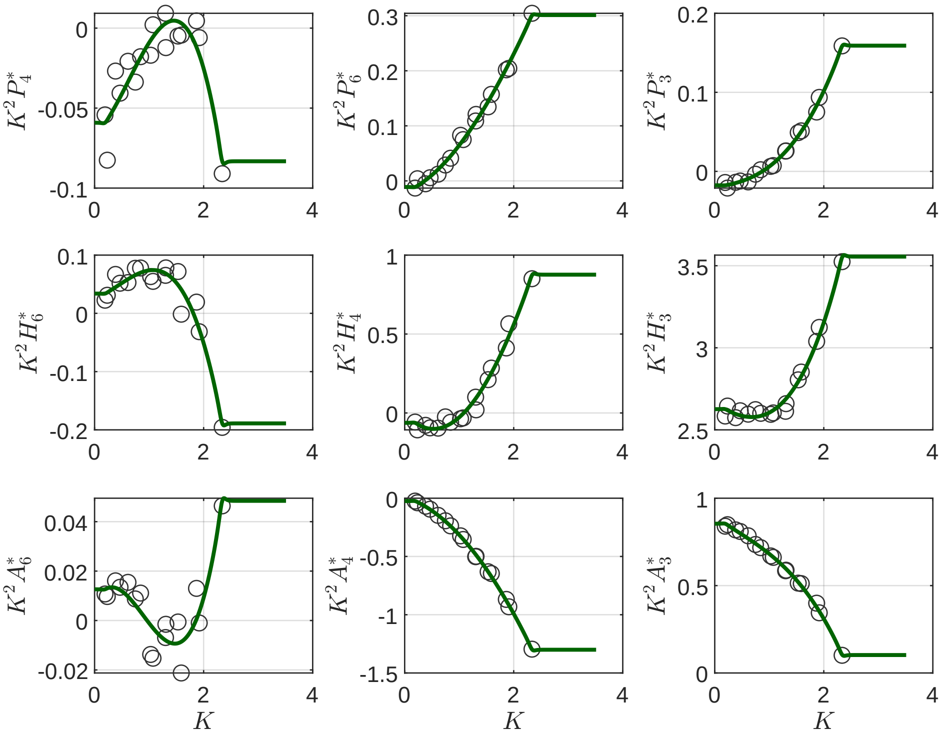

ADs related to $\hat{C}_{ae}$ for S2-G3

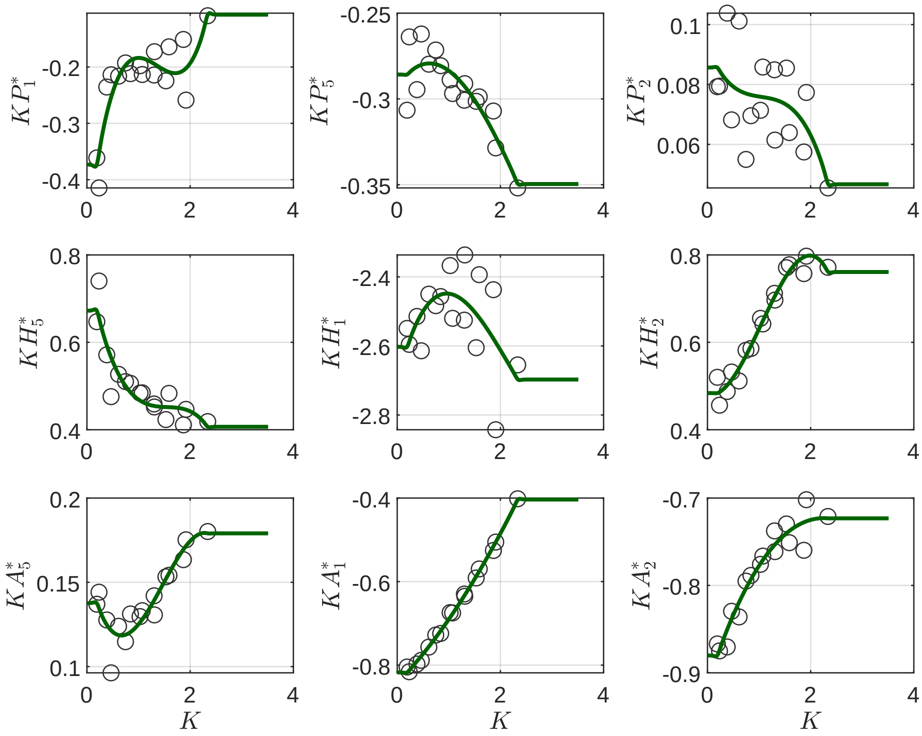

Figure 8.22: ADs for S2-G3

ADs related to $\hat{K}_{ae}$ for S3-G1

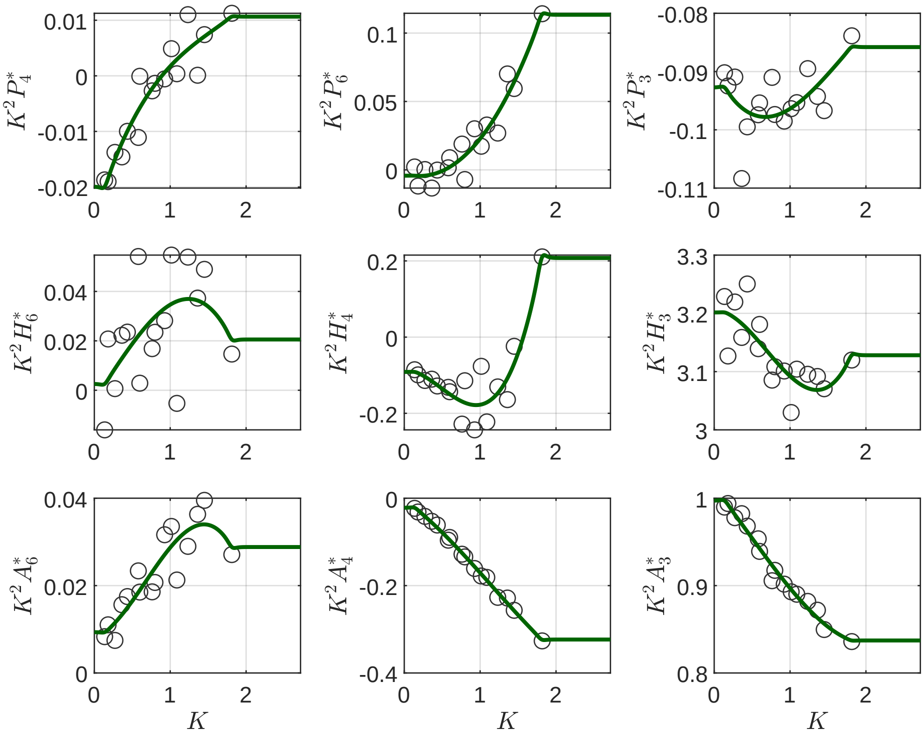

ADs related to $\hat{C}_{ae}$ for S3-G1

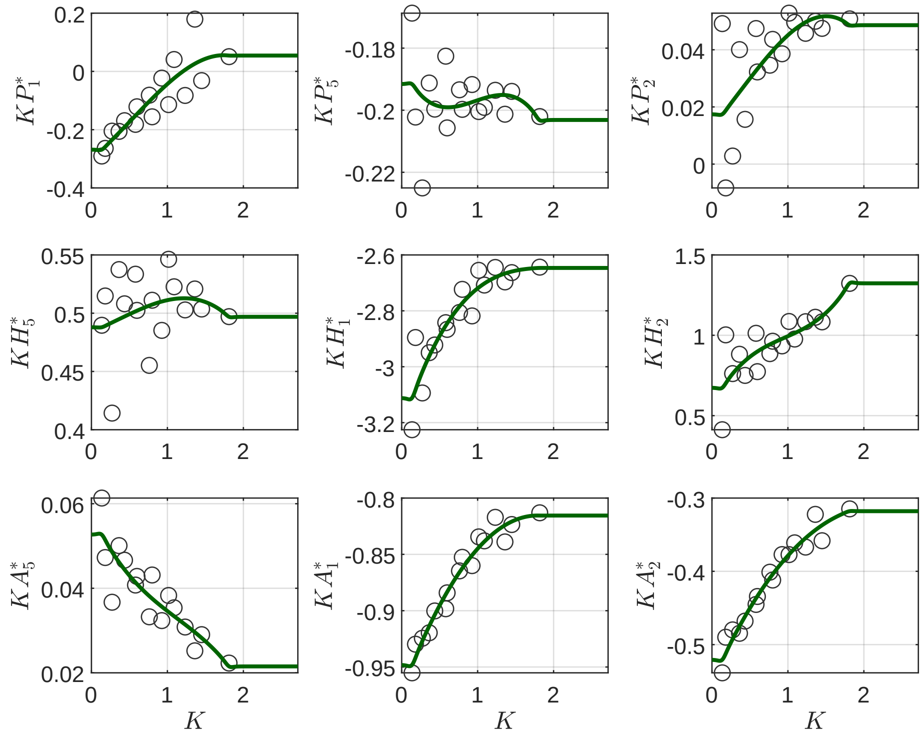

Figure 8.23: ADs for S3-G1

ADs related to $\hat{K}_{ae}$ for S3-G2

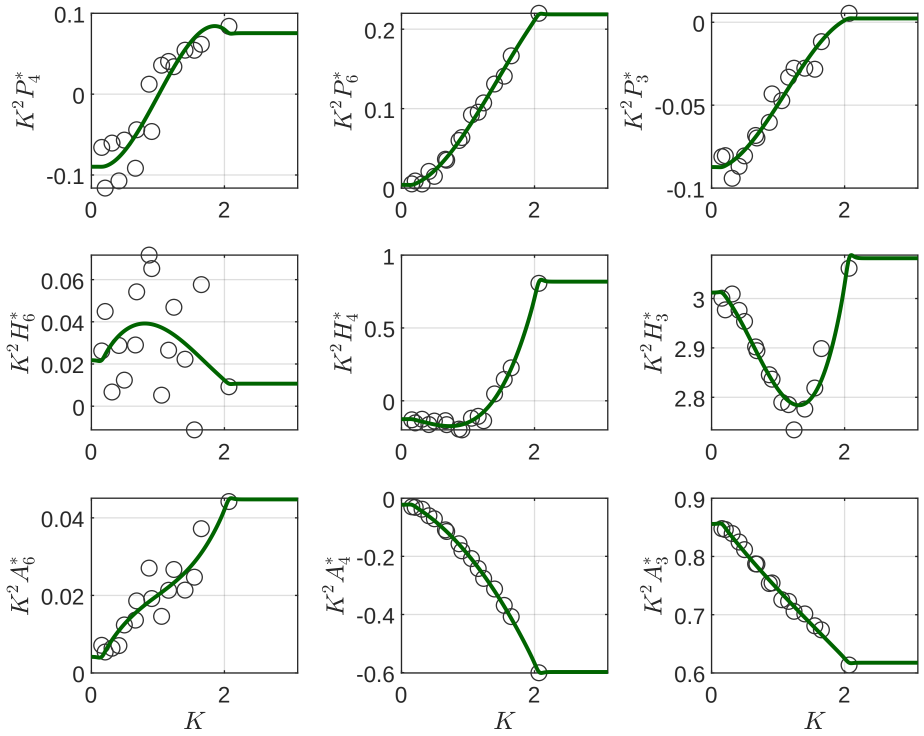

ADs related to $\hat{C}_{ae}$ for S3-G2

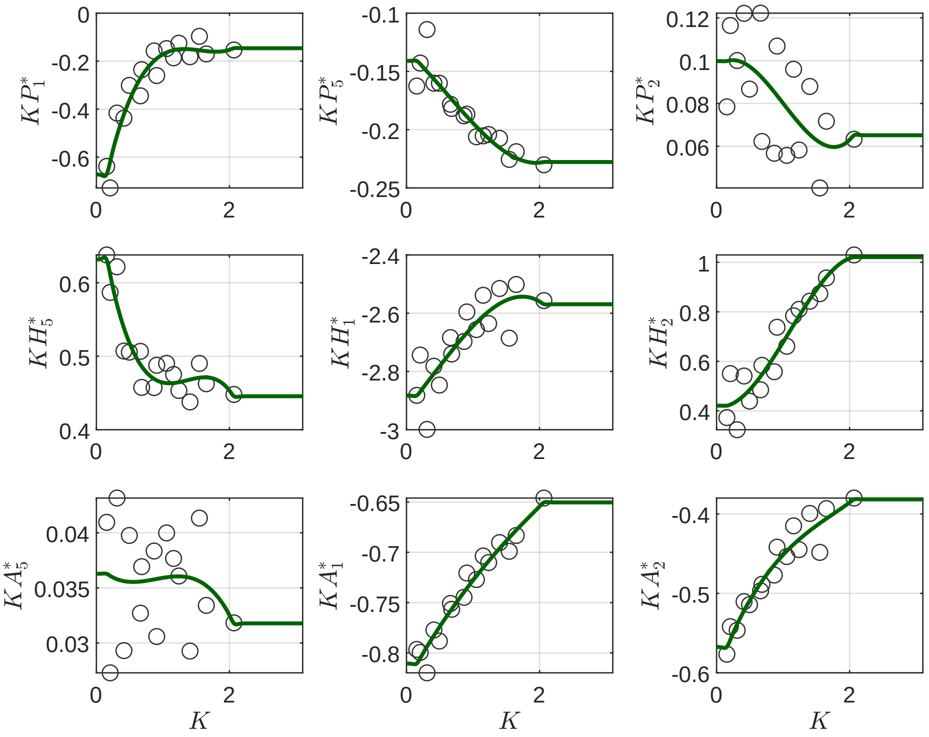

Figure 8.24: ADs for S3-G2

ADs related to $\hat{K}_{ae}$ for S3-G3

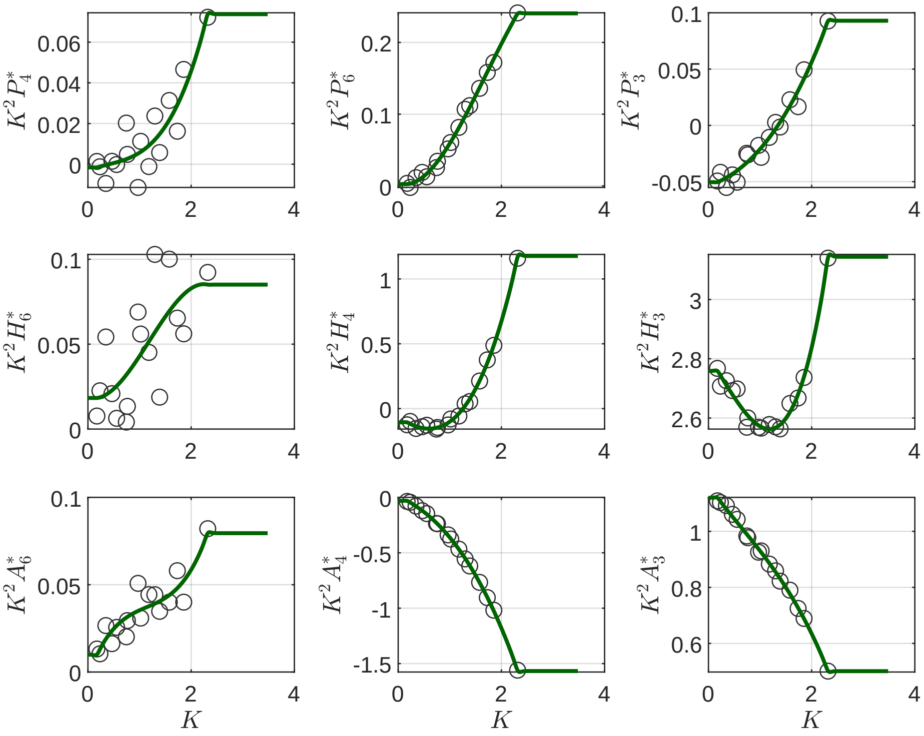

ADs related to $\hat{C}_{ae}$ for S3-G3

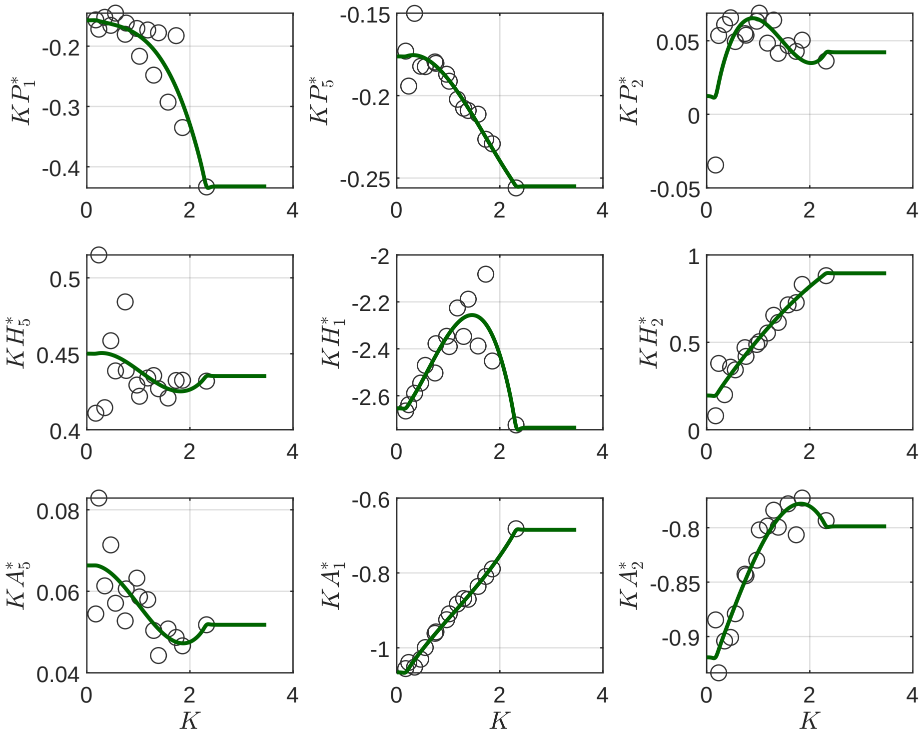

Figure 8.25: ADs for S3-G3

ADs related to $\hat{K}_{ae}$

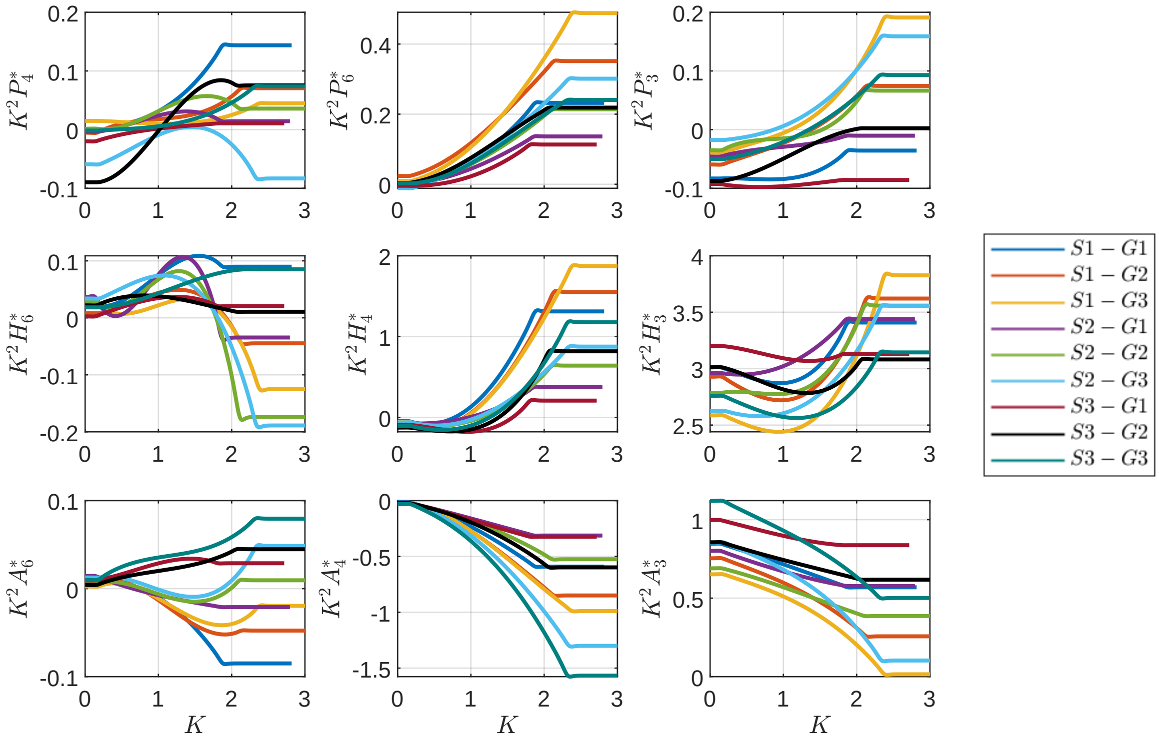

ADs related to $\hat{C}_{ae}$

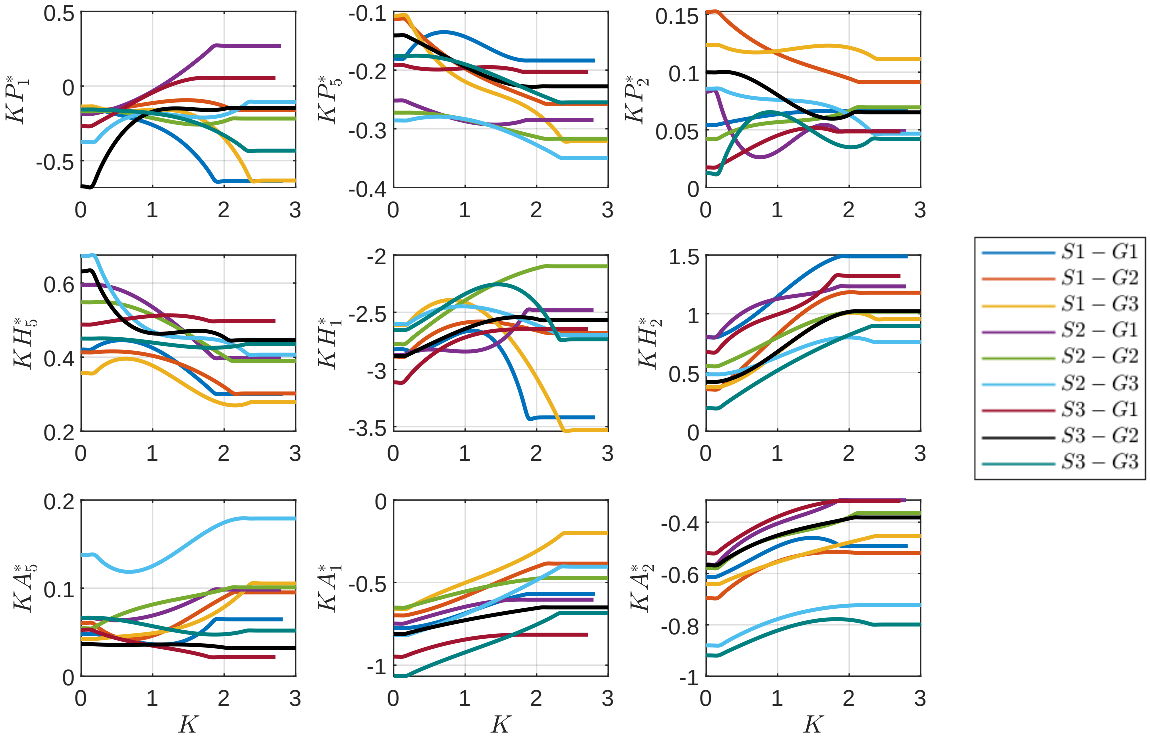

Figure 8.26: Polynomial fit for all configurations with ADs as functions of K

8.5 Predicted Stability Limits

To estimate the stability limit, multi-mode flutter analysis that accounts for the coupling effect of several vibration modes is performed. The instability condition is identified by finding the solution giving a singular impedance matrix. An increasing sequence of in-wind velocities is introduced until the in-wind velocity equates the critical wind velocity within a certain accuracy. The multi-mode flutter analysis approach is deliberated in Section 3.5.

Flutter analysis is based on modal superpositioning, which introduces the vibration mode shapes as generalized coordinates. The number of modes to include depend on whether the stability limit changes. For the flutter analyses, an adequate number of 50 modes are considered as the contribution from higher-order modes does not change the estimated stability limits.

In Figure 8.27, the still-air vibration modes which contribute to the instability phenomena are displayed by plotting the absolute value of the eigenvector. The lowest critical velocity is often provided by combining the fundamental vertical and torsional modes (Trein and Shirato, 2011). However, in the multi-mode flutter analysis of the Hardanger Bridge, three vibrations modes were found to contribute significantly (Øiseth et al., 2010). The latter also applies to the Sulafjord bridge crossing. Common for all configurations is the main contributions from three vibration modes. The flutter instability phenomenon is indicated by the strong influence from the two first vertical symmetric modes (V2 and V3) and the first torsional symmetric mode (T1).

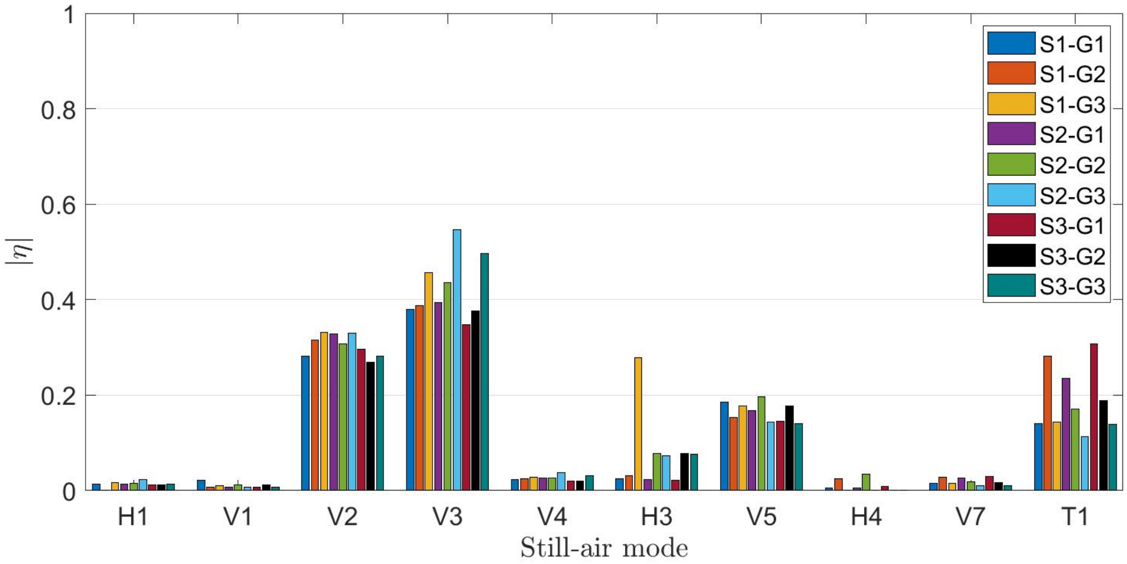

Figure 8.27: Modes contributing to the instability phenomena

The stability limits for a selection of vibration mode combinations are presented in Table 8.2. For the combination of modes V2, V3 and T1, the stability limits converge. Minor changes of maximum 1.3% in the stability limits are observed by adding contributing vertical and horizontal modes of higher order. The converging stability limits for the three vibration modes indicate that the governing instability phenomenon is multi-modal coupled flutter for all configurations.

Table 8.2: Stability limits for selected vibration modes

	V_{cr} [ms^{-1}]								
Mode combination	S1-G1	S1-G2	S1-G3	S2-G1	S2-G2	S2-G3	S3-G1	S3-G2	S3-G3
1-50	94.8	97.6	105.5	95.2	100.5	102.0	81.6	89.9	83.7
V2, T1	127.9	124.6	>130	127.6	127.1	>130	107.4	109.9	103.4
V3, T1	119.3	117.4	125.7	118.0	117.4	>130	98.7	101.2	97.6
V2, V3, T1	105.5	103.4	105.5	104.9	105.2	100.5	87.6	91.2	86.0
V2, V3, V5, T1	104.5	102.9	105.7	103.8	104.5	101.6	86.5	90.4	87.1
V2, V4, V5, V7, T1	104.5	103.0	105.7	103.8	104.6	101.8	86.6	90.5	87.1
H1, V2, V4, V5, V7, T1	104.5	102.9	105.7	103.7	104.5	101.5	86.5	90.4	87.1

To better understand the instability behaviour, the research is narrowed down to consider the modes with the main contribution to the flutter phenomenon: V2, V3 and T1. In Figure 8.28, the stability limits of the three-mode flutter phenomenon are plotted against the gap to depth ratio. The blue, red and green data points represent the configurations of S1, S2 and S3, respectively. While the orange solid line represents the stability criterion of the Norwegian bridge design code - N400 (Statens vegvesen, 2015). The calculation of the stability criterion at the location of the the Sulafjord bridge crossing is provided in Chapter 2. It is noticeable that the configurations have stability limits above the stability criterion. Thus indicating that all configurations pass the instability control of N400. The configurations of S1 and S2 exhibit superior stability behaviour compared to S3. In Figure 8.28, a 2nd order polynomial fit is implemented as a dashed line between the data points of each girder shape to observe the change in stability limit with altering gap. The central slot concept improves the flutter stability by reducing the pressure difference between the upper and lower surfaces of the bridge deck. Evident in Figure 8.28 is a general tendency of increasing stability limit with gap. The configurations S1-G2, S2-G3 and S3-G3 oppose the trend, which may be reasoned by the inaccuracies in the polynomial fits of the ADs.

The ADs characterize the self-excited forces acting on the bridge and are be obtained from forced vibration tests. The imposed oscillation is repeated for 8 frequencies and 2 wind speeds, which provides a total of 16 data points for each degree of freedom. Lastly, a 3rd order polynomial is adapted to the measured data points. Reliable estimates of the ADs are crucial in the assessment of the flutter phenomena. The uncertainties of the approximated ADs relates to the quantity and scatter of data points acquired from the wind tunnel tests. Adapting a linear or quadratic model to a non-linear or non-quadratic scatter plot may also introduce significant errors. However, only the approximation of the AD at the critical reduced frequency will influence the critical wind velocity. Securing a good approximation in the reduced frequency regime associated with the stability limit may improve the estimation of the instability behaviour. In Table 8.3, the reduced frequencies of the three-mode flutter phenomenon are noted. All the reduced frequencies are within the reduced frequency regime of the wind tunnel tests. The reliability of the calculated stability limits is strengthened by not using extrapolated approximations of the ADs.

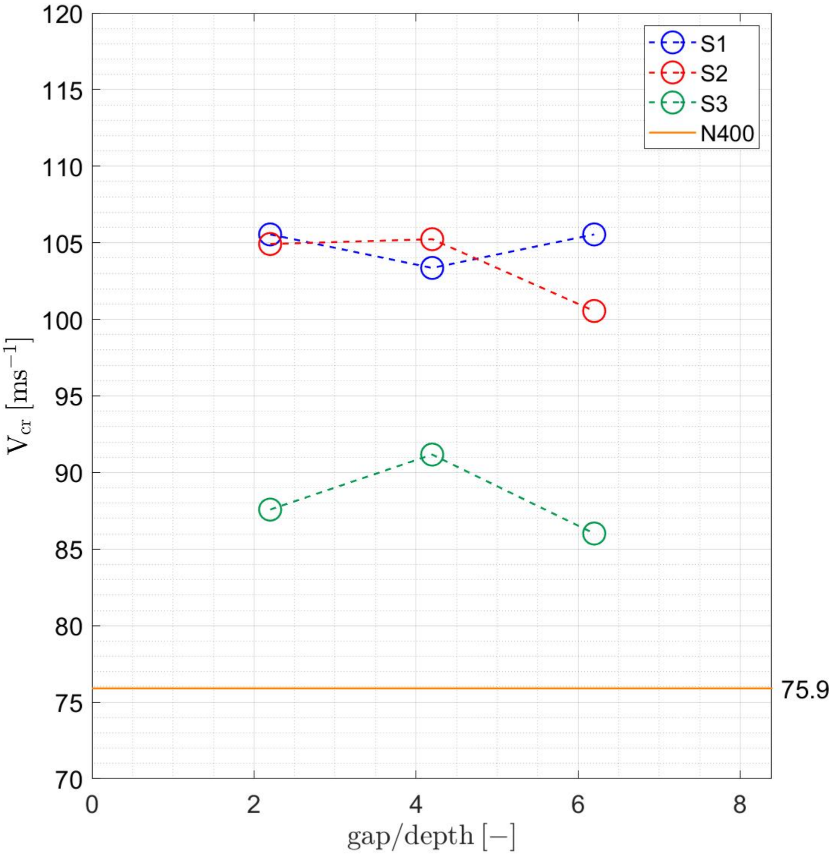

Figure 8.28: Stability limits of the three-mode flutter phenomenon

Table 8.3: Reduced frequencies of the three-mode flutter phenomenon

	K [-]		
Config.	G1	G2	G3
S1	0.378	0.403	0.423
S2	0.380	0.404	0.416
S3	0.459	0.466	0.483

To observe the importance of the ADs in calculating the stability limit, a sensitivity analysis is conducted by modifying the ADs using *sensitivityAnalysisAD.m.* The ADs H_{1-4}^* and A_{1-4}^* that represent the heaving and the pitching harmonic motions are studied. A scale factor (λ) is introduced separately to the selected ADs of S1-G1 for the mode combination of V2, V3 and T1. Table 8.4 records the percentage change in the stability limits with individually scaled ADs. The sensitivity analysis shows significant influence of the ADs: H_3^*, A_1^*, A_2^* and A_3^*. The other selected ADs appear to have a minor influence on the stability limit. Identical ADs were found significant in flutter stabilisation of the Hardanger Bridge (Øiseth et al., 2010).

Table 8.4: Percentage change in the stability limits of the three-mode flutter phenomenon of S1-G1 with separately scaled ADs

λ	H_1^*	H_2^*	H_3^*	H_4^*	A_1^*	A_2^*	A_3^*	A_4^*
0.4	-3%	-1%	136%	0%	17%	-20%	23%	3%
0.6	-2%	-1%	14%	0%	10%	-12%	14%	2%
0.8	-1%	0%	6%	0%	5%	-5%	6%	1%
1.0	0%	0%	0%	0%	0%	0%	0%	0%
1.2	2%	0%	-5%	0%	-4%	5%	-5%	-1%
1.4	4%	1%	-9%	0%	-8%	9%	-10%	-2%
1.6	6%	1%	-12%	0%	-11%	13%	-14%	-2%

At the critical reduced frequency, the approximated ADs in Figure 8.26 of significant influence can be associated with the stability limits obtained of the three-mode flutter phenomena. The higher absolute values of A_1^* and A_3^* for S3 than S1 and S2 at the critical reduced frequencies give increased vulnerability to unstable behaviour of S3. With growing values of H_3^*, the polynomial fits are displayed in the order of G3, G2 and G1. Indicating a decrease in H_3^* with increasing gap. This substantiates the theory presented of larger separation between the girders leading to improved flutter stability due to the reduction in pressure difference between the upper and lower girder surfaces (Fujino and Siringoringo, 2013). The high negative values of A_2^* for S1-G2, S2-G3 and S3-G3 at the critical reduced frequencies supports the lower stability limits obtained than expected, which break the trend of improved flutter stability with greater gap.

Flutter is an instability phenomenon that involves the introduction of self-excited forces due to flow-structure interaction. The unstable behaviour is initiated when the energy input from the wind exceeds the energy dissipated by the structure. The flutter phenomenon is investigated by considering the resulting complex eigenvalues and eigenvectors, giving the solution to the complex eigenvalue problem. To ensure bridge stability, the real part of the complex eigenvalues has to become negative, which represents positive damping.

Figure 8.29 shows the in-wind frequencies and damping ratios determined from the complex eigenvalues of configuration S1-G1. The stability limit is defined by the lowest mean wind velocity, where zero damping occurs in one of the in-wind modes. The damping ratio reaches zero for the first torsional mode, T1. However, an increase in damping ratio with the mean wind velocity is observed for the vertical modes, V2 and V3. For the larger gap, a decrease in the main contributing vertical mode is noticeable at high mean wind velocities. Evident is the loss of stiffness with increasing mean wind velocity. The twisting response of the bridge due to flutter appears to reduce the torsional stiffness. The greater proximity of the frequencies at high mean wind velocities eases the coupling effect of the vertical and torsional modes. Appendix J provides the results for the other configurations. For the S2 and S3 configurations, similar results and behaviour of the S1 configurations are obtained and observed.

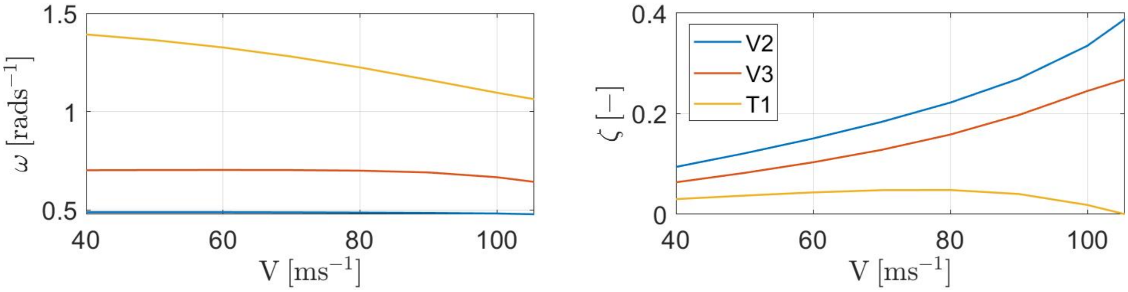

(a) S1-G1

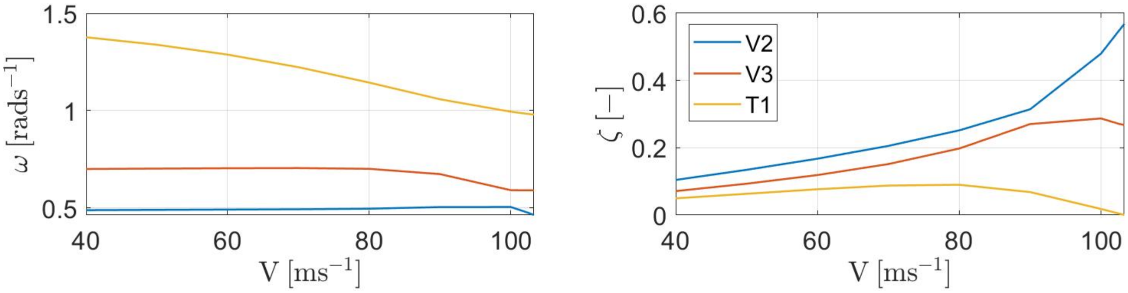

(b) S1-G2

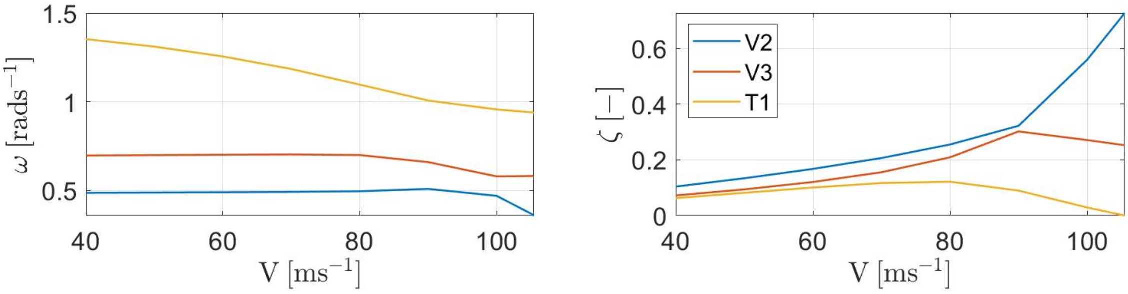

(c) S1-G3

Figure 8.29: In-wind frequencies (left) and damping ratios (right) of the three-mode flutter phenomenon of S1

The complex eigenvectors (η) considering the flutter phenomenon of the S1 configurations are plotted in Figure 8.30. The Argand diagrams show the vertical and torsional mode contributions and the phase angles between the heaving and the pitching harmonic oscillations. The contributions from vertical modes increase and torsional modes decrease with larger gap. The smaller contribution of the driving instability mode (T1) for the larger gaps may be related to the general increase in stability limit with gap. The phase angle or phase lag is indicated by the relative direction of the plotted arrows in the Argand diagrams. The phase lags of 90 degrees and 180 degrees acquired between the gap configurations represent time lags of $\frac{1}{4}$T and $\frac{1}{2}$T in the time history, respectively. Considering the configurations individually, the vertical and torsional modes couples with a phase lag, transferring energy between the air flow and vertical and torsional bridge motions. The phase lags between V2, V3 and T1 become slightly greater with larger gap. Hence, an indication of enhanced difficulty of energy transfer within the wind-structure system for larger gaps. Appendix K provides the Argand diagrams for all configurations where the configurations of S2 and S3 show similar results and behaviour as the configurations of S1.

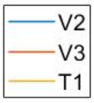

(a) Legend for Argand diagrams

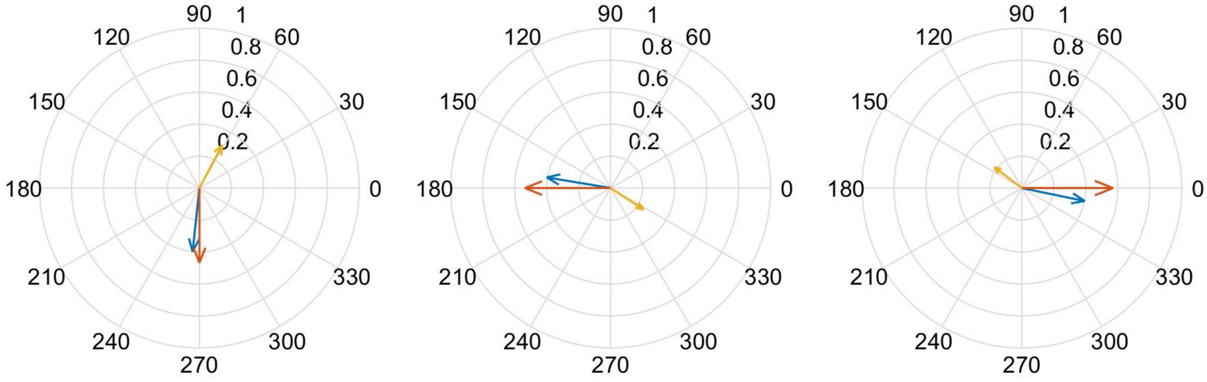

(b) S1-G1 (c) S1-G2 (d) S1-G3

Figure 8.30: Argand diagrams displaying flutter mode complexity of S1

The coupling of still-air vibration modes is further explored. Two main factors are found to impact the coupling tendency of vibration modes: (1) the separation in natural frequency and (2) the degree of shape-wise similarity of the vertical and the torsional vibration modes (Øiseth et al., 2010). Table 8.1 shows that the natural frequencies of V3 and T1 are less separated than V2 and T1 and that the still-air modes of V3 and T1 have a stronger resemblance than V2 and T1. As seen in Table 8.2, the two factors yield a lower critical velocity of mode combinations V3 and T1 than V2 and T1, consistent with the hypothesis presented.

Figure 8.31 shows the separation in natural frequency of the vertical modes (V2 and V3) and the torsional mode (T1) for variations in the gap at zero mean wind velocity. Evident is the greater proximity between the natural frequencies of the vertical vibration modes and the torsional vibration mode with increasing gap. For the majority of the configurations, increases in the critical velocity with larger gaps are observed. Suggesting that the closely spaced natural frequencies for larger gaps may improve the predicted stability limit.

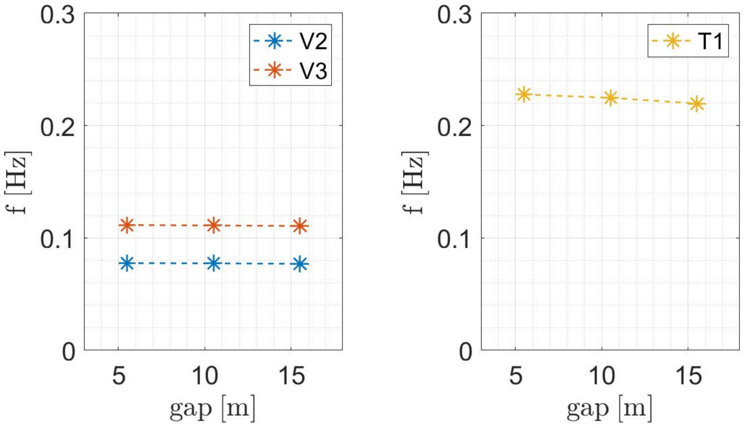

(a) Vertical modes (b) Torsional modes

Figure 8.31: Natural frequencies of the three-mode flutter phenomenon at V=0 ms^{-1}

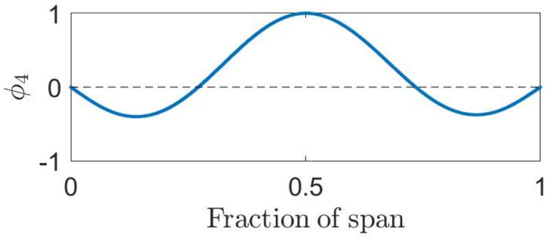

(a) Vertical mode shape of V2

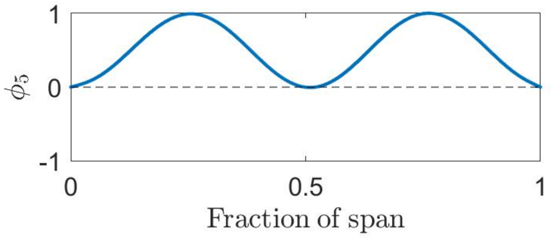

(b) Vertical mode shape of V3

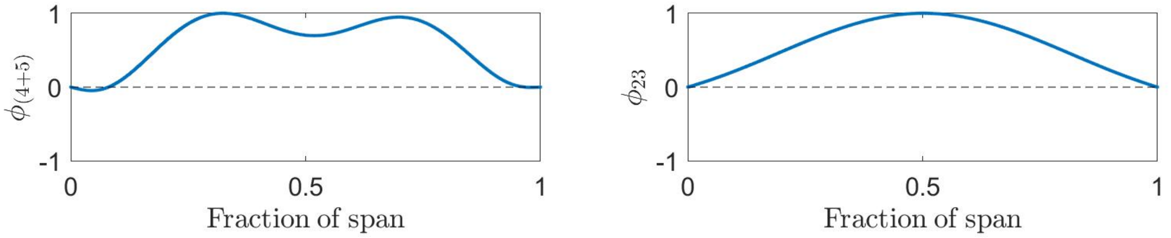

(c) Vertical mode shape of V2 and V3 (d) Torsional mode shape of T1

Figure 8.32: Mode shapes of the three-mode flutter phenomenon

Flutter instability will not occur for a combination of diverse vibration mode shapes. Therefore the shape-wise similarity is a measure to evaluate the possibility of multi-mode effects. Illustrations of the flutter vibration mode are provided in Figure 8.32 to observe the shape-wise similarity. The still-air vibration modes for V2, V3, sum of V2 and V3 and T1 are displayed. Noticeable is the shape-wise similarity between the sum of the vertical modes and the torsional mode in the three-mode coupled flutter phenomenon.

The mode shape similarity factor (ψ) can be used to estimate the degree of shape-wise similarity. For perfect shape-wise similarity, the mode shape similarity factor will equal 1. As seen in Equation 8.3, a strong shape-wise similarity is obtained for the coupling of the vertical modes V2 and V3 and the torsional mode T1. The mode shape integrals in Equations 8.1 and 8.2 confirm that the still-air mode shapes of V3 and T1 have greater similarity than V2 and T1.

$$\psi_{4,23} = \frac{\int \phi_4 \phi_{23} dx}{\int \phi_4^2 dx} \frac{\int \phi_4 \phi_{23} dx}{\int \phi_{23}^2 dx} = 0.43 \tag{8.1}$$

$$\psi_{5,23} = \frac{\int \phi_5 \phi_{23} dx}{\int \phi_5^2 dx} \frac{\int \phi_5 \phi_{23} dx}{\int \phi_{23}^2 dx} = 0.54 \tag{8.2}$$

$$\psi_{(4+5),23} = \frac{\int \phi_{(4+5)} \phi_{23} dx}{\int \phi_{(4+5)}^2 dx} \frac{\int \phi_{(4+5)} \phi_{23} dx}{\int \phi_{23}^2 dx} = 0.94 \tag{8.3}$$

8.6 Limitations of Results

The sources of error are divided into sections considering the inaccuracies of the FE-model, the errors related to the section models and the wind tunnel tests and limitations of the processing of the results. The inaccuracies of the global element models are listed as follows.

- The retraction force applied to the top of the towers is neglected, resulting in an inward lean of the towers. The simplification has minor impact on the flutter analysis.
- The iteration procedure executed in Abaqus to account for the displacement due to self-weight is within margins of 0.1 m from the final construction geometry.
- The boundary conditions and interactions are idealised. E.g. the ties between the cables and the hangers are modelled as fixed connections promoting excessive vibrations in hangers and cables. The true behaviour of the bridge may better be represented by connections between the girders and the hangers that allow for rotation.
- Identical configuration of hangers as the Langenuen Bridge with 24 m of separation of the hangers. In the feasibility study by Multiconsult, a 20 m separation of the hangers is specified.
- Conservative choices are made for the properties of the girder, cables, hangers, pylons and portal beams.

The errors related to the section models and wind tunnel effects include

- The dimensions, positioning, finish and material properties of the section models and attachments can affect the results from the wind tunnel tests.

- The influence of the boundary layer in proximity to the wind tunnel walls is minor considering the boundary layer thickness against the span of the section model. Therefore, a uniform velocity profile is assumed.
- With a blockage ratio of 2.5%, no considerations are made for the blockage effect (Lee et al., 2014).
- The gap between the section model and the wind tunnel walls measure 3 cm. End plates are not used as the section model almost spans entirely across the width of the wind tunnel. The flow in the wind tunnel is considered two-dimensional.
- The pitot probe is positioned with sufficient distance from the section model such that it does not affect the flow induced on the section model.

The following limitations of the processed results from the global element models and the wind tunnel tests are considered.

- The quality of the data depends on the execution of the wind tunnel tests and the sampling frequency. The sampling frequency is the number of data points acquired per second, which defines the precision of the recorded data.
- Conservative density assumptions are made. In the wind tunnel, air density fluctuations of 1.18-1.19 kgm^{-3} are recorded. The air density of 1.2 kgm^{-3} is used in the data processing. For the location of the bridge crossing of the Sulafjord, the theoretical density of 1.25 kgm^{-3} is implemented (Statens vegvesen, 2015).
- The evaluated damping ratio from the logarithmic decrements is sensitive to the selection of points and the duration of the damped free vibration time series. Due to the beating phenomenon, the envelope is not representative of the true damping. The damping ratio from the Norwegian bridge design code of $\zeta = 0.2\%$ (Statens vegvesen, 2015) may deviate from the bridge crossing the Sulafjord. The estimations of the damping ratio are considered acceptable for conducted assessment of VIV performance.
- It is assumed a locally stationary and homogeneous wind field acting on the bridge, considered as a line-like structure. The wind speed is assumed to be assessed in terms of a time-invariant mean part and a randomly fluctuating component.
- The predicted stability limits is to a great extent affected by the flutter derivatives. Significant uncertainties in ADs relate to the number and scatter of data points acquired from the forced vibration tests in addition to the fit of the polynomial curve. Approximations of ADs at the critical reduced frequency are within the frequency regime of the wind tunnel tests, strengthening the reliability of the calculated stability limits.

Chapter 9

Conclusions

Sufficient aerodynamic stability limits are found for the twin-deck configurations of a suspension bridge crossing the Sulafjord. The wind-structure interaction is explored for nine twin-deck configurations of different shapes and gaps. Through interpolation, a geometric relation is established yielding three girder shapes with minor amendments. The sharpness of the inner and outer fairings alter, causing changes in the angle of the fairings and the girder width. The twin-deck configurations represent the three girder shapes (S1-S3) combined with the three gaps (G1-G3). For the configurations, the aerodynamic stability and the vortex-induced oscillating behaviour is evaluated. The modal properties are extracted from global element models, while the static coefficients and aerodynamic derivatives are experimentally obtained.

The VIV and damping tests show that less severe vortex-induced oscillations and improved damping is achieved with built-in dampers. However, the TMDs are challenging to replicate in full-scale and therefore do not solve the issue of VIVs. To fulfil the serviceability requirements of the bridge, excessive vibrations shall be avoided. The configurations of S1 and smaller gaps obtain superior VIV performance in the wind tunnel. Additionally, the section models are found to exhibit larger vibrations due to vortex shedding than the equivalent full-scale bridge decks.

The analysis of the static coefficients and aerodynamic derivatives revealed negligible dependency on the Reynolds number for the nine section models. The overall static coefficients exhibited clear trends with minimal presence of non-linearity. Low presence of scatter and good polynomial fittings for most of the critical aerodynamic derivatives entails better results. Whereas, the aerodynamic derivatives that show deviating trend with increased wind speed, causes for a worse polynomial fit as well as inaccuracies concerning the stability limit calculations. Most of the critical aerodynamic derivatives achieved good estimations with a third degree polynomial fitting contributing to enhanced accuracy of the stability limits. Considering both the static coefficients and aerodynamic derivatives, the configurations of section type S3 displays a stability weakness due to evident deviations throughout the analysis.

In the computation of the stability limits, the contributions of 50 modes are found adequate. The stability limits converge for the combination of the two first vertical symmetric modes (V2 and V3) and the first torsional symmetric mode (T1). For the three-mode flutter phenomenon, the calculated stability limits ranges between $86.0\,\mathrm{ms}^{-1}$ and $105.5\,\mathrm{ms}^{-1}$. The configurations of S1 and S2 exhibit superior stability behaviour and detected is also a general tendency of increasing stability limit with larger gaps. Deviations from the stability limit trends may be due to inaccurate polynomial fits of the ADs. Crucial are reliable estimates of the ADs at the critical reduced frequency in assessment of the flutter phenomenon. The sensitivity analysis conducted shows significant influence on the stability limit of the ADs: H_3^*, A_1^*, A_2^* and A_3^*. High absolute values of A_1^* and A_3^* substantiate the more unstable behaviour of S3. With growing values of H_3^* the gap decreases, supporting the improved flutter stability with increasing gap. The high values of A_2^* may reason the lower stability limits obtained than expected for S1-G2, S2-G3 and S3-G3. However, all the configurations fulfil the stability criterion of $75.9\,\mathrm{ms}^{-1}$ determined from the Norwegian bridge design code - N400 (Statens vegvesen, 2015).

Chapter 10

Further Work

During the work of this master's thesis, several subjects of further work have been identified. The proposed work for further investigation and control of the aerodynamic performance of the twin-deck configurations is presented as follows:

- Study the effect of the section model attachments on VIV and flutter performance in the wind tunnel. The attachments of railings, guide vanes and TMD are introduced in the thesis. However, other cross-sectional details like wind barrier, grid plates and central stabilizers can be investigated. Research on the importance of cross-sectional details have been conducted by Zhou et al. (2019), Laima et al. (2018), and Yang et al. (2017).

- Repetition of the wind tunnel tests with applied wind in opposite direction to establish if the geometry of the section models entail a shift in the aerodynamic properties. S1-G2, S2-G3 and S3-G3 obtain lower stability limits than expected, which may be due to the inaccuracies of the experimentally obtained static coefficients and aerodynamic derivatives. The reliability of the flutter analyses can be assessed through Monte Carlo simulations as conducted for the Hardanger Bridge by Øiseth et al. (2015).

- The effect of turbulence should be further investigated as inflows on bridges have turbulence characteristics (Laima and Li, 2015). The wind tunnel tests are performed in smooth flow and turbulence may alter the wind-structure interaction significantly. Therefore, the buffeting behaviour of the twin-decks should be further examined.

- Further research is required to evaluate the vortex-induced response and stability behaviour of the twin-deck configurations in greater detail. For the twin-box girders, further work can involve the wind-induced pressure differences (Kwok et al., 2012), the vortex shedding behaviour (Chen et al., 2014), the Reynolds dependency of ADs (Lee et al., 2014) and the flutter performance (Nieto et al., 2020).

- Optimization of the twin-deck configurations as conducted by Cid Montoya et al. (2021). Since all twin-decks preformed well within the stability criterion, the girder design may be optimized reducing the material consumption and construction costs.

- Improvements of the global element models to obtain mathematical models more representative of true bridge behaviour. Adjustments can be made to the interactions and boundary conditions, girder geometry and properties including cross-beams etc.

Bibliography

Álvarez, A.J., Nieto, F., Kwork, K.C.S., and Hernández, S. (2018), "Aerodynamic performance of twin-box decks: A parametric study on gap width effects based on validated 2D URANS simulations", *Journal of Wind Engineering and Industrial Aerodynamics*, 182, pp. 202–221, DOI: `10.1016/j.jweia.2018.09.004`.

Brancaleoni, F. (2016), "Concepts and new perspectives for long span bridges", *Romanian Journal of Transport Infrastructure*, 5(6), pp. 75–97, DOI: `10.1515/rjti-2016-0043`.

Buckingham, E. (1914), "On Physically Similar Systems; Illustrations of the Use of Dimensional Equations", *Physical Review*, 4(4), pp. 345–376, DOI: `10.1103/PhysRev.4.345`.

Castellon, D., Fenerci, A., and Øiseth, O. (2021), "Environmental Contours for Wind-Resistant Bridge Design in Complex Terrain", *Submitted for journal publication.*

Chen, W.L., Li, H., and Hu, H. (2014), "An experimental study on the unsteady vortices and turbulent flow structures around twin-box-girder bridge deck models with different gap ratios", *Journal of Wind Engineering and Industrial Aerodynamics*, 132, pp. 27–36, DOI: `10.1016/j.jweia.2014.06.015`.

Chen, X. (2007), "Improved Understanding of Bimodal Coupled Bridge Flutter Based on Closed-Form Solutions", *Journal of Structural Engineering*, 133(1), pp. 22–31, DOI: `10.1061/(ASCE)0733-9445(2007)133:1(22)`.

Chen, X. and Kareem, A. (2002), "Advances in Modeling of Aerodynamic Forces on Bridge Decks", *Journal of Engineering Mechanics*, 128(11), pp. 1193–1205, DOI: `10.1061/(ASCE)0733-9399(2002)128:11(1193)`.

Chen, X. and Kareem, A. (2003), "Aeroelastic Analysis of Bridges: Effects of Turbulence and Aerodynamic Nonlinearities", *Journal of Engineering Mechanics*, 129(8), pp. 885–895, DOI: `10.1061/(ASCE)0733-9399(2003)129:8(885)`.

Chen, X., Kareem, A., and Matsumoto, M. (2001), "Multimode coupled flutter and buffeting analysis of long span bridges", *Journal of Wind Engineering and Industrial Aerodynamics*, 89(7-8), pp. 649–664, DOI: `10.1016/S0167-6105(01)00064-2`.

Cheynet, E., Jakobsen, J.B., and Snæbjörnsson, J. (2016), "Buffeting response of a suspension bridge in complex terrain", *Engineering Structures*, 128, pp. 474–487, DOI: `10.1016/j.engstruct.2016.09.060`.

Chopra, A.K. (2012), *Dynamics of Structures*, 4th ed, Upper Saddle River: Pearson Education, Inc.

Cid Montoya, M., Nieto, F., Hernández, S., Fontán, A., Jurado, J.A., and Kareem, A. (2021), "Optimization of bridges with short gap streamlined twin-box decks considering structural, flutter and buffeting performance", *Journal of Wind Engineering and Industrial Aerodynamics*, 208, p. 104316, DOI: `10.1016/j.jweia.2020.104316`.

Dassault Systèmes Simulia Corp. (2014), *Abaqus Scripting Reference Guide*, version 6.14.

Dassault Systèmes Simulia Corp. (2020), *Solidworks*, version 2020, URL: `https://www.solidworks.com/`, [Accessed: 1. April 2021].

Davenport, A.G. (1962), “The Response of Slender, Line-Like Structures to a Gusty Wind”, *Proceedings of the Institution of Civil Engineers*, 23(3), pp. 389–408, DOI: `https://doi.org/10.1680/iicep.1962.10876`.

Diana, G., Resta, F, and Rocchi, D. (2008), “A new numerical approach to reproduce bridge aerodynamic non-linearities in time domain”, *Journal of Wind Engineering and Industrial Aerodynamics*, 96(10-11), pp. 1871–1884, DOI: `10.1016/j.jweia.2008.02.052`.

Dombu, M.V. and Gjelstad, M. (2019), “Parametric modelling of a suspension bridge with an aluminium girder”, MA thesis, Høgskoleringen 1, 7491 Trondheim: Norwegian University of Science and Technology.

Fenerci, A., Øiseth, O., and Rønnquist, A. (2017), “Long-term monitoring of wind field characteristics and dynamic response of a long-span suspension bridge in complex terrain”, *Engineering Structures*, 147, pp. 269–284, DOI: `10.1016/j.engstruct.2017.05.070`.

Frandsen, J.B. (2004), “Numerical bridge deck studies using finite elements. Part I: flutter”, *Journal of Fluids and Structures*, 19, pp. 171–191, DOI: `10.1016/j.jfluidstructs.2003.12.005`.

Fujino, Y. and Siringoringo, D. (2013), “Vibration Mechanisms and Controls of Long-Span Bridges: A Review”, *Structural Engineering International*, 23(3), pp. 248–268, DOI: `10.2749/101686613X13439149156886`.

Generate Directorate of Highways (2020), *1915Çanakkale*, URL: `https://www.1915canakkale.com/en-us`, [Accessed: 23. February 2021].

Gimsing, N.J. and Georgakis, C.T. (2012), *Cable Supported Bridges: Concept and Design*, 3rd ed, Chichester: John Wiley & Sons, Ltd.

Giske, F. and Midtgarden, E. (2018), “Parametric Design and Gradient-Free Optimization of Super Long-Span Suspension Bridges”, MA thesis, Høgskoleringen 1, 7491 Trondhiem: Norwegian University of Science and Technology.

Grongstad, J.R. and Kildal, O. (2018), “Wind tunnel testing of bridge decks”, MA thesis, Høgskoleringen 1, 7491 Trondheim: Norwegian University of Science and Technology.

Han, Y., Liu, S., Hu, J.X., Cai, C.S., Zhang, J., and Chen, Z. (2014), “Experimental study on aerodynamic derivatives of a bridge cross-section under different traffic flows”, *Journal of Wind Engineering and Industrial Aerodynamics*, 133, pp. 250–262, DOI: `10.1016/j.jweia.2014.08.003`.

Hu, L., Hu, Y.L., and Huang, W.F. (2013), “Typhoon-induced non-stationary buffeting response of long-span bridges in complex terrain”, *Engineering Structures*, 57, DOI: `10.1016/j.engstruct.2013.09.044`.

Jain, A., Jones, N.O., and Scalan, R. H. (1996), “Coupled flutter and buffeting analysis of long-span bridges”, *Journal of Structural Engineering*, 122(7), pp. 716–725, DOI: `10.1061/(ASCE)0733-9445(1996)122:7(716)`.

Kjeller Vindteknikk (2019), *Analysis of wind measurements from 6 masts at Sulafjorden 24.11.2016 - 30.09.2019*, tech. rep. RAP-KVT-L-104-R0 / KVT/ASH/2019/R136.

Kwok, K.C.S., Qin, X.R., Fok, C.H., and Hitchcock, P.A. (2012), “Wind-induced pressures around a sectional twin-deck bridge model: Effects of gap-width on the aerodynamic forces and vortex shedding mechanisms”, *Journal of Wind Engineering and Industrial Aerodynamics*, 110, pp. 50–61, DOI: `10.1016/j.jweia.2012.07.010`.

Laima, S. and Li, H. (2015), “Effects of gap width on flow motions around twin-box girders and vortex-induced vibrations”, *Journal of Wind Engineering and Industrial Aerodynamics*, 139, pp. 37–49, DOI: `10.1016/j.jweia.2015.01.009`.

Laima, S., Li, H., Chen, W., and Ou, J. (2018), “Effects of attachments on aerodynamic characteristics and vortex-induced vibration of twin-box girder”, *Journal of Fluid and Structures*, 77, pp. 115–133, DOI: `10.1016/j.jfluidstructs.2017.12.005`.

Larose, G.L. and D'Auteuil, A. (2006), "On the Reynolds number sensitivity of the aerodynamics of bluff bodies with sharp edges", *Journal of Wind Engineering and Industrial Aerodynamics*, 94(5), pp. 365–376, DOI: `10.1016/j.jweia.2006.01.011`.

Larsen, A., Esdahl, S., Andresen, J.E., and Vejrum, T. (2000), "Storebælt suspension bridge - vortex shedding excitation and mitigation by guide vanes", *Journal of Wind Engineering and Industrial Aerodynamics*, 88, pp. 283–296, DOI: `10.1016/S0167-6105(00)00054-4`.

Larsen, A., Savage, M., Lafrenière, A., Hui, M.C.H., and Larsen, S.V. (2008), "Investigation of vortex response of a twin box bridge section at high and low Reynolds numbers", *Journal of Wind Engineering and Industrial Aerodynamics*, pp. 934–944, DOI: `10.1016/j.jweia.2007.06.020`.

Lee, S., Kwon, S.D., and Yoon, J. (2014), "Reynolds number sensitivity to aerodynamic forces of twin box bridge girder", *Journal of Wind Engineering and Industrial Aerodynamics*, 127, pp. 59–68, DOI: `10.1016/j.jweia.2014.02.004`.

Lystad, T.M., Fenerci, A., and Øiseth, O. (2018), "Evaluation of mast measurements and wind tunnel terrain models to describe spatially variable wind field characteristics for long-span bridge design", *Journal of Wind Engineering and Industrial Aerodynamics*, 179, pp. 558–573, DOI: `10.1016/j.jweia.2018.06.021`.

Multiconsult (2015), *Suspension bridge alternative - Sulafjorden*, tech. rep.

Nieto, F., Cid Montoya, M., Hernández, S., Kusano, I., Casteleiro, A., Álvarez, A.J., Jurado, J.Á., and Fontán, A. (2020), "Aerodynamic and aeroelastic responses of short gap twin-box decks: Box geometry and gap distance dependent surrogate based design", *Journal of Wind Engineering and Industrial Aerodynamics*, 201, p. 104147, DOI: `10.1016/j.jweia.2020.104147`.

Norwegian Public Roads Administration (2020), *Ferjefri E39*, URL: `https://www.vegvesen.no/vegprosjekter/ferjefriE39`, [Accessed: 18. February 2021].

Rambøll (2015), *Concept Study - Sulafjorden*, tech. rep.

Sato, H., Hirahara, N., Fumoto, K., Hirano, S., and Kusuhara, S. (2002), "Full aeroelastic model test of a super long-span bridge with slotted box girder", *Journal of Wind Engineering and Industrial Aerodynamics*, 90, pp. 2023–2032, DOI: `10.1016/S0167-6105(02)00318-5`.

Scanlan, R.H. and Tomko, J.J. (1971), "Airfoil and Bridge Deck Flutter Derivatives", *Journal of the Engineering Mechanics Division*, 97(6), pp. 1717–1737, DOI: `10.1061/JMCEA3.0001526`.

Siedziako, B. and Øiseth, O. (2017a), "A new experimental approach to validation of aerodynamic derivatives based model for self-excited forces", *9th Asia-Pacific Conference on Wind Engineering.*

Siedziako, B. and Øiseth, O. (2017b), "On the importance of cross-sectional details in the wind tunnel testing of bridge deck section models", *Procedia Engineering*, 199, pp. 3145–3151, DOI: `10.1016/j.proeng.2017.09.573`.

Siedziako, B., Øiseth, O., and Rønnquist, A. (2017), "An enhanced forced vibration rig for wind tunnel testing of bridge deck section models in arbitrary motion", *Journal of Wind Engineering and Industrial Aerodynamics*, 164, pp. 152–163, DOI: `10.1016/j.jweia.2017.02.011`.

Statens vegvesen (2011), *Teknisk brosjyre Hardangerbrua*, URL: `https://www.vegvesen.no/vegprosjekter/Hardangerbrua`, [Accessed: 30. March 2021].

Statens vegvesen (2015), *Håndbok N400 - Bruprosjektering.*

Strømmen, E. (2010), *Theory of Bridge Aerodynamics*, 2nd ed, Berlin: Springer.

Tamura, Y. and Kareem, A. (2013), *Advanced Structural Wind Engineering*, Tokyo: Springer.

Theodorsen, T. (1949), *General Theory of Aerodynamic Instability and the Mechanism of Flutter*, Washington: National Advisory Committee for Aeronautics.

Trein, C.A. and Shirato, H. (2011), "Coupled flutter stability from the unsteady pressure characteristics point of view", *Journal of Wind Engineering and Industrial Aerodynamics*, 99(2), pp. 114–122, DOI: `10.1016/j.jweia.2010.12.003`.

Wang, Q., Liao, H., Li, M., and Ma, C. (2011), "Influence of aerodynamic configuration of a streamline box girder on bridge flutter and vortex-induced vibration", *Journal of Modern Transportation*, 19, pp. 261–267, DOI: `10.1007/BF03325767`.

Yang, Y., Zhou, R., Ge, Y., Mohotti, D., and Mendis, P. (2015), "Aerodynamic instability performance of twin box girders for long-span bridges", *Journal of Wind Engineering and Industrial Aerodynamics*, 145, pp. 196–208, DOI: `10.1016/j.jweia.2015.06.014`.

Yang, Y., Zhou, R., Ge, Y., and Zhang, L. (2016), "Experimental studies on VIV performance and countermeasures for twin-box girder bridges with various slot width ratios", *Journal of Fluids and Structures*, 66, pp. 476–489, DOI: `10.1016/j.jfluidstructs.2016.08.010`.

Yang, Y., Zhou, R., Ge, Z., Zou, X., and Zhang, L. (2017), "Flutter characteristics of twin-box girder bridges with vertical central stabilizers", *Engineering Structures*, 133, pp. 33–48, DOI: `10.1016/j.engstruct.2016.12.009`.

Zhou, R., Ge, Y., Yang, Y., Du, Y., Liu, S., and Zhang, L. (2019), "Nonlinear behaviors of the flutter occurrences for a twin-box girder bridge with passive countermeasures", *Journal of Sound and Vibration*, 447, pp. 221–235, DOI: `10.1016/j.jsv.2019.02.002`.

Zhu, L.D. and Xu, Y.L. (2005), "Buffeting response of long-span cable-supported bridges under skew winds. Part 1: Theory", *Journal of Sound and Vibration*, 281(3-5), pp. 647–673, DOI: `10.1016/j.jsv.2004.01.026`.

Øiseth, O., Rönnquist, A., and Naess, A. (2015), "System Reliability of Suspension Bridges Considering Static Divergence and Flutter", *12th International Conference on Applications of Statistics and Probability in Civil Engineering, ICASP12.*

Øiseth, O., Rönnquist, A., and Sigbjörnsson, R. (2010), "Simplified prediction of wind-induced response and stability limit of slender long-span suspension bridges, based on modified quasi-steady theory: A case study", *Journal of Wind Engineering and Industrial Aerodynamics*, 98(12), pp. 730–741, DOI: `10.1016/j.jweia.2010.06.009`.

Appendices

Appendix A

List of Electronic Attachments

Python scripts:

- *Sulafjorden_TD21_S1G1.py*
- *AbaqusExportModal.py*

Matlab scripts:

- *importAbaqusResults.m*
- *modalProperties.m*
- *VIV.m*
- *strouhalNumber.m*
- *damping.m*
- *scrutonNumber.m*
- *staticCoeffAllTests.m*
- *aerodynamicDerivativesAllTests.m*
- *flutterAnalysis.m*
- *stabilityLimits.m*
- *sensitivityAnalysisAD.m*

Appendix B

Detailed Girder Geometries

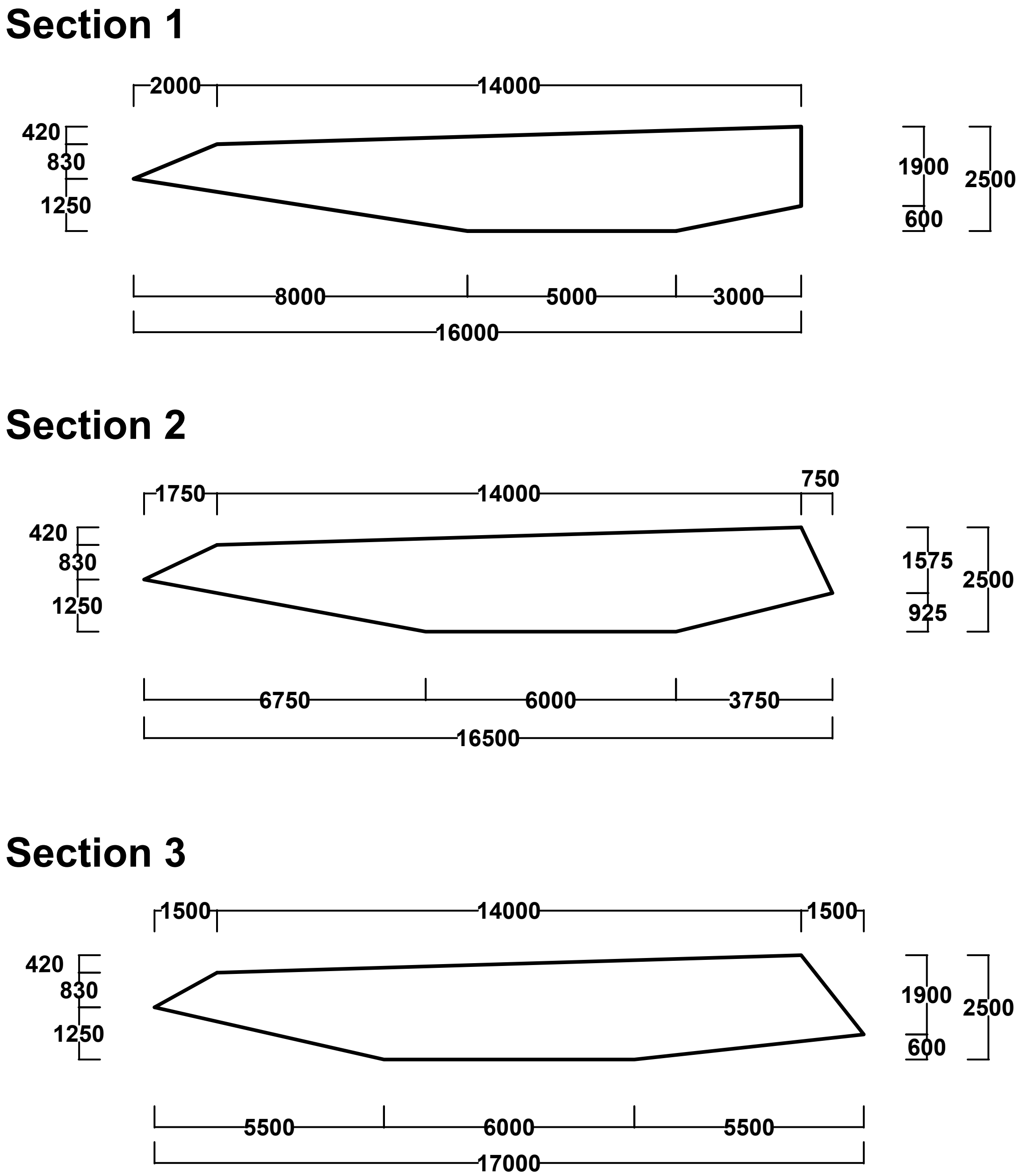

Section 1

Section 2

Section 3

Figure B.1: Detailed layout of section types with dimensions in 1:1 scale.

Section 1

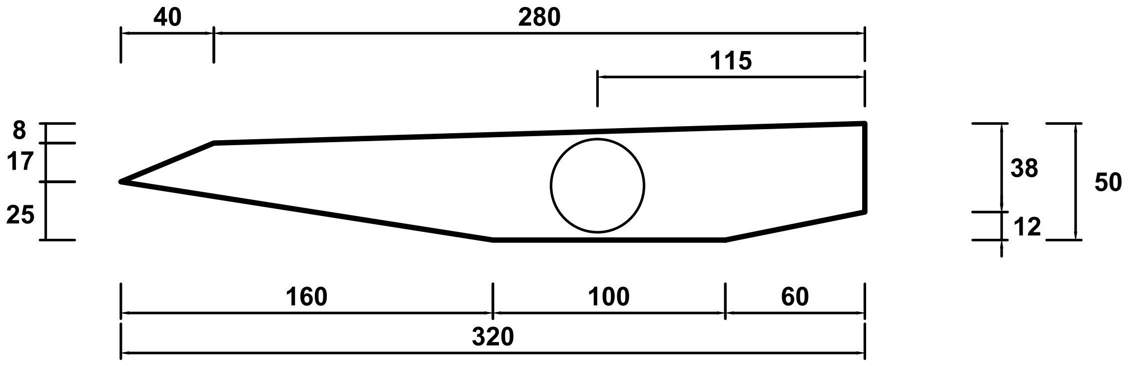

Section 2

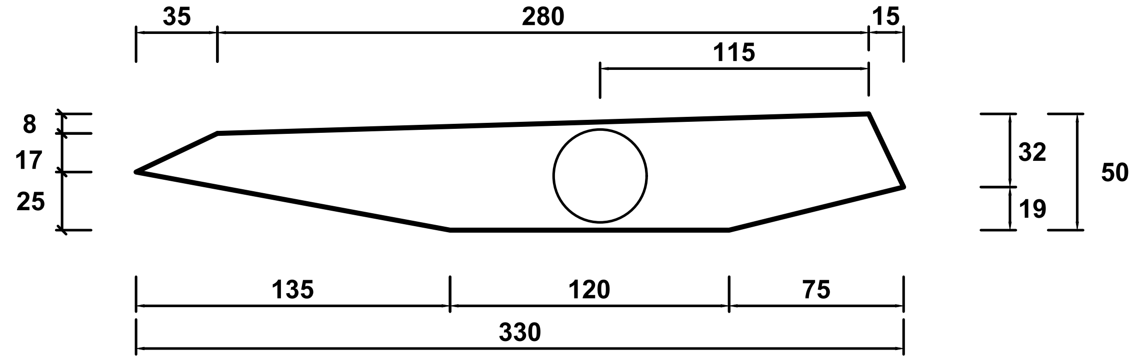

Section 3

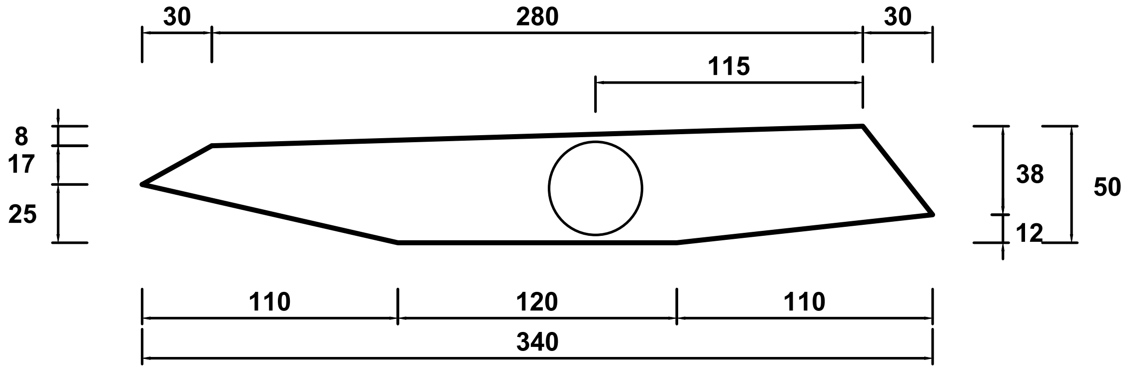

Figure B.2: Detailed layout of section types with aluminium pipe and dimensions in 1:50.

Appendix C

Added Girder Inertia

The added girder inertia is presented for S1, S2 and S3 in Table C.1, Table C.2 and Table C.3, respectively. The Local 1-coordinate to the center of mass e_1 has opposing signs for girder 1 and girder 2 as the local coordinate axes 1 and 2 are defined in the direction of the global negative y and positive z, respectively.

Table C.1: Added girder inertia for S1

Component	Gap	Linear mass [kg/m]	e_1 [m]	e_2 [m]	I_{11} [kgm^2/m]	I_{22} [kgm^2/m]
Girder	$\forall$	6045.550	0.000	0.000	5542.885	143 309.600
Diaphgrama	$\forall$	562.119	0.000	0.000	201.824	9034.565
Asphalt	$\forall$	2800.000	∓2.234	1.287	1.493	45 733.333
Hanger heads	$\forall$	33.333	∓9.234	1.047	0.025	0.025
Cross-beams	G1	191.125	±6.141	0.000	240.794	120.449
	G2	364.875	±7.391	0.000	459.697	838.072
	G3	538.625	±8.641	0.000	678.601	2695.929

Table C.2: Added girder inertia for S2

Component	Gap	Linear mass [kg/m]	e_1 [m]	e_2 [m]	I_{11} [kgm^2/m]	I_{22} [kgm^2/m]
Girder	$\forall$	6078.510	0.000	0.000	5670.055	146 127.750
Diaphgrama	$\forall$	589.339	0.000	0.000	220.036	9756.765
Asphalt	$\forall$	2800.000	∓1.831	1.286	1.493	45 733.333
Hanger heads	$\forall$	33.333	∓8.831	1.061	0.025	0.025
Cross-beams	G1	191.125	±7.294	0.000	240.794	120.449
	G2	364.875	±8.544	0.000	459.697	838.072
	G3	538.625	±9.794	0.000	678.601	2695.929

Table C.3: Added girder inertia for S3

Component	Gap	Linear mass [kg/m]	e_1 [m]	e_2 [m]	I_{11} [kgm^2/m]	I_{22} [kgm^2/m]
Girder	$\forall$	6237.380	0.000	0.000	6029.350	157 698.650
Diaphgrama	$\forall$	618.384	0.000	0.000	234.126	10 894.230
Asphalt	$\forall$	2800.000	∓1.595	1.239	1.493	45 733.333
Hanger heads	$\forall$	33.333	∓8.595	1.021	0.025	0.025
Cross-beams	G1	191.125	±8.280	0.000	240.794	120.449
	G2	364.875	±9.530	0.000	459.697	838.072
	G3	538.625	±10.780	0.000	678.601	2695.929

Appendix D

Linear Mass of Section Models

Table D.1: Linear mass of section models

	m [kgm^{-1}]		
Config.	S1	S2	S3
$\forall$	2.15	2.13	2.20

Appendix E

Modal Properties

Table E.1: Modal properties for S1

	S1-G1			S1-G2			S1-G3		
Name	f	$\tilde{\mathrm{M}}$	$\tilde{\mathrm{K}}$	f	$\tilde{\mathrm{M}}$	$\tilde{\mathrm{K}}$	f	$\tilde{\mathrm{M}}$	$\tilde{\mathrm{K}}$
	[Hz]	[kg]	[Nm^{-1}]	[Hz]	[kg]	[Nm^{-1}]	[Hz]	[kg]	[Nm^{-1}]
H1	0.031	3.847×10^7	1.419×10^6	0.032	3.805×10^7	1.564×10^6	0.034	3.799×10^7	1.744×10^6
H2	0.064	3.054×10^7	5.014×10^6	0.072	3.170×10^7	6.465×10^6	0.080	3.320×10^7	8.311×10^6
V1	0.065	4.227×10^7	6.957×10^6	0.065	4.271×10^7	7.020×10^6	0.064	4.316×10^7	7.083×10^6
V2	0.078	2.189×10^7	5.212×10^6	0.077	2.213×10^7	5.242×10^6	0.077	2.236×10^7	5.272×10^6
V3	0.112	3.298×10^7	1.626×10^7	0.111	3.334×10^7	1.632×10^7	0.111	3.371×10^7	1.639×10^7
V4	0.114	3.794×10^7	1.951×10^7	0.114	3.856×10^7	1.973×10^7	0.114	3.916×10^7	1.995×10^7
H3	0.118	2.583×10^7	1.419×10^7	0.133	2.662×10^7	1.872×10^7	0.149	3.038×10^7	2.672×10^7
V5	0.146	3.496×10^7	2.954×10^7	0.146	3.538×10^7	2.974×10^7	0.146	3.581×10^7	2.994×10^7
V6	0.174	4.123×10^7	4.915×10^7	0.173	4.158×10^7	4.929×10^7	0.173	4.193×10^7	4.943×10^7
H4	0.205	3.897×10^7	6.462×10^7	0.223	2.503×10^7	4.934×10^7	0.279	3.303×10^7	1.015×10^8
V7	0.205	3.782×10^7	6.278×10^7	0.204	3.838×10^7	6.332×10^7	0.204	3.916×10^7	6.425×10^7
T1	0.228	2.760×10^7	5.678×10^7	0.226	2.663×10^7	5.380×10^7	0.222	2.968×10^7	5.756×10^7
V8	0.235	3.993×10^7	8.741×10^7	0.235	3.995×10^7	8.687×10^7	0.234	4.005×10^7	8.652×10^7
V9	0.269	3.585×10^7	1.023×10^8	0.268	3.641×10^7	1.031×10^8	0.267	3.757×10^7	1.057×10^8
T2	0.286	2.388×10^7	7.705×10^7	0.300	2.786×10^7	9.927×10^7	0.312	3.251×10^7	1.248×10^8
V10	0.302	3.502×10^7	1.264×10^8	0.301	3.523×10^7	1.261×10^8	0.300	3.544×10^7	1.258×10^8
V11	0.338	3.348×10^7	1.508×10^8	0.336	3.368×10^7	1.504×10^8	0.335	3.389×10^7	1.500×10^8
H5	0.339	2.740×10^7	1.243×10^8	0.367	3.443×10^7	1.835×10^8	0.422	3.045×10^7	2.143×10^8
V12	0.375	3.342×10^7	1.852×10^8	0.373	3.360×10^7	1.845×10^8	0.371	3.379×10^7	1.838×10^8
V13	0.414	3.223×10^7	2.179×10^8	0.412	3.244×10^7	2.171×10^8	0.410	3.265×10^7	2.164×10^8

Table E.2: Modal properties for S2

	S2-G1			S2-G2			S2-G3		
Name	f [Hz]	$\tilde{\mathrm{M}}$ [kg]	$\tilde{\mathrm{K}}$ [Nm^{-1}]	f [Hz]	$\tilde{\mathrm{M}}$ [kg]	$\tilde{\mathrm{K}}$ [Nm^{-1}]	f [Hz]	$\tilde{\mathrm{M}}$ [kg]	$\tilde{\mathrm{K}}$ [Nm^{-1}]
H1	0.031	3.846×10^7	1.443×10^6	0.033	3.811×10^7	1.592×10^6	0.034	3.836×10^7	1.735×10^6
H2	0.066	3.079×10^7	5.226×10^6	0.073	3.199×10^7	6.734×10^6	0.080	3.345×10^7	8.360×10^6
V1	0.065	4.242×10^7	6.983×10^6	0.065	4.287×10^7	7.045×10^6	0.064	4.330×10^7	7.061×10^6
V2	0.078	2.197×10^7	5.226×10^6	0.077	2.221×10^7	5.255×10^6	0.077	2.246×10^7	5.250×10^6
V3	0.112	3.312×10^7	1.629×10^7	0.111	3.348×10^7	1.635×10^7	0.111	3.375×10^7	1.633×10^7
V4	0.114	3.819×10^7	1.962×10^7	0.114	3.879×10^7	1.984×10^7	0.113	3.904×10^7	1.970×10^7
H3	0.120	2.597×10^7	1.482×10^7	0.136	2.838×10^7	2.062×10^7	0.150	3.121×10^7	2.765×10^7
V5	0.146	3.511×10^7	2.963×10^7	0.146	3.554×10^7	2.983×10^7	0.145	3.589×10^7	2.973×10^7
V6	0.174	4.135×10^7	4.924×10^7	0.173	4.170×10^7	4.938×10^7	0.172	4.201×10^7	4.905×10^7
H4	0.208	3.906×10^7	6.667×10^7	0.226	2.090×10^7	4.208×10^7	0.281	3.310×10^7	1.031×10^8
V7	0.205	3.800×10^7	6.298×10^7	0.204	3.860×10^7	6.360×10^7	0.203	4.004×10^7	6.510×10^7
T1	0.228	2.629×10^7	5.380×10^7	0.225	2.736×10^7	5.455×10^7	0.220	3.080×10^7	5.868×10^7
V8	0.235	3.995×10^7	8.732×10^7	0.235	3.999×10^7	8.684×10^7	0.233	3.993×10^7	8.542×10^7
V9	0.269	3.599×10^7	1.025×10^8	0.268	3.667×10^7	1.037×10^8	0.266	4.038×10^7	1.126×10^8
T2	0.288	2.453×10^7	8.017×10^7	0.301	2.871×10^7	1.030×10^8	0.312	3.372×10^7	1.296×10^8
V10	0.302	3.510×10^7	1.264×10^8	0.301	3.531×10^7	1.261×10^8	0.298	3.545×10^7	1.245×10^8
V11	0.337	3.355×10^7	1.508×10^8	0.336	3.376×10^7	1.504×10^8	0.333	3.390×10^7	1.485×10^8
H5	0.343	2.755×10^7	1.278×10^8	0.372	3.235×10^7	1.766×10^8	0.425	3.048×10^7	2.176×10^8
V12	0.374	3.349×10^7	1.851×10^8	0.372	3.367×10^7	1.844×10^8	0.369	3.379×10^7	1.819×10^8
V13	0.413	3.231×10^7	2.178×10^8	0.411	3.252×10^7	2.170×10^8	0.408	3.268×10^7	2.143×10^8

Table E.3: Modal properties for S3

	S3-G1			S3-G2			S3-G3		
Name	f [Hz]	$\tilde{M}$ [kg]	$\tilde{K}$ [Nm^{-1}]	f [Hz]	$\tilde{M}$ [kg]	$\tilde{K}$ [Nm^{-1}]	f [Hz]	$\tilde{M}$ [kg]	$\tilde{K}$ [Nm^{-1}]
H1	0.031	3.897×10^7	1.461×10^6	0.033	3.857×10^7	1.620×10^6	0.034	3.883×10^7	1.766×10^6
H2	0.065	3.128×10^7	5.294×10^6	0.073	3.251×10^7	6.904×10^6	0.080	3.398×10^7	8.562×10^6
V1	0.065	4.291×10^7	7.074×10^6	0.065	4.335×10^7	7.135×10^6	0.064	4.379×10^7	7.153×10^6
V2	0.078	2.222×10^7	5.275×10^6	0.077	2.246×10^7	5.303×10^6	0.077	2.271×10^7	5.300×10^6
V3	0.111	3.355×10^7	1.640×10^7	0.111	3.391×10^7	1.646×10^7	0.110	3.419×10^7	1.644×10^7
V4	0.114	3.900×10^7	2.002×10^7	0.114	3.957×10^7	2.021×10^7	0.113	3.988×10^7	2.011×10^7
H3	0.120	2.647×10^7	1.505×10^7	0.136	2.874×10^7	2.110×10^7	0.150	3.169×10^7	2.831×10^7
V5	0.146	3.561×10^7	3.000×10^7	0.146	3.604×10^7	3.019×10^7	0.145	3.640×10^7	3.011×10^7
V6	0.174	4.175×10^7	4.962×10^7	0.173	4.210×10^7	4.975×10^7	0.172	4.241×10^7	4.943×10^7
H4	0.208	3.953×10^7	6.730×10^7	0.262	3.109×10^7	8.425×10^7	0.282	3.391×10^7	1.064×10^8
V7	0.205	3.859×10^7	6.381×10^7	0.204	3.943×10^7	6.481×10^7	0.203	4.223×10^7	6.857×10^7
T1	0.227	2.469×10^7	5.025×10^7	0.223	2.665×10^7	5.241×10^7	0.218	3.205×10^7	5.991×10^7
V8	0.235	4.013×10^7	8.743×10^7	0.234	4.021×10^7	8.702×10^7	0.232	4.021×10^7	8.576×10^7
V9	0.268	3.653×10^7	1.037×10^8	0.267	3.771×10^7	1.063×10^8	0.266	3.386×10^7	9.425×10^7
T2	0.287	2.491×10^7	8.118×10^7	0.301	2.937×10^7	1.051×10^8	0.311	3.896×10^7	1.487×10^8
V10	0.301	3.536×10^7	1.267×10^8	0.300	3.556×10^7	1.264×10^8	0.298	3.570×10^7	1.249×10^8
V11	0.336	3.381×10^7	1.511×10^8	0.335	3.401×10^7	1.506×10^8	0.332	3.415×10^7	1.488×10^8
H5	0.343	2.852×10^7	1.322×10^8	0.373	3.325×10^7	1.829×10^8	0.427	3.137×10^7	2.254×10^8
V12	0.373	3.372×10^7	1.852×10^8	0.371	3.390×10^7	1.845×10^8	0.368	3.403×10^7	1.820×10^8
V13	0.412	3.256×10^7	2.180×10^8	0.410	3.277×10^7	2.172×10^8	0.406	3.293×10^7	2.145×10^8

Appendix F

VIV Tests

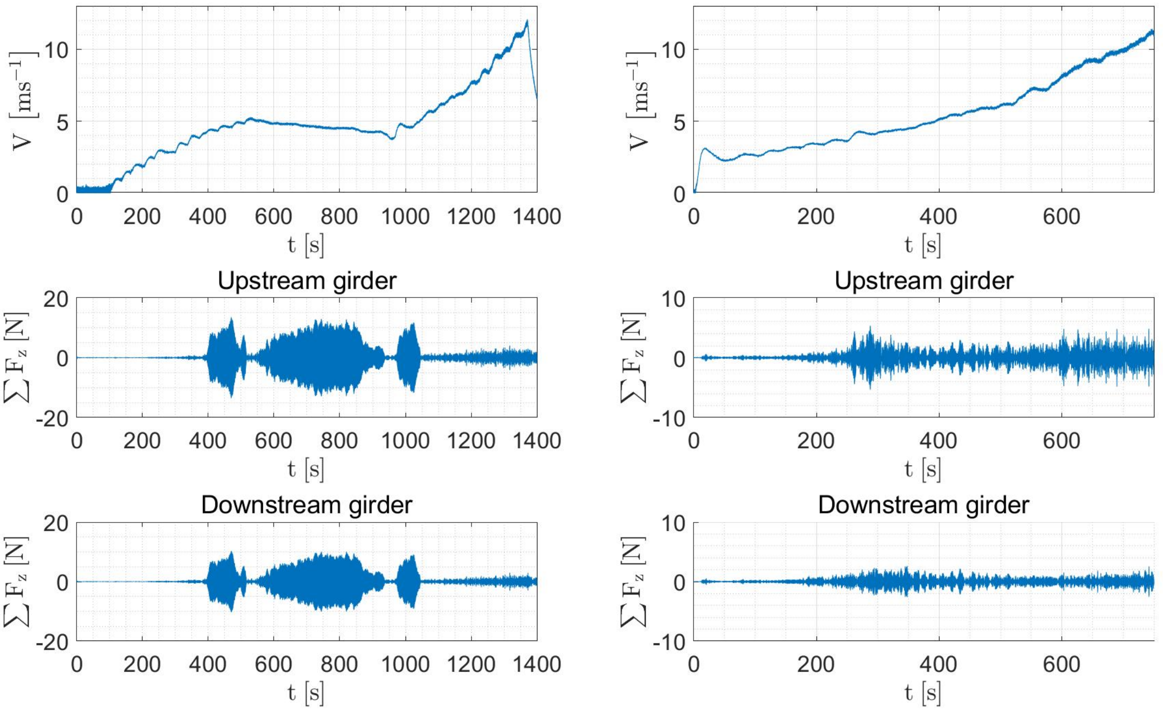

(a) S1-G1

(b) S1-G2

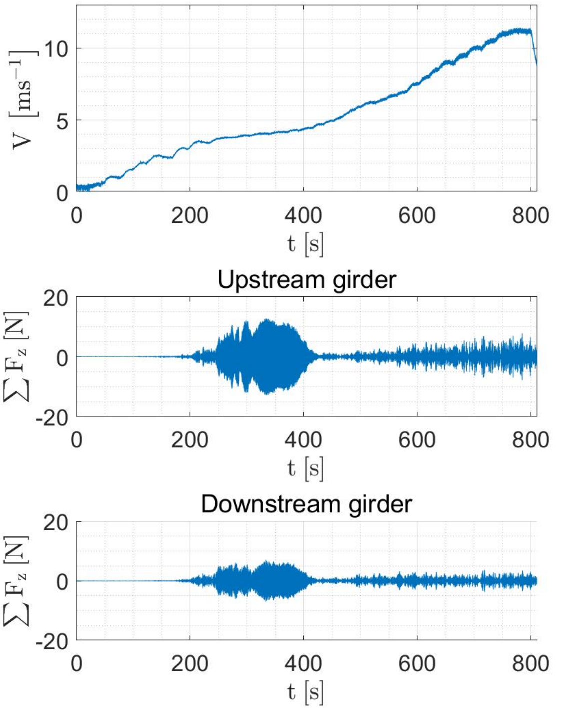

(c) S1-G3

Figure F.1: Results from VIV tests S1

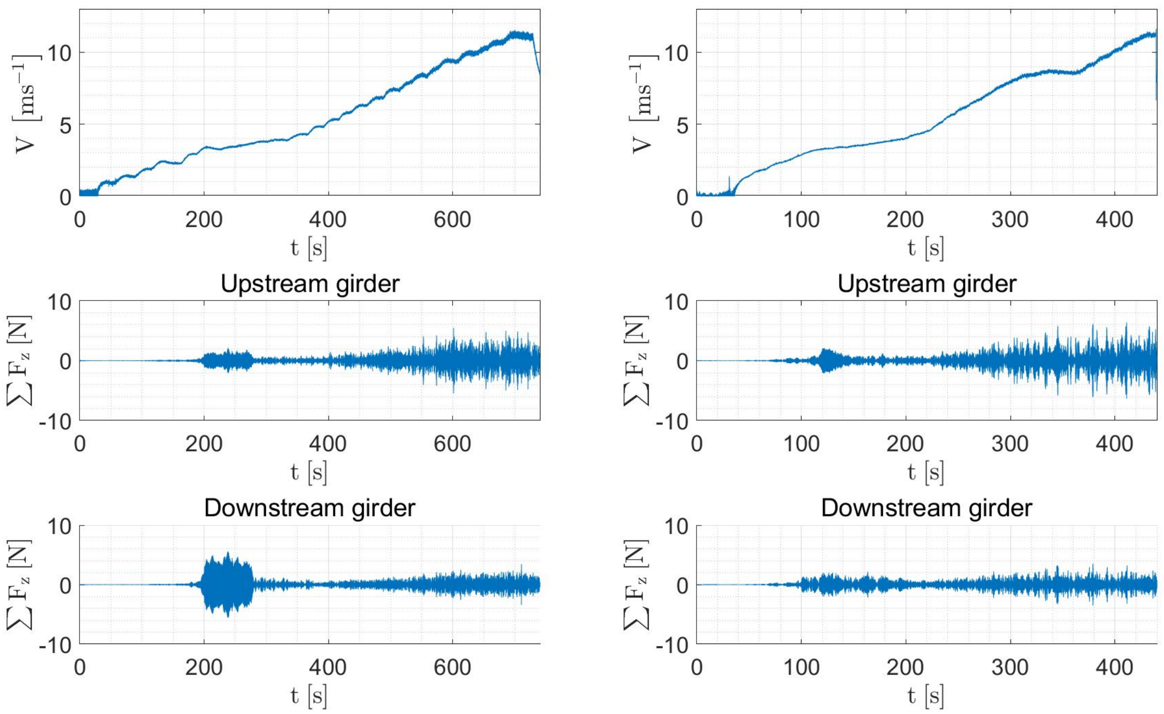

(a) S2-G1

(b) S2-G2

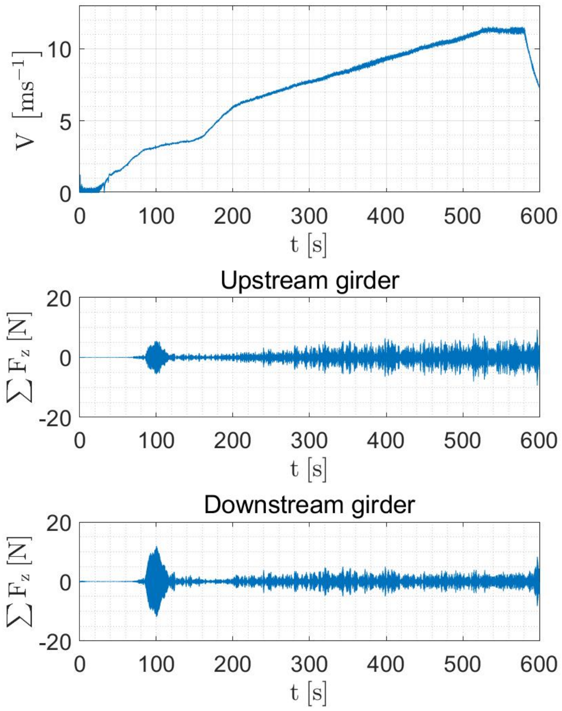

(c) S2-G3

Figure F.2: Results from VIV tests S2

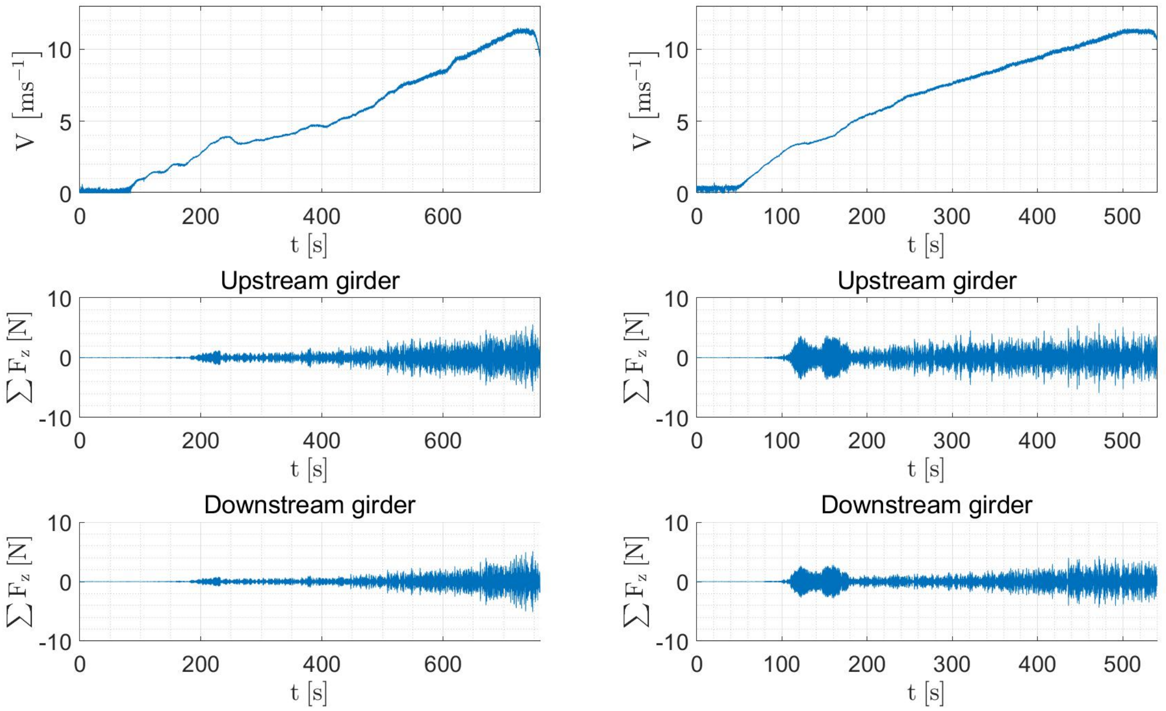

(a) S3-G1

(b) S3-G2

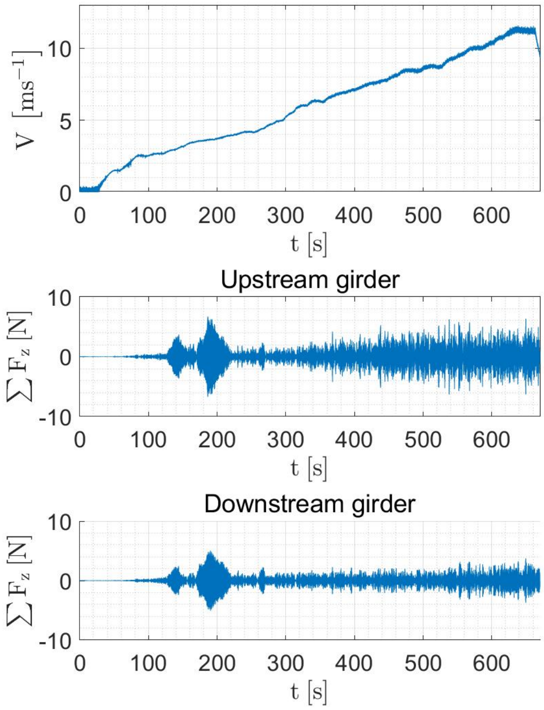

(c) S3-G3

Figure F.3: Results from VIV tests S3

Appendix G

Damping of Section Models

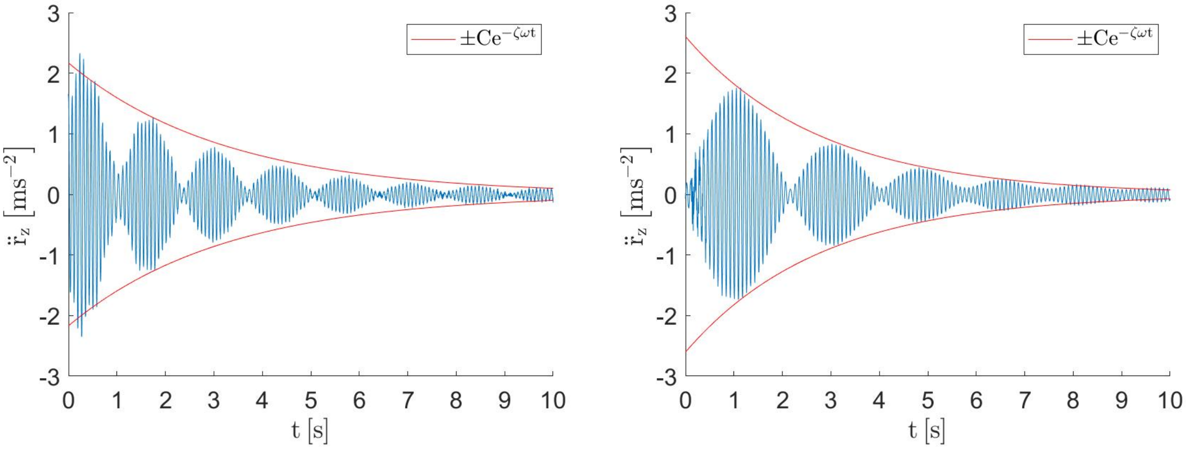

(a) S1, $\zeta = 0.4\,\%$

(b) S2, $\zeta = 0.5\,\%$

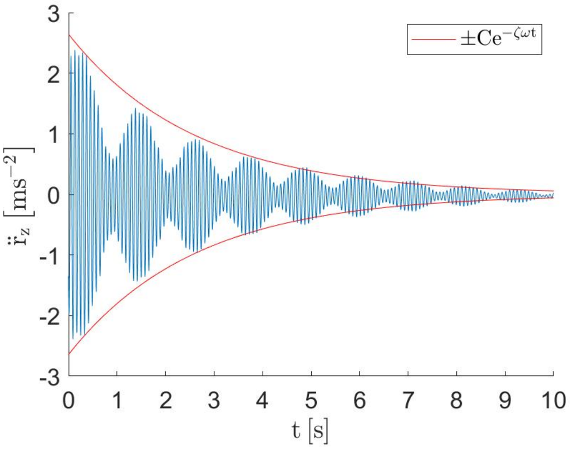

(c) S3, $\zeta = 0.5\,\%$

Figure G.1: Decay of motion

Appendix H

Static Coefficients

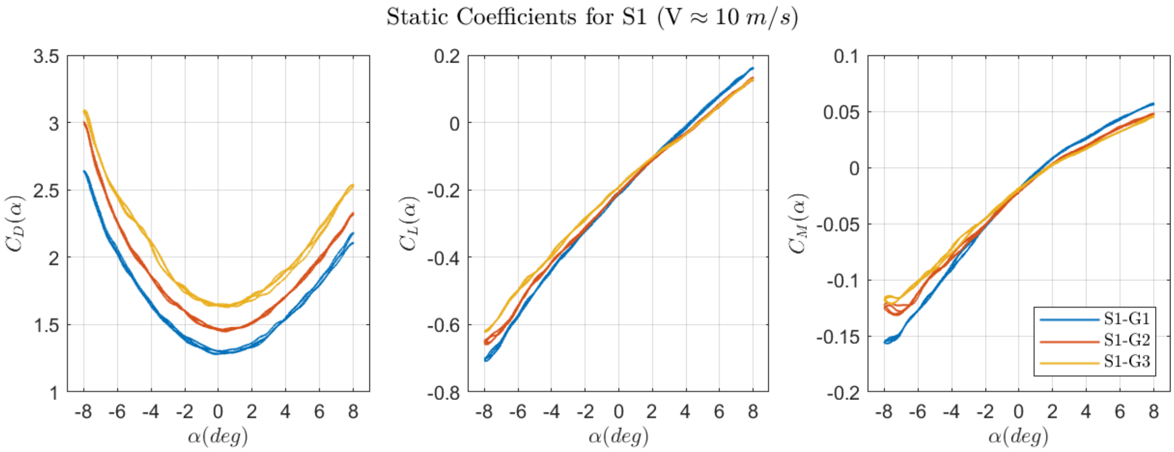

(a)

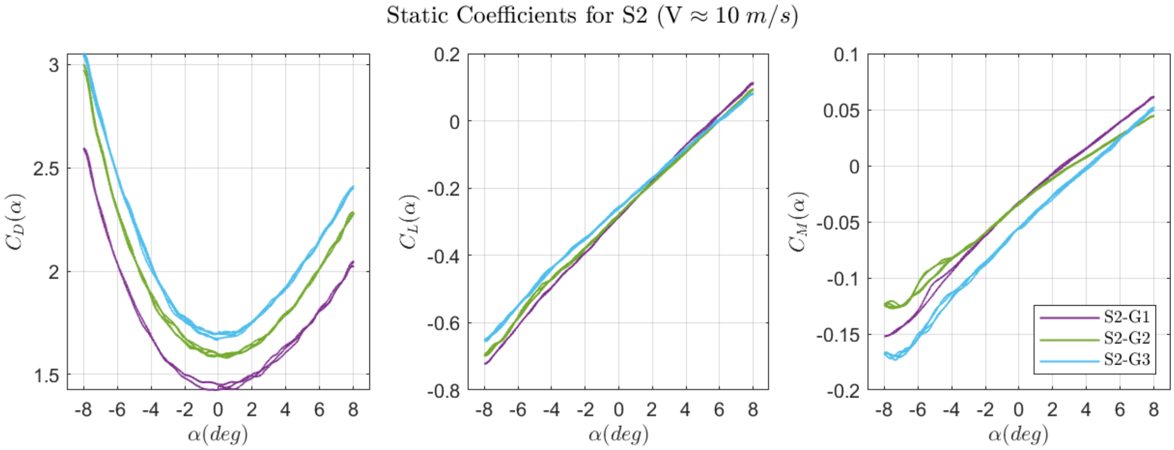

(b)

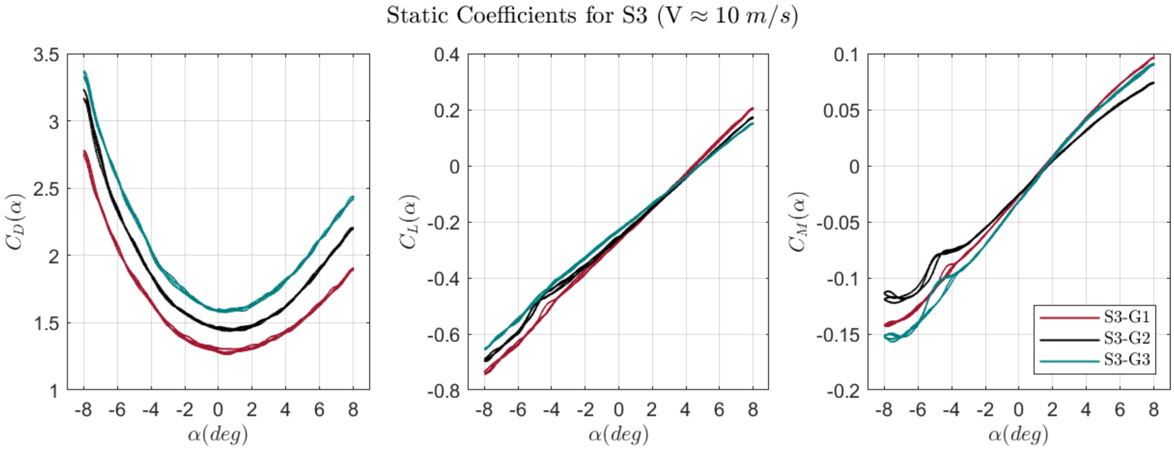

(c)

Figure H.1: Static coefficients for same section with varying gap widths.

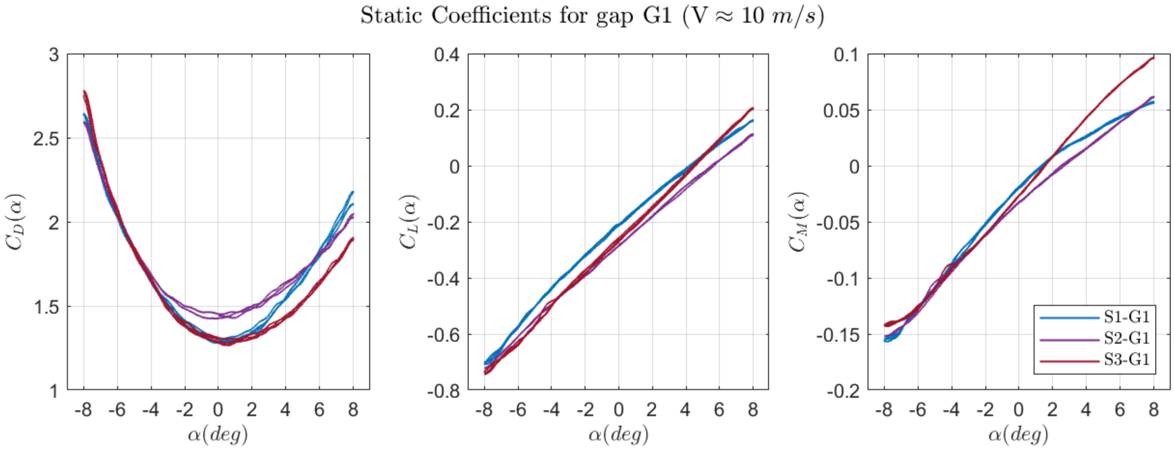

(a)

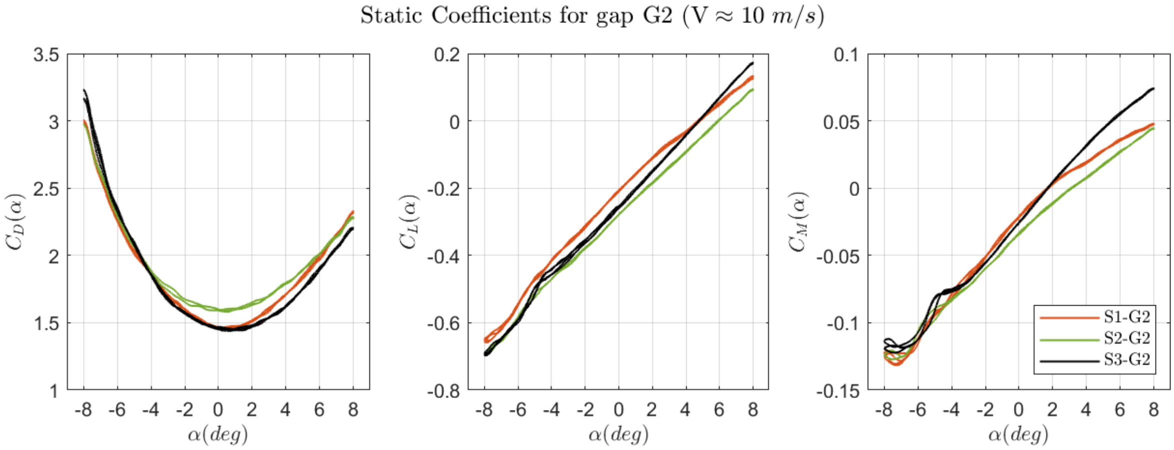

(b)

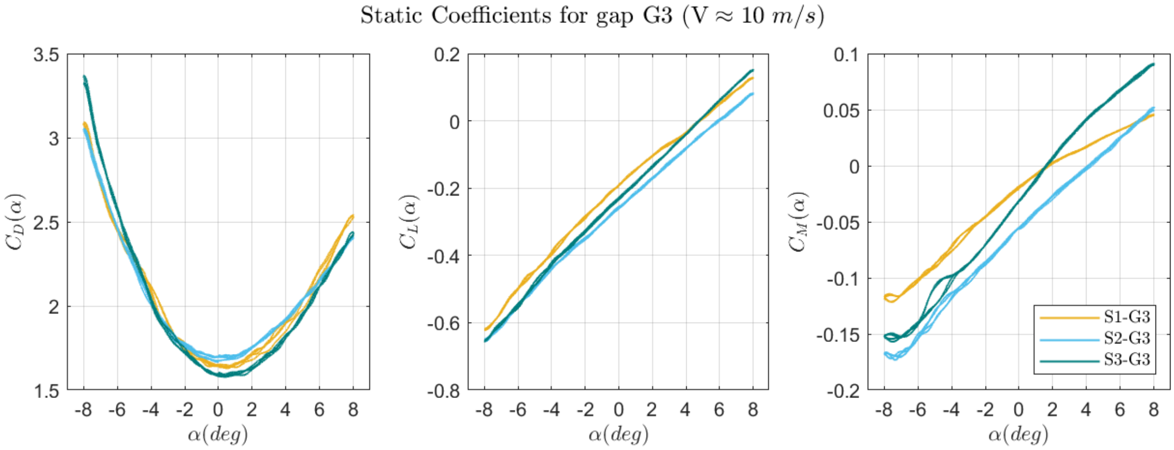

(c)

Figure H.2: Static coefficients for same gap widths with varying section type: (a) Gap 1 (b) Gap 2 (C) Gap 3

Appendix I

Aerodynamic Derivatives

The following pages show the scatter plots with separated data for the wind speeds $V \approx 6$ m/s and $V \approx 8$ m/s for each of the nine configurations. Legend can be seen in Figure I.1.

Included is also figures containing the polynomial fitted ADs for all configurations as functions of reduced velocity (V_r). Colour maps for the different curves can be found next to the figures.

Figure I.1: Legend for figures I.2 (a)-(r)

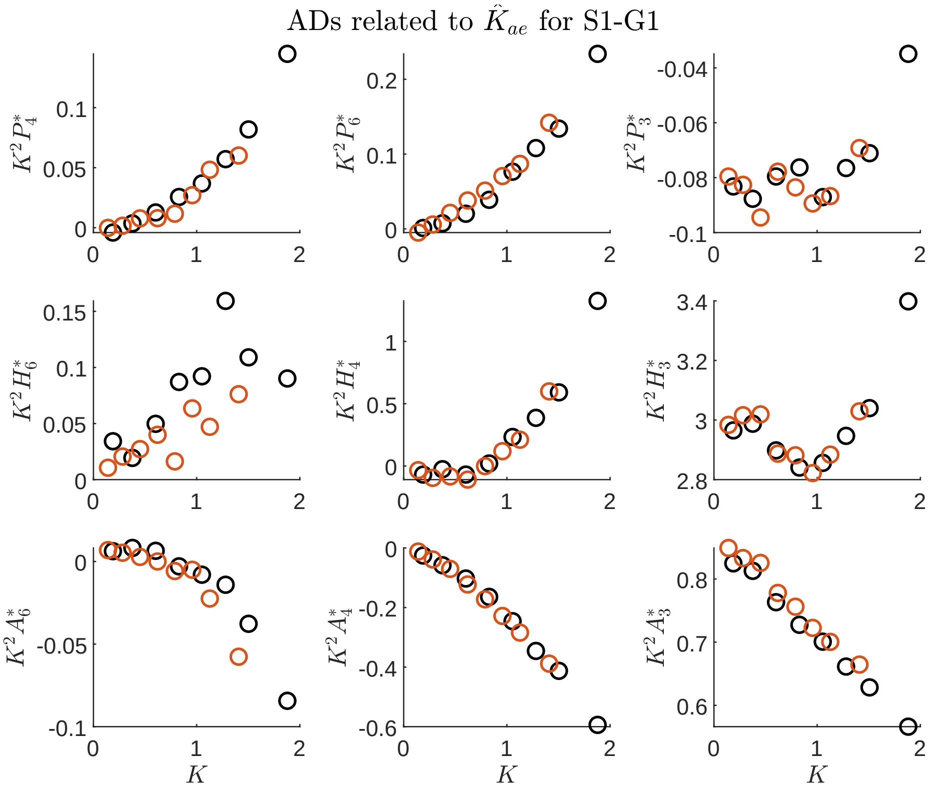
ADs related to $\hat{K}_{ae}$ for S1-G1
$K^2P_4^*$
$K^2P_6^*$
$K^2P_3^*$
$K^2H_6^*$
$K^2H_4^*$
$K^2H_3^*$
$K^2A_6^*$
$K^2A_4^*$
$K^2A_3^*$
0.1
0.05
0
0.2
0.1
0
-0.04
-0.06
-0.08
-0.1
0.15
0.1
0.05
0
1
0.5
0
3.4
3.2
3
2.8
0
-0.05
-0.1
0
-0.2
-0.4
-0.6
0.8
0.7
0.6
0
1
2
K

(a)

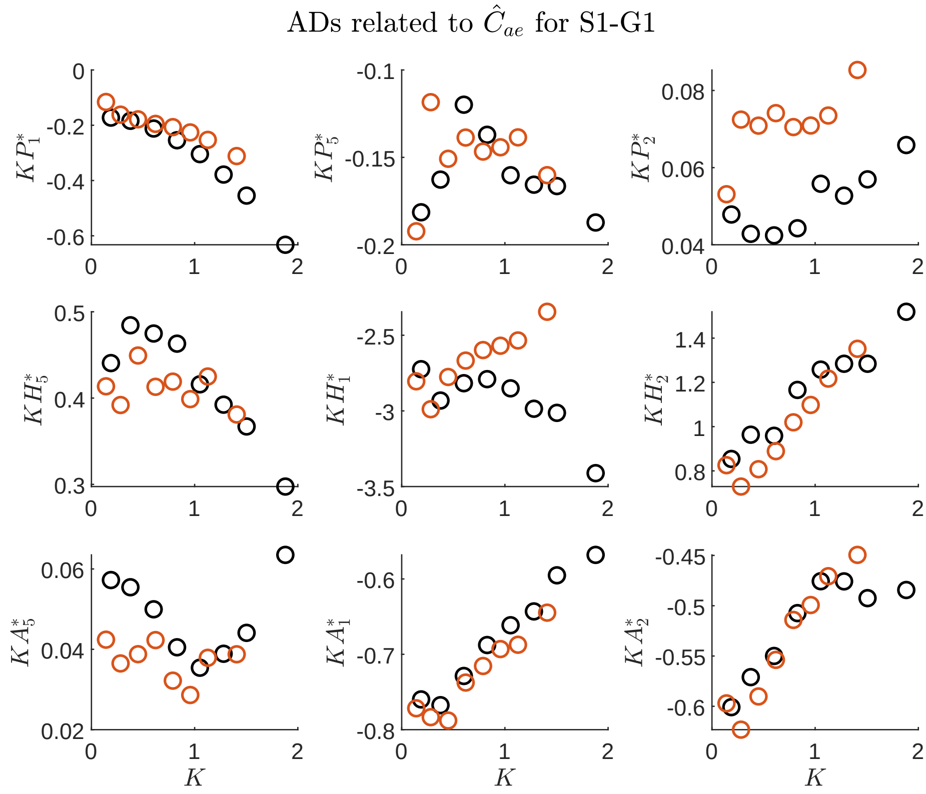
ADs related to $\hat{C}_{ae}$ for S1-G1
KP_1^*
KP_5^*
KP_2^*
KH_5^*
KH_1^*
KH_2^*
KA_5^*
KA_1^*
KA_2^*
0
-0.2
-0.4
-0.6
-0.1
-0.15
-0.2
0.08
0.06
0.04
0.5
0.4
0.3
-2.5
-3
-3.5
1.4
1.2
1
0.8
0.06
0.04
0.02
-0.6
-0.7
-0.8
-0.45
-0.5
-0.55
-0.6
0
1
2
K

(b)

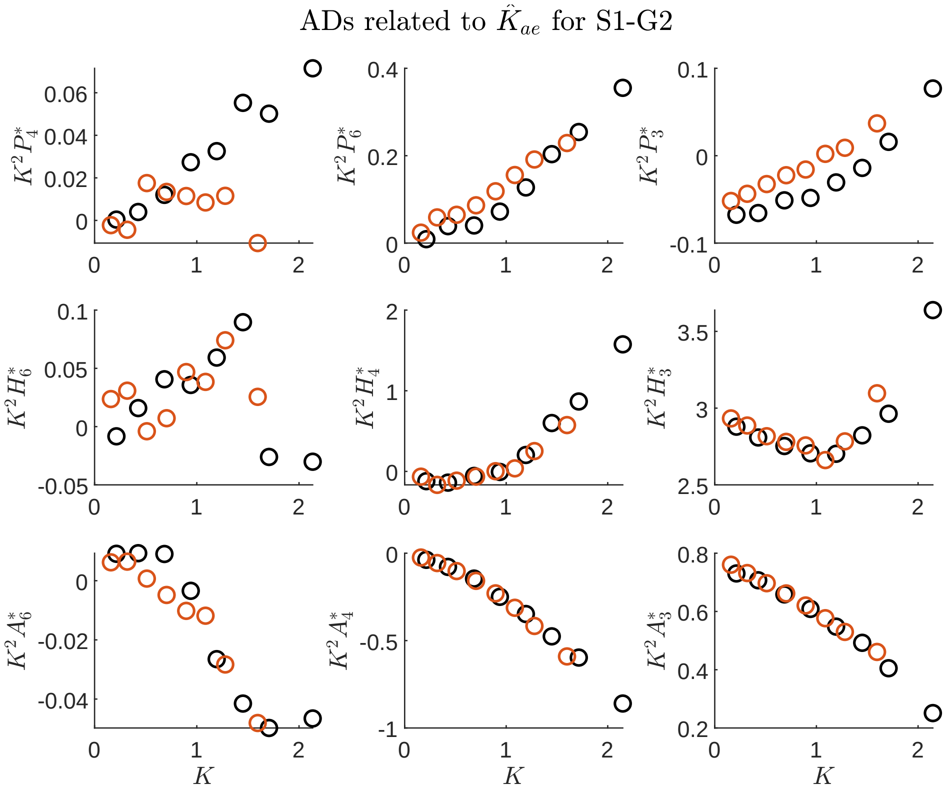

ADs related to $\hat{K}_{ae}$ for S1-G2

(c)

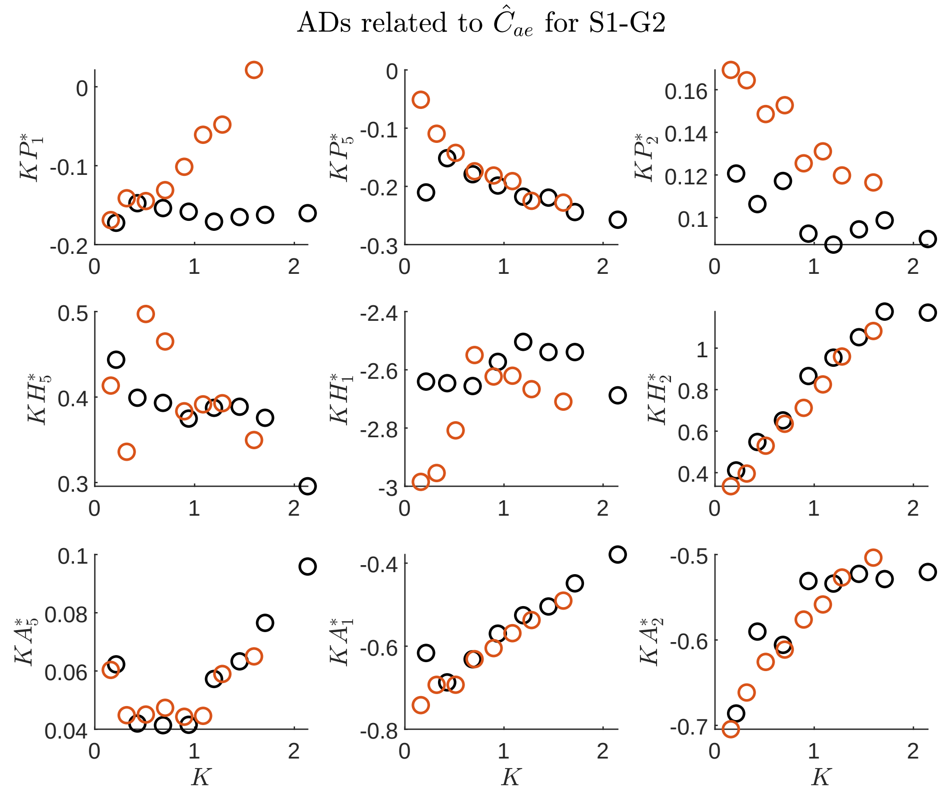

ADs related to $\hat{C}_{ae}$ for S1-G2

(d)

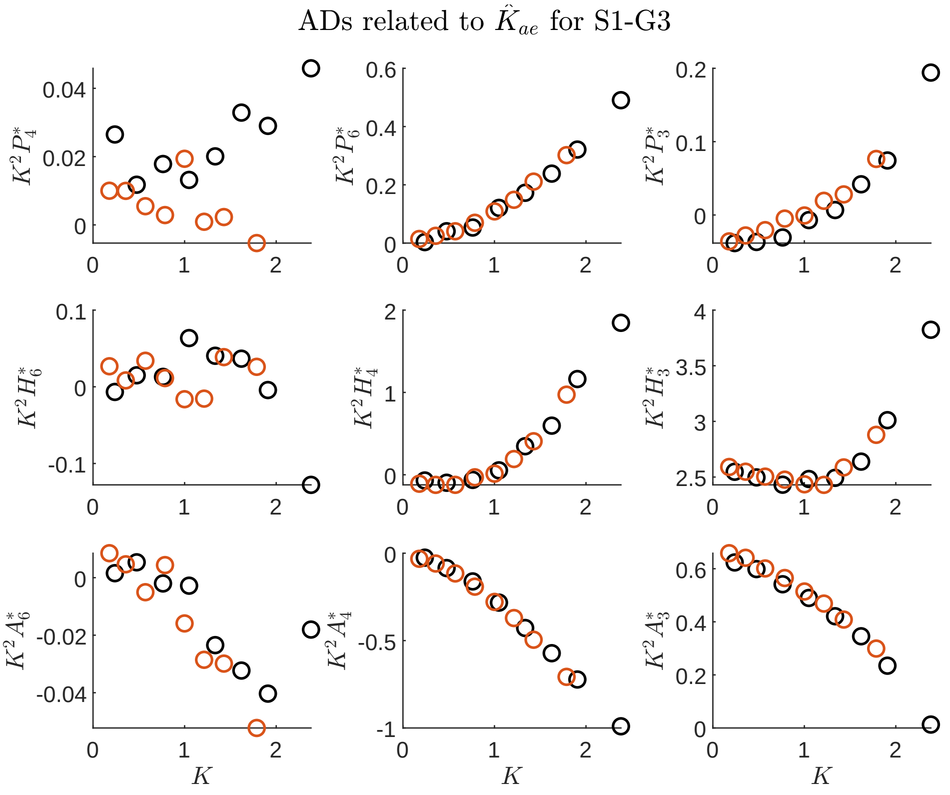
ADs related to $\hat{K}_{ae}$ for S1-G3
$K^2P_4^*$
$K^2P_6^*$
$K^2P_3^*$
$K^2H_6^*$
$K^2H_4^*$
$K^2H_3^*$
$K^2A_6^*$
$K^2A_4^*$
$K^2A_3^*$
K
0
1
2

(e)

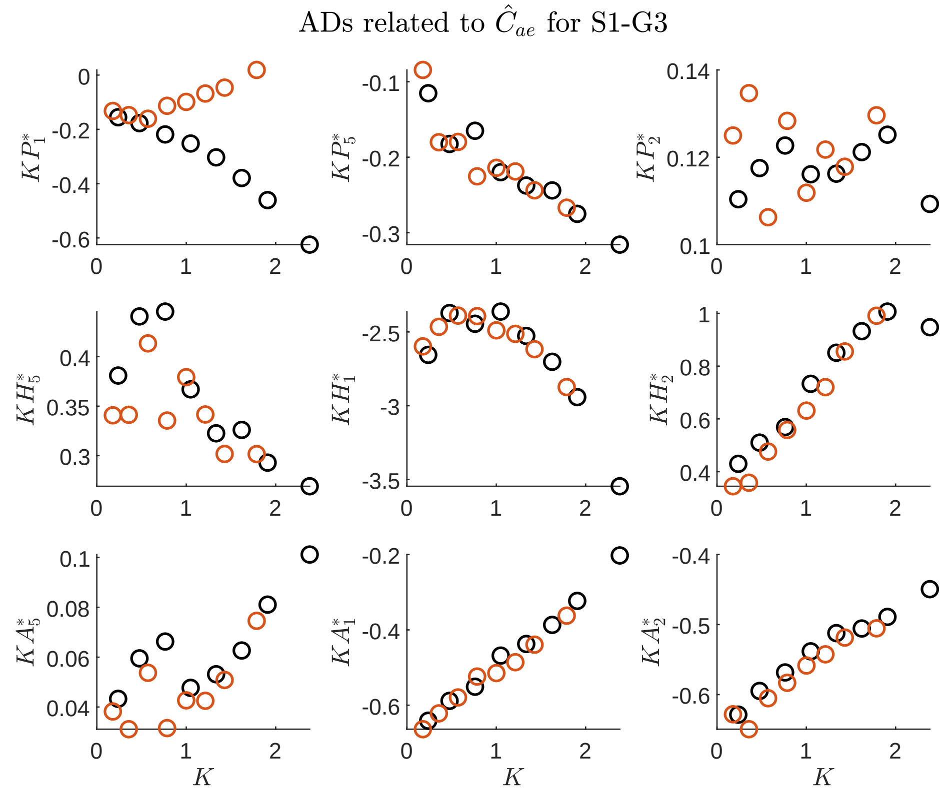
ADs related to $\hat{C}_{ae}$ for S1-G3
KP_1^*
KP_5^*
KP_2^*
KH_5^*
KH_1^*
KH_2^*
KA_5^*
KA_1^*
KA_2^*
K
0
1
2

(f)

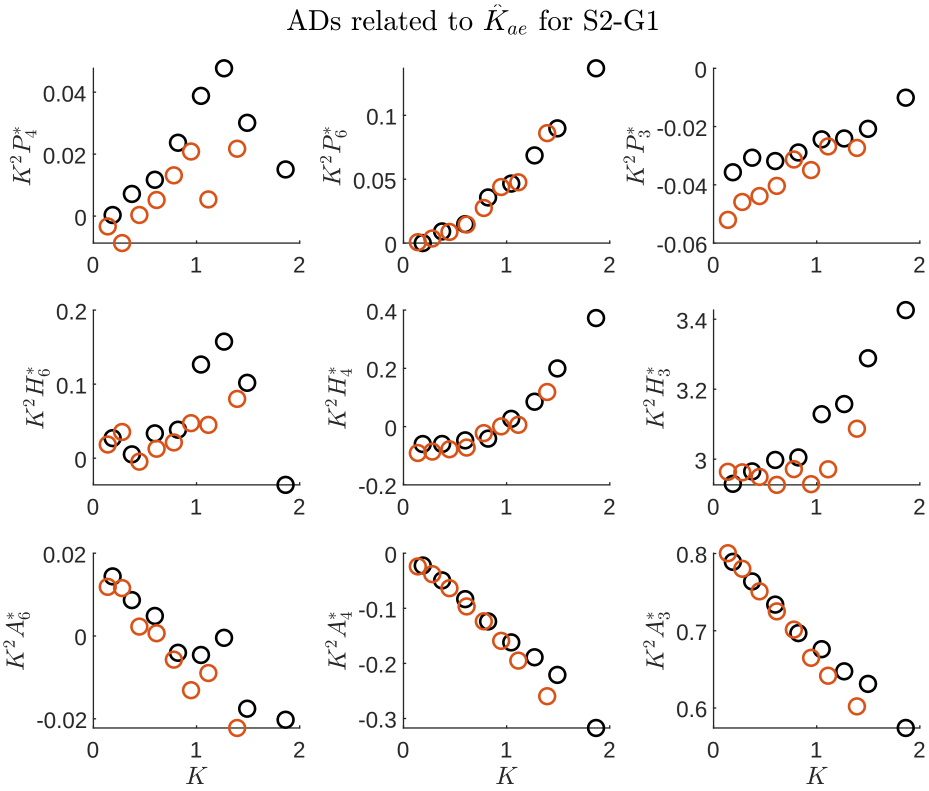
ADs related to $\hat{K}_{ae}$ for S2-G1
$K^2P_4^*$
$K^2P_6^*$
$K^2P_3^*$
$K^2H_6^*$
$K^2H_4^*$
$K^2H_3^*$
$K^2A_6^*$
$K^2A_4^*$
$K^2A_3^*$
0.04
0.02
0
0.1
0.05
0
-0.02
-0.04
-0.06
0.2
0.1
0
0.4
0.2
0
-0.2
3.4
3.2
3
0.02
0
-0.02
-0.1
-0.2
-0.3
0.8
0.7
0.6
0
1
2
K

(g)

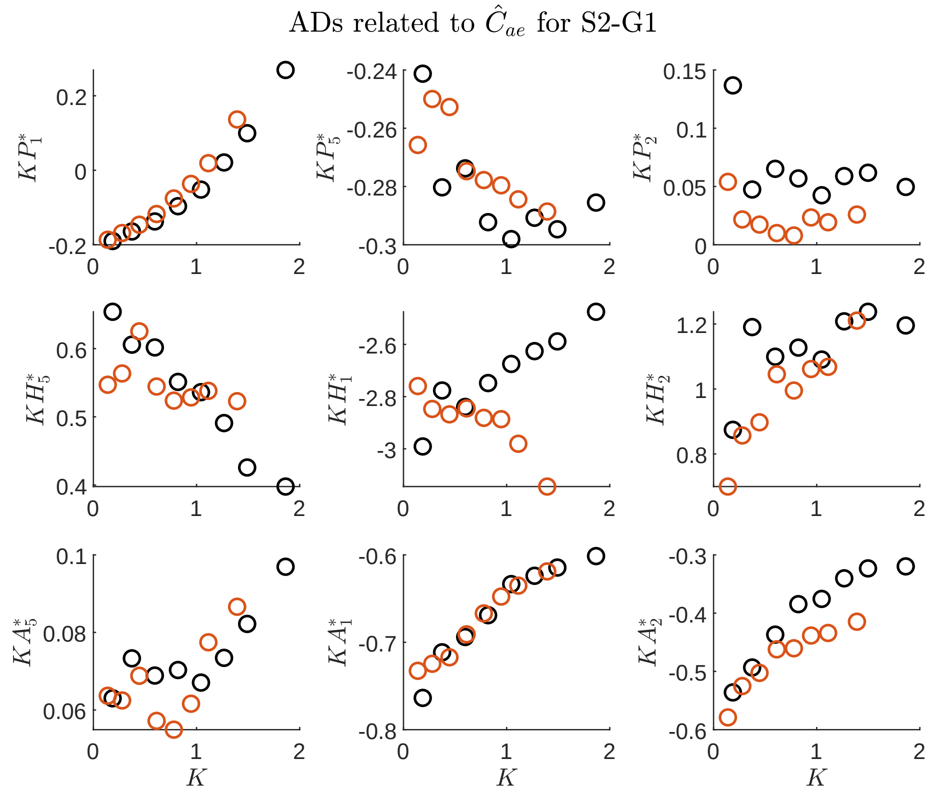
ADs related to $\hat{C}_{ae}$ for S2-G1
KP_1^*
KP_5^*
KP_2^*
KH_5^*
KH_1^*
KH_2^*
KA_5^*
KA_1^*
KA_2^*
0.2
0
-0.2
-0.24
-0.26
-0.28
-0.3
0.15
0.1
0.05
0
0.6
0.5
0.4
-2.6
-2.8
-3
1.2
1
0.8
0.1
0.08
0.06
-0.6
-0.7
-0.8
-0.3
-0.4
-0.5
-0.6
0
1
2
K

(h)

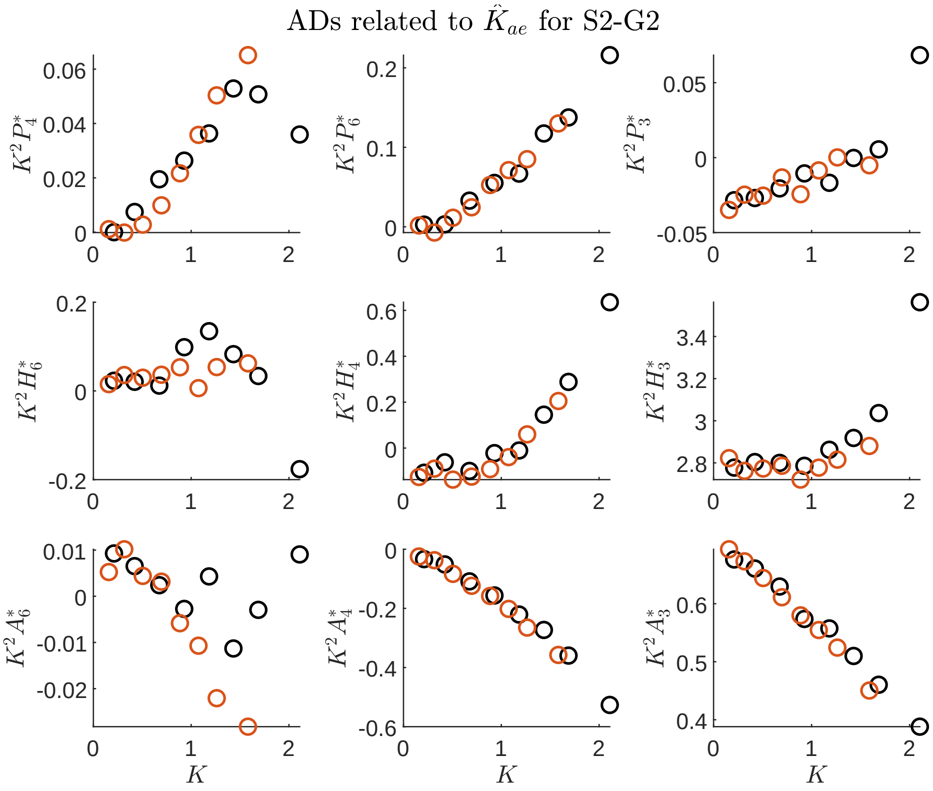
ADs related to $\hat{K}_{ae}$ for S2-G2

(i)

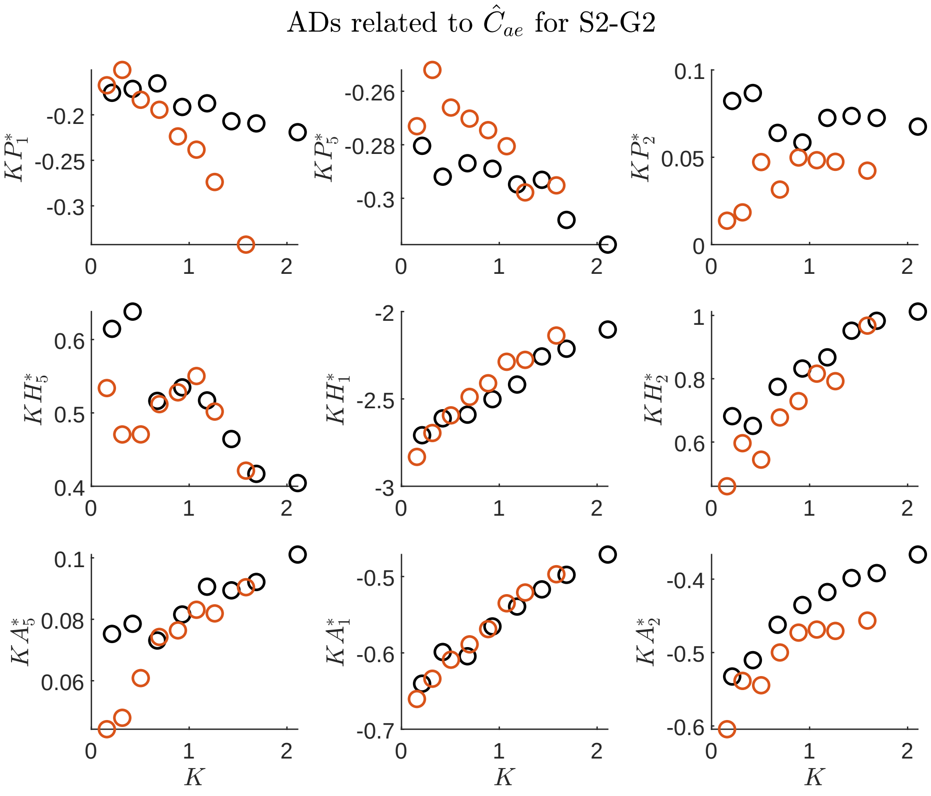
ADs related to $\hat{C}_{ae}$ for S2-G2

(j)

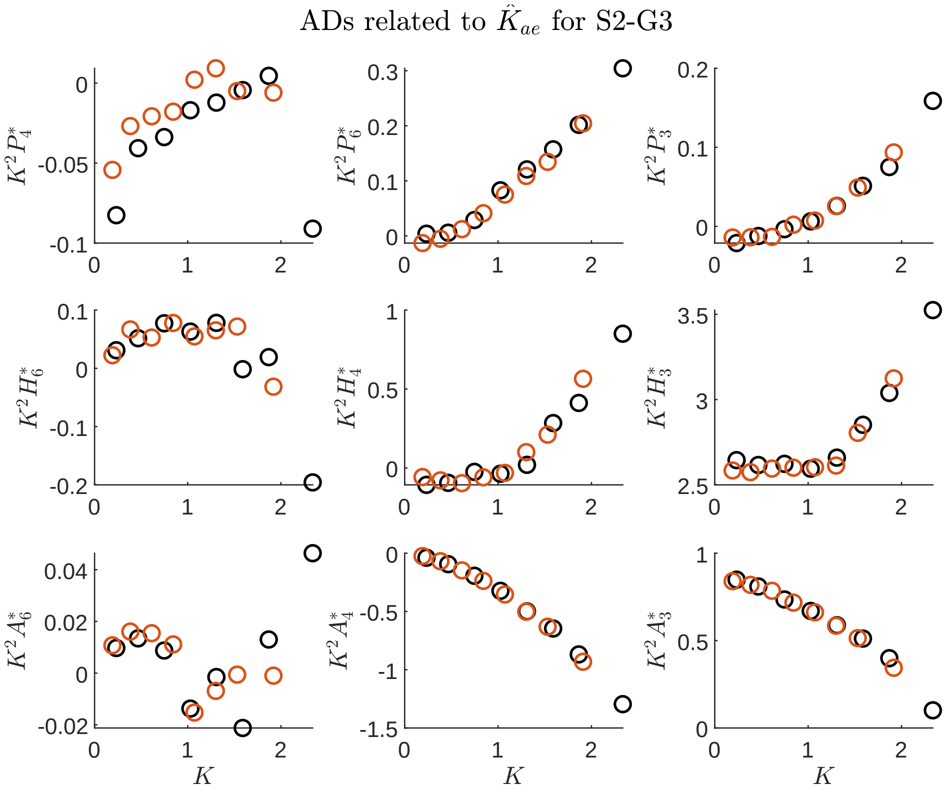

ADs related to $\hat{K}_{ae}$ for S2-G3

(k)

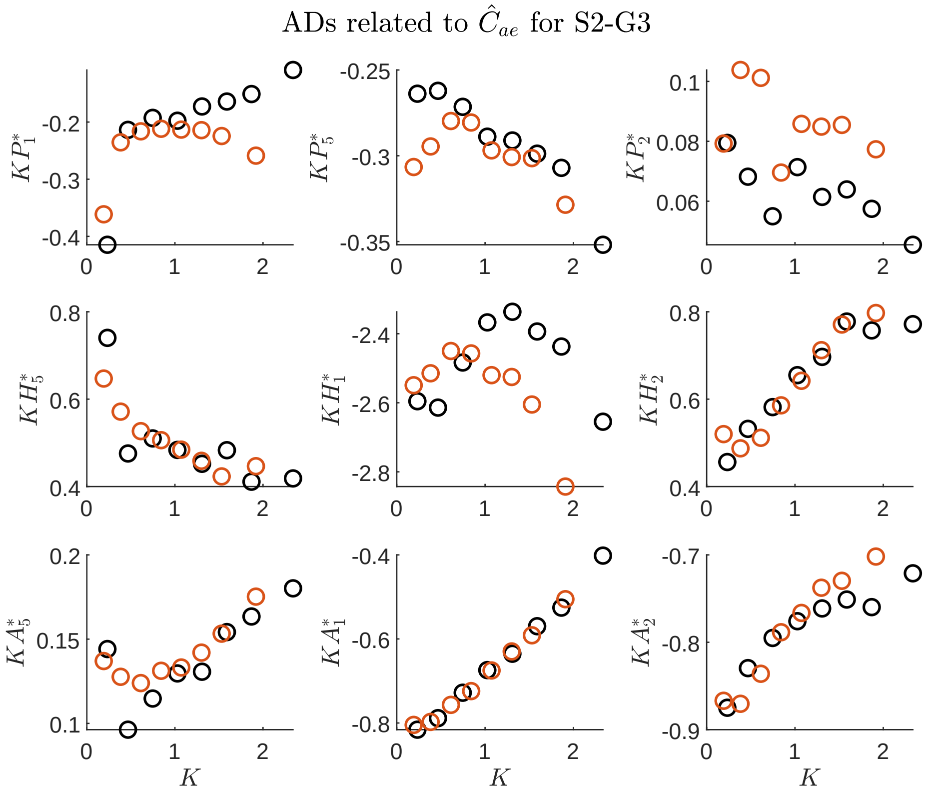

ADs related to $\hat{C}_{ae}$ for S2-G3

(l)

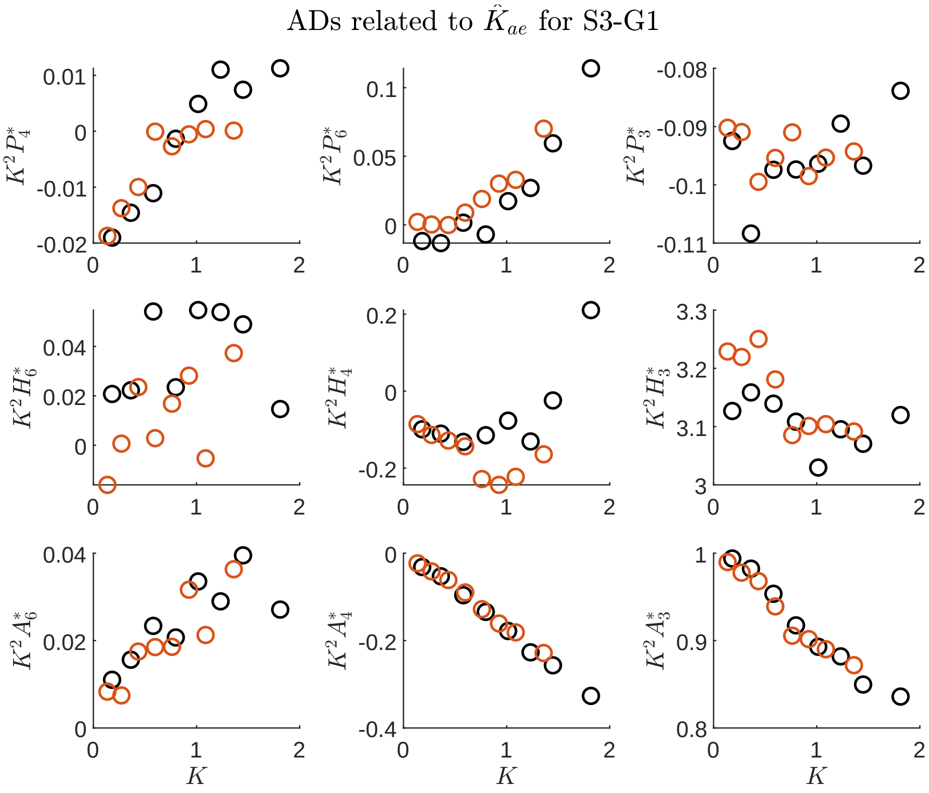
ADs related to $\hat{K}_{ae}$ for S3-G1
$K^2P_4^*$
0.01
0
-0.01
-0.02
$K^2P_6^*$
0.1
0.05
0
$K^2P_3^*$
-0.08
-0.09
-0.1
-0.11
$K^2H_6^*$
0.04
0.02
0
$K^2H_4^*$
0.2
0
-0.2
$K^2H_3^*$
3.3
3.2
3.1
3
$K^2A_6^*$
0.04
0.02
0
$K^2A_4^*$
0
-0.2
-0.4
$K^2A_3^*$
1
0.9
0.8
0
1
2
K

(m)

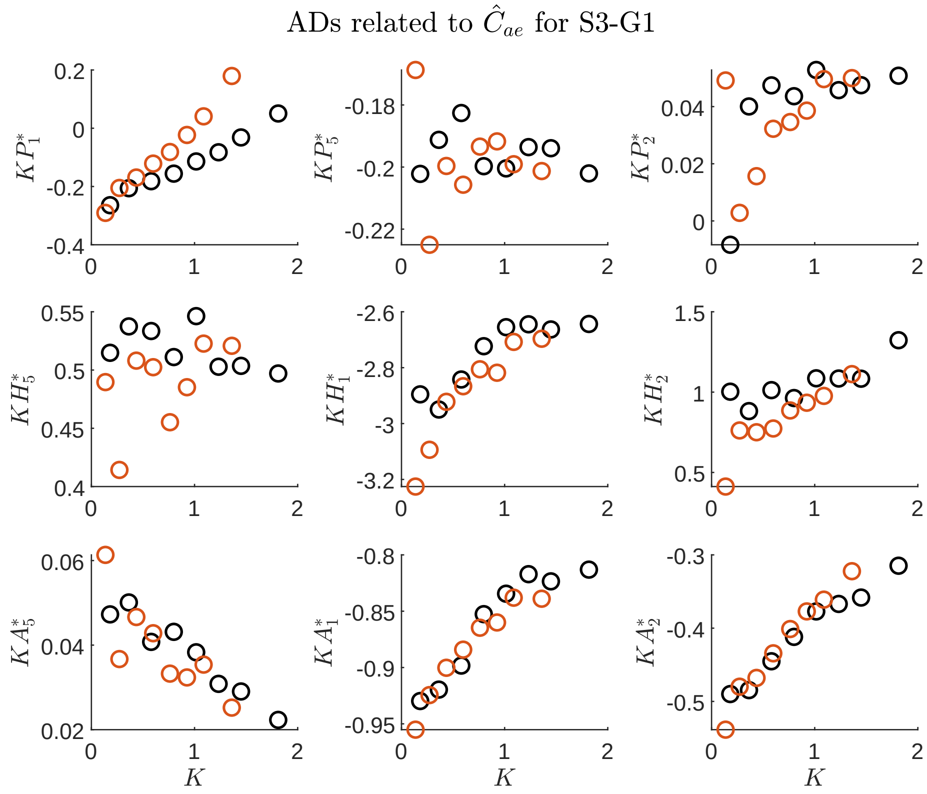
ADs related to $\hat{C}_{ae}$ for S3-G1
KP_1^*
0.2
0
-0.2
-0.4
KP_5^*
-0.18
-0.2
-0.22
KP_2^*
0.04
0.02
0
KH_5^*
0.55
0.5
0.45
0.4
KH_1^*
-2.6
-2.8
-3
-3.2
KH_2^*
1.5
1
0.5
KA_5^*
0.06
0.04
0.02
KA_1^*
-0.8
-0.85
-0.9
-0.95
KA_2^*
-0.3
-0.4
-0.5
0
1
2
K

(n)

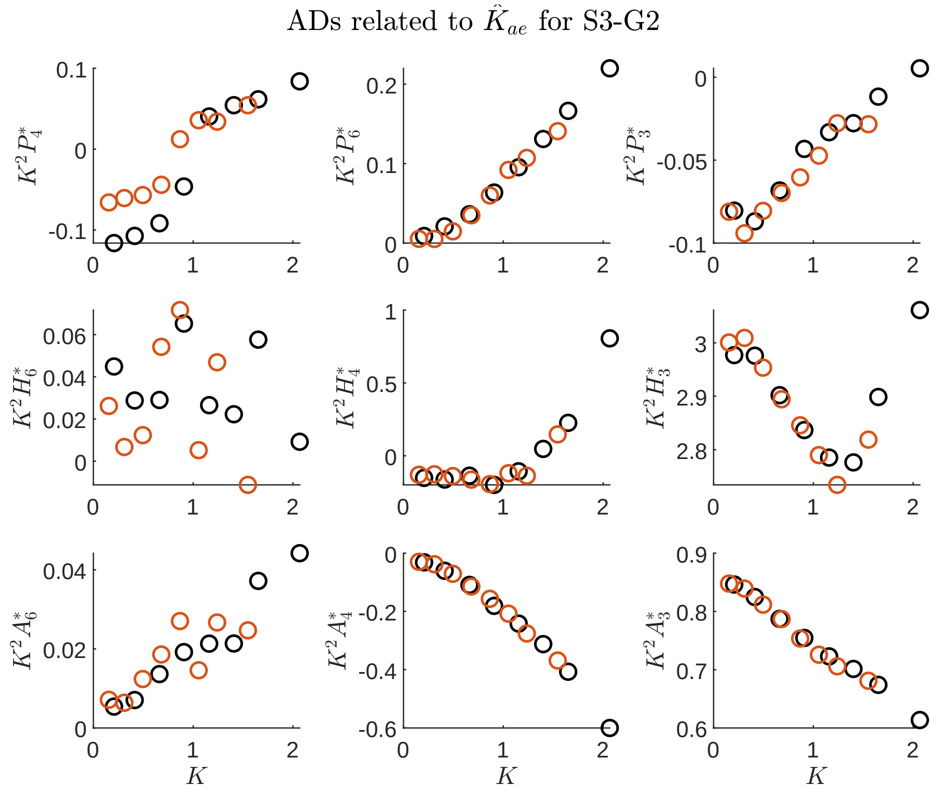

ADs related to $\hat{K}_{ae}$ for S3-G2

(o)

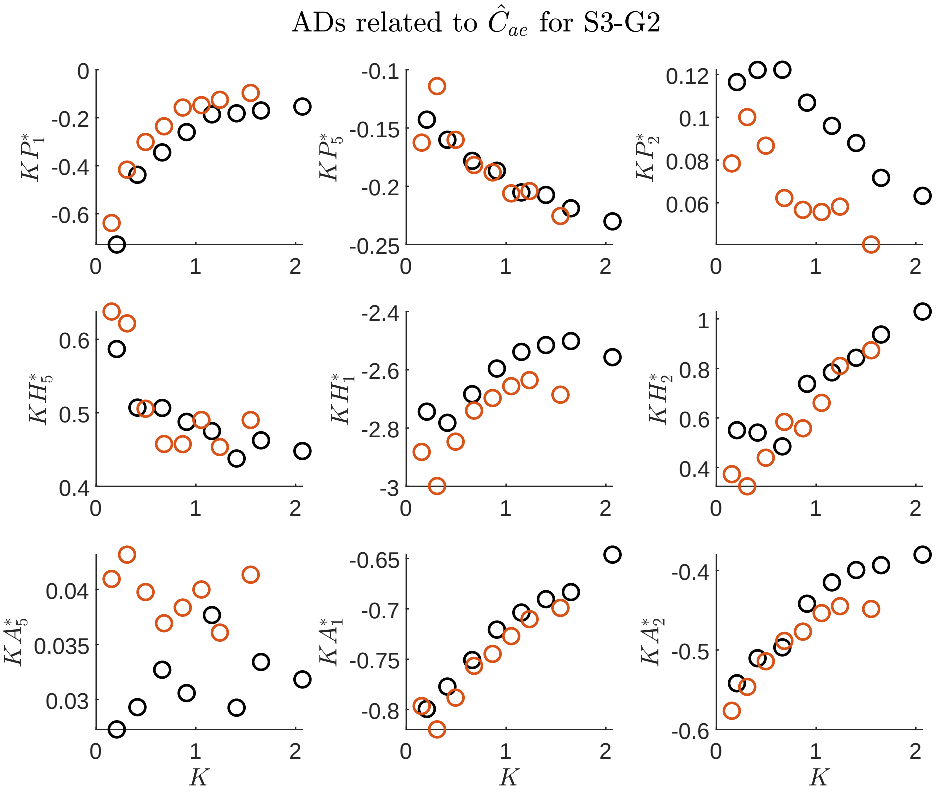

ADs related to $\hat{C}_{ae}$ for S3-G2

(p)

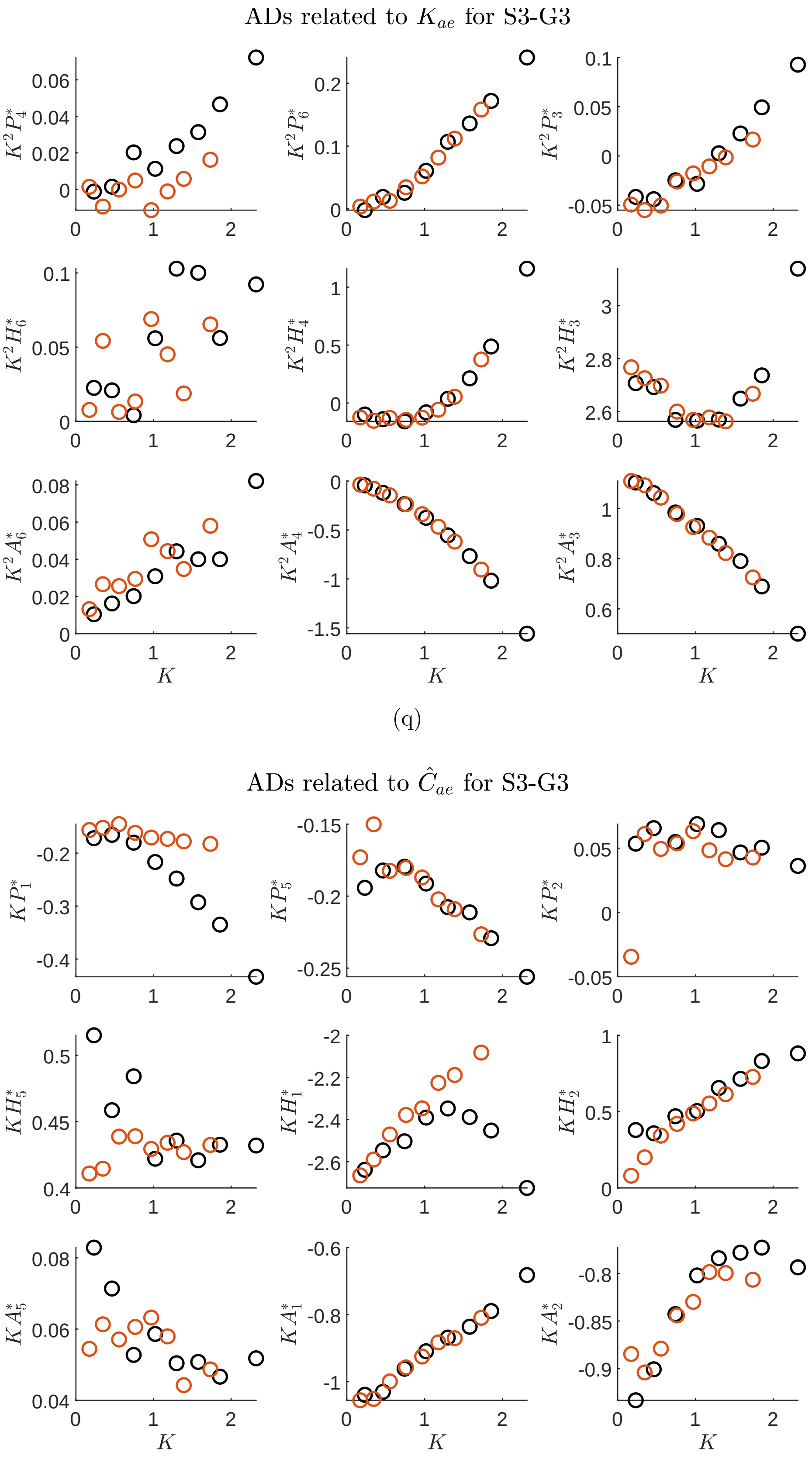
ADs related to K_{ae} for S3-G3

(q)

ADs related to $\hat{C}_{ae}$ for S3-G3

(r)

Figure I.2: Scatter plots of ADs for each of the nine configurations.

ADs related to $\hat{K}_{ae}$

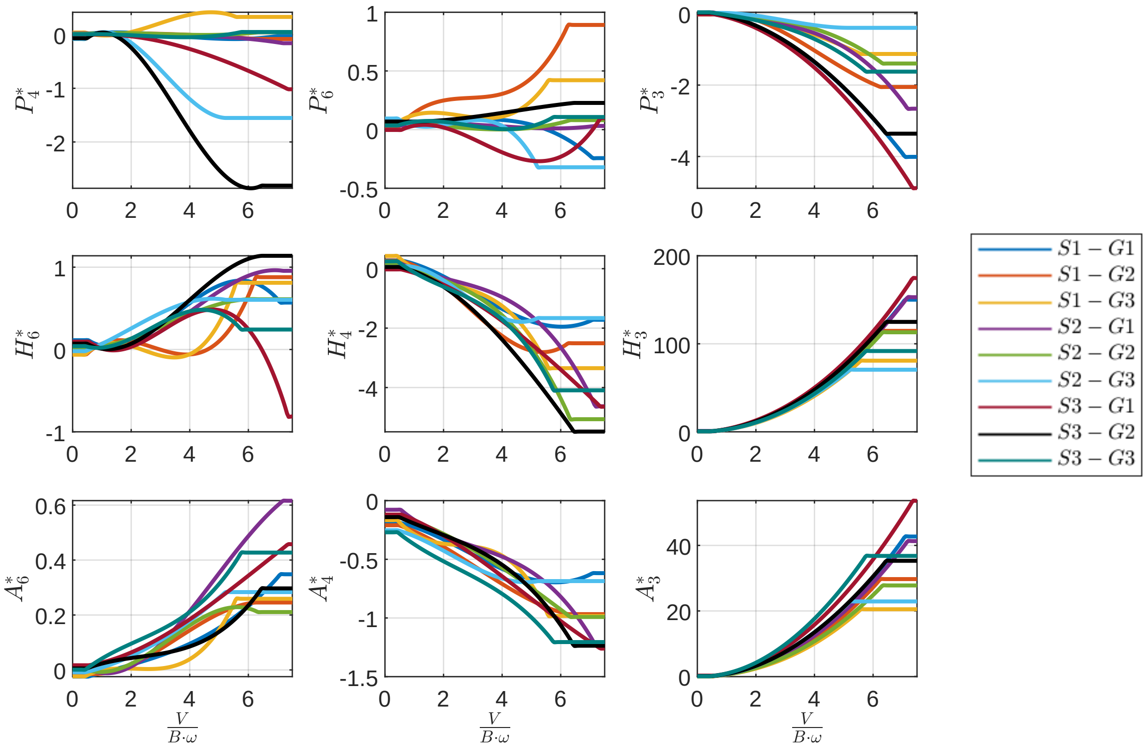

ADs related to $\hat{C}_{ae}$

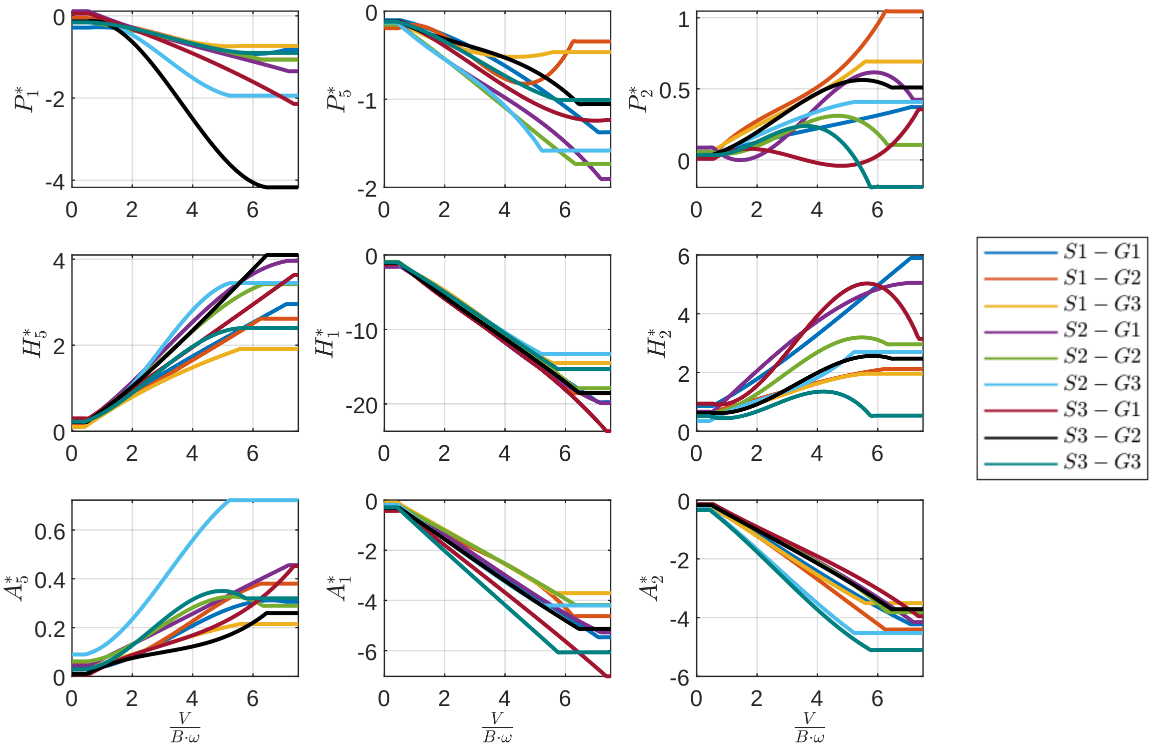

Figure I.3: Polynomial fit for all configurations with ADs as functions of V_r

Appendix J

In-Wind Frequencies and Damping Ratios

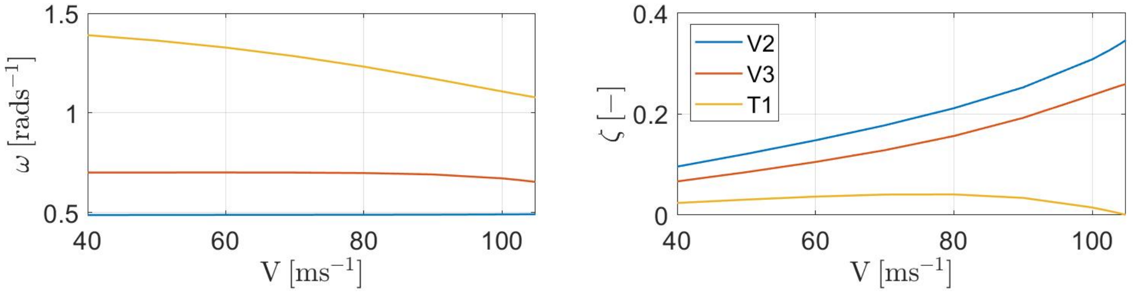

(a) S2-G1

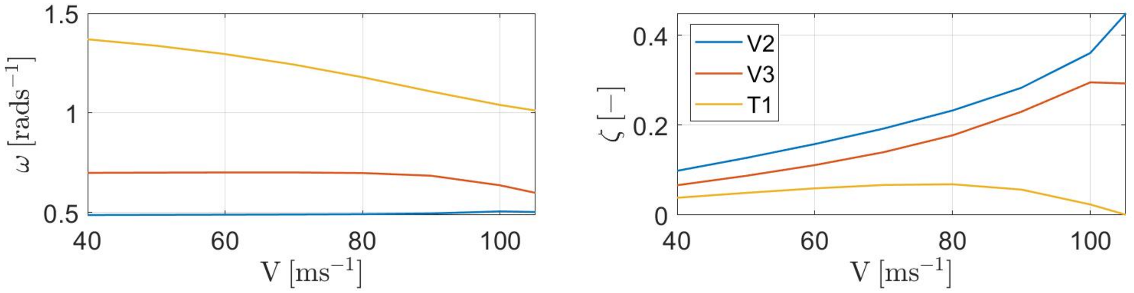

(b) S2-G2

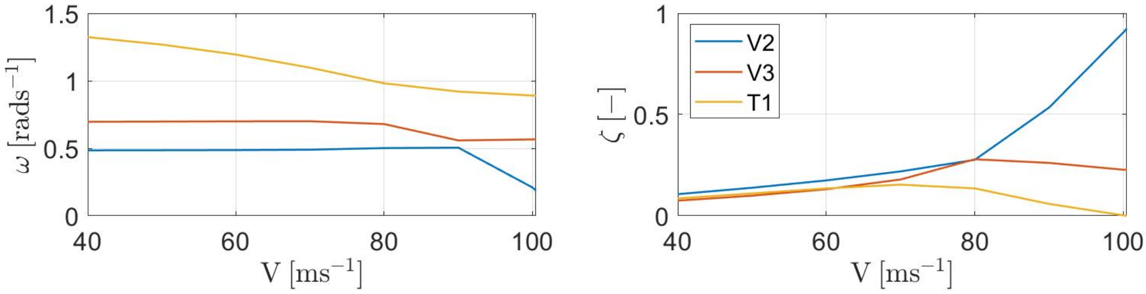

(c) S2-G2

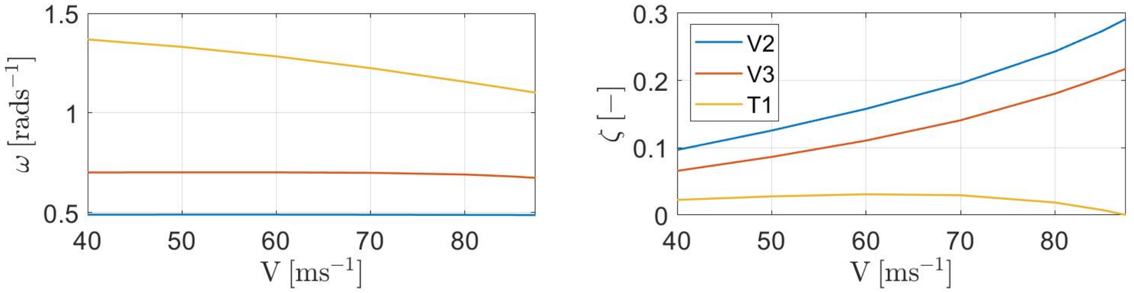

(d) S3-G1

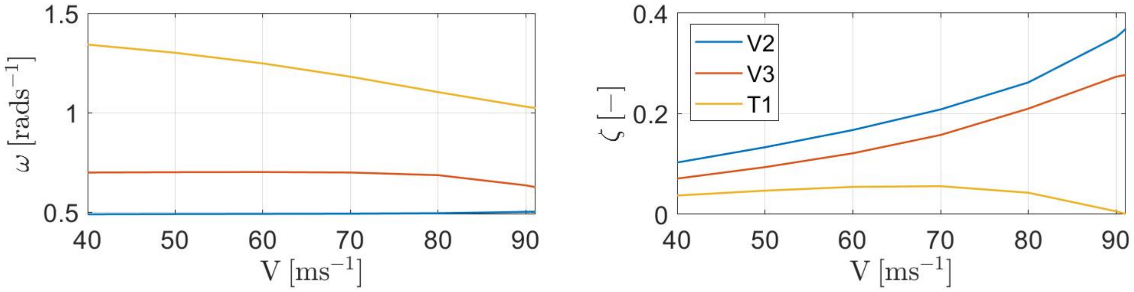

(e) S3-G2

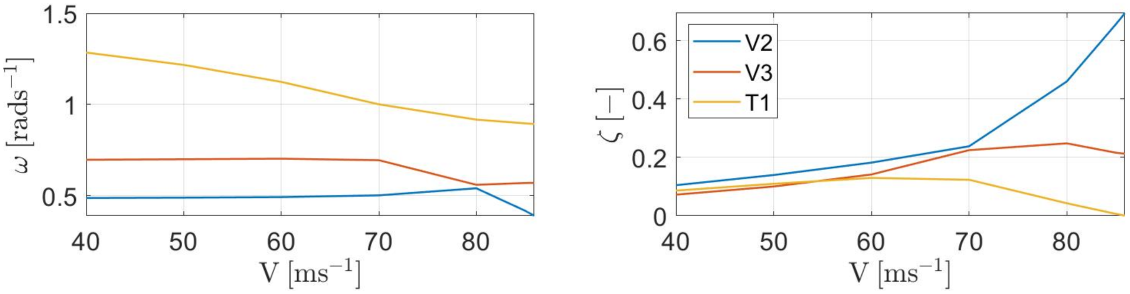

(f) S3-G3

Figure J.0: In-wind frequencies (left) and damping ratios (right) of the three-mode flutter phenomenon of S2 and S3

Appendix K

Argand Diagrams of Flutter Mode Complexity

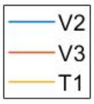

(a) Legend for Argand diagrams

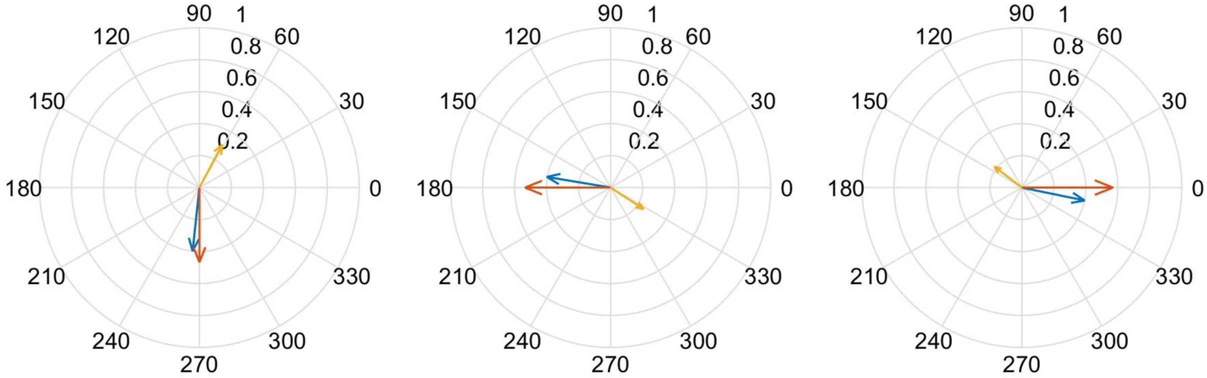

(b) S1-G1 (c) S1-G2 (d) S1-G3

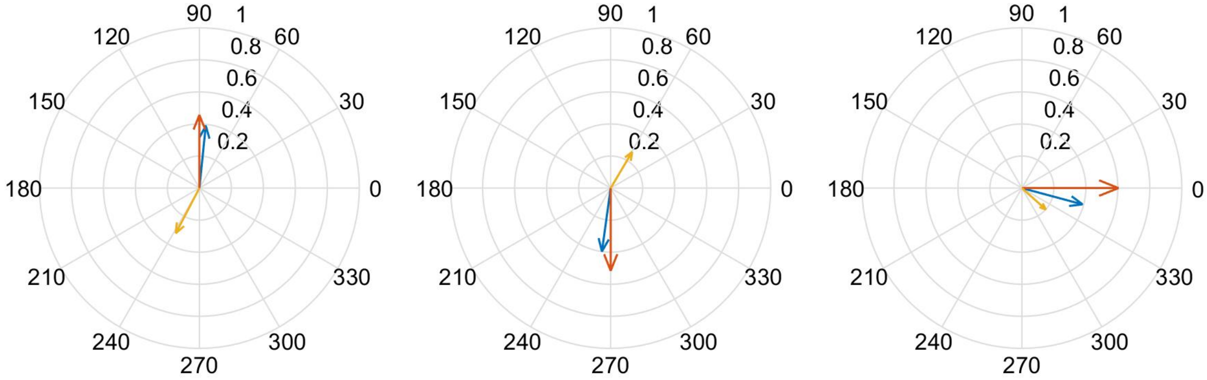

(e) S2-G1 (f) S2-G2 (g) S2-G3

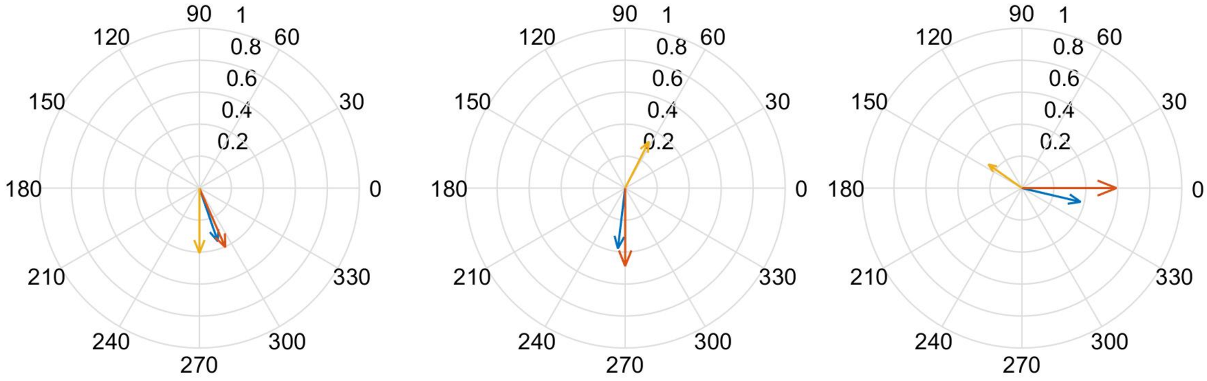

(h) S3-G1 (i) S3-G2 (j) S3-G3

Figure K.1: Argand diagrams of flutter mode complexity

NTNU
Norwegian University of
Science and Technology